Thermomechanical behavior of different Ni-base superalloys for turbine blade forging dies

Master Thesis of

Matthias Hacksteiner, BSc

Institute of Material Science and Welding

Supervisor: Ass.Prof. Dr.techn. Maria Cecilia Poletti

Chair: Univ.-Prof. Dipl.-Ing. Dr.techn. Christof Sommitsch

In collaboration with Böhler Schmiedetechnik GmbH & Co KG

Advisor: Dipl.-Ing. Daniel Huber

Faculty of Mechanical Engineering and Economic Sciences

Graz University of Technology, Austria

Graz, May 2013

Eidesstattliche Erklärung

Ich erkläre an Eides statt, dass ich die vorliegende Arbeit selbstständig verfasst, andere als die angegebenen Quellen/Hilfsmittel nicht benutzt, und die den benutzten Quellen wörtlich und inhaltlich entnommenen Stellen als solche kenntlich gemacht habe.

Graz, Mai 2013 Matthias Hacksteiner

Statutory declaration

I declare that I have authored this thesis independently, that I have not used other than the declared sources/resources, and that I have explicitly marked all material which has been quoted either literally or by content from the used sources.

Graz, May 2013 Matthias Hacksteiner

Kurzfassung

Der Wirkungsgrad von Flugzeugen lässt sich durch die Verwendung fortschrittlicher Werkstoffe erhöhen, die entweder eine generell leichtere Konstruktion oder höhere Verbrennungstemperaturen in der Gastubine ermöglichen. Der Einsatz von Gamma-Titanaluminiden, hochfesten intermetallischen Legierungen, ermöglicht beides. Dieser Materialtyp ist ein vielversprechender Nachfolger von weit etablierten Nickelbasis-Superlegierungen für diverse Triebwerkskomponenten, da er ähnliche Hochtemperaturfestigkeiten bei nur etwa halber Dichte aufweist.

Ein laufendes Forschungsprojekt widmet sich der Herstellung von Niederducktubinenschaufeln aus einer Titanaluminid-Legierung durch Gesenkschmieden. Der Schmiedeprozess erfordert hohe Kräfte und Temperaturen, was zu einer hohen Belastung der Schmiedegesenke führt. Aus diesem Grund muss deren Werkstoff hervorragende Hochtemperatureigenschaften aufweisen, um einen stabilen Produktionsprozess und lange Lebensdauer zu gewährleisten.

Die vorliegende Arbeit liefert eine detaillierte Untersuchung des thermomechanischen Verhaltens dreier Legierungen, die als Gesenkwerkstoff in Betracht gezogen werden. Es handelt sich um gut verarbeitbare Nickelbasislegierungen, die aufgrund ihrer charakteristischen teilchengehärteten Mikrostruktur ausgezeichnete mechanischen Eigenschaften im betrachteten Temperaturbereich aufweisen. Die weit verbreitete sowie gut untersuchte Legierung Inconel 718 dient als Referenzwerkstoff und wird mit zwei neu entwickelten Superlegierungen, Allvac 718Plus und Haynes 282, verglichen. Basierend auf den Ergebnissen physikalischer Simulationen des Schmiedeprozesses wird eine Werkstoffwahl getroffen.

In thermomechanischen Versuchen an Zugproben wurden Temperatur- und Lastzyklen dem realen Schmiedeprozess nachempfunden. Mit mikrostrukturellen Untersuchungen und numerischen Ausscheidungssimulationen wurde versucht, die erhaltenen Ergebnisse zu interpretieren und ein generelles Verständnis über das Materialverhalten unter den gegebenen Bedingungen zu erlangen.

Die thermomechanischen Versuche wurden bei unterschiedlichen maximalen Spannungen und bis zu unterschiedlichen plastischen Dehnungen durchgeführt. Alle drei Legierungen wiesen eine Spannungsabhängigkeit der minimalen Dehnraten enstprechend Potenzgesetzen auf. Die Auswertung der Spannungsexponenten im industriell für Schmiedegesenke relevanten Bereich niedriger plastischer Dehnungen lässt vermuten, dass es sich beim vorherrschenden Verformungsmechanismus um Versetzungskriechen handelt.

Verglichen mit dem Ausgangsgefüge wiesen plastisch verformte Proben verschiedene mikrostrukturelle Veränderungen auf. Es konnten eine starke Verformung der Kornstruktur und Entfestigungsmechanismen wie Teilchenvergröberung, Teilchenumwandlung sowie dynamische Rekristallisation beobachtet werden.

Abschließend wurde eine Reihung der Werkstoffe im Hinblick auf Wirtschaftlichkeit und Standzeit durchgeführt.

Abstract

Aircraft efficiency can be increased by the utilization of advanced materials which enable either lighter structural construction or higher jet engine combustion temperatures. Both approaches can be realized by the use of gamma titanium aluminides, high-strength intermetallics. The material is a promising successor of widely established Ni-base alloys for certain aircraft engine components as it exhibits similar mechanical properties at only around half the density.

A current research project focuses on the processing of this intermetallic compound to low-pressure turbine blades via die forging. This forming process requires high stresses and temperatures. Therefore, the forging tool material has to meet great demands regarding its high-temperature properties in order to guarantee a stable production process and long service life.

In this study, a detailed investigation of the thermomechanical behavior of three pre-selected candidates for the forging die material is presented. All three investigated materials are readily processable Ni-base superalloys which exhibit excellent mechanical properties due to their characteristic precipitation strengthened microstructures. Inconel 718, a widely applied and thoroughly investigated alloy, is used as reference material and compared to two rather new superalloys, Allvac 718Plus and Haynes 282.

Final material selection is performed based on the results of physical forging simulations. Thermomechanical tests were carried out using tensile samples with temperature and load cycles based on the real forging process. Microstructural investigations and numerical simulations were performed to interpret the obtained results and to get a general insight into the material behavior under given conditions.

Thermomechanical tests were carried out at three different maximum stress levels and up to varying plastic strains. For all investigated alloys, the stress dependence of their minimum strain rates followed power-law relationships. An evaluation of the corresponding stress exponents suggests that the predominating deformation mechanism up to very low plastic strains (as industrially relevant for forging dies) is dislocation creep.

Different microstructural changes were observed in deformed specimens compared to the initial state. These changes include strong deformation of the grain structure and softening mechanisms such as precipitate coarsening or transformation as well as dynamic recrystallization.

To conclude the work, a benchmark regarding service life and cost effectiveness is presented.

Acknowledgements

First of all, I owe a great debt of gratitude to the director of the Institute for Materials Science and Welding (IWS) at Graz University of Technology, *Univ.-Prof. Dipl.-Ing. Dr.techn. Christof Sommitsch*, for the opportunity to accomplish my Master Thesis at his institute. Furthermore, I am deeply grateful to the former head of the institute, *Em.Univ.-Prof. Dipl.-Ing. Dr.mont. Horst H. Cerjak*, for arousing my curiosity in materials science and for taking me aboard as a member of IWS. I want to thank both of them and the whole IWS team for the great cooperation during my work as student assistant over the last years.

Special thanks are directed to my highly motivating and supportive supervisor at IWS, *Ass.Prof. Dr.techn. Maria Cecilia Poletti*. She proposed solutions to any problem I encountered during the work and expanded my knowledge in numerous enriching discussions. Her passion in materials science as well as her warm and friendly nature made our cooperation a pleasure both on a professional and personal level.

In the same breath I want to thank my advisor at Böhler Schmiedetechnik GmbH & Co KG, *Dipl.-Ing. Daniel Huber*, who entrusted me with this great and challenging task and provided competent and kind support whenever necessary.

In addition, I would like to thank the IWS laboratory staff for their assistance and advice concerning laboratory and workshop activities. Special thanks are also directed to *Dr.techn. Fernando Warchomicka* of the Institute of Materials Science and Technology at Vienna University of Technology for his patient help with FEG-SEM investigations. Furthermore, I am grateful to both *Dr. sc. ETH Erwin Povoden-Karadeniz* and *Dipl.-Ing. Stojan Vujic* for their kind support concerning numerical simulations with MatCalc.

The greatest thanks, however, are directed to my family and especially my parents who have always been a constant source of love, support and strength during my years of study and my whole life. Thank you for everything!

Table of contents

1 Introduction

Since the beginning of motorized aviation in the early 20th century, the world has changed significantly. Fast and inexpensive long-distance travelling and shipping laid the cornerstone of globalization.

In the last decades, the severe economic and ecological impact of the aircraft industry led to a great amount of research to improve aircraft efficiency. Fuel consumption and therefore operating costs and negative environmental effects (keyword global warming) need to be reduced. One important way of improving aircraft efficiency is to develop new, advanced materials which enable either lighter construction or higher jet engine combustion temperatures.

The manufacture and processing of such materials is a major challenge. Thus, comprehensive experience and research are needed in order to process these materials into high quality, ready-to-mount components. A typical example of such high-duty products are turbine blades. Exposed to severe mechanical, thermal and chemical load, these components need to fulfill highest reliability and durability requirements.

Several critical processing steps and considerable efforts in quality management and inspection are needed to produce such products. This work deals with one manufacturing step of turbine blades: shaping via die forging. High stresses and temperatures are required to form the blade material which is a novel, high-strength light-weight alloy. Therefore, the forging tool has to meet great demands regarding mechanical and thermal material properties in order to achieve long service life and guarantee a stable production process.

Based on a physical simulation of the forging process, forging die material selection and characterization is performed in the present work. Three materials, all of which are Ni-base superalloys, are being investigated and compared.

2 Initial situation and objectives

The project partner, Böhler Schmiedetechnik GmbH & Co KG (BSTG), manufactures forgings for different applications, for instance aerospace engine parts, turbine blades and a variety of structural components.[1]

A current work project of BSTG, called *DAFNE* (Development of γ-TiAl forgings in a near conventional hot-die low-cost process and evaluation of prototype production), is part of the European *Clean Sky* initiative which promotes the development of different technologies to increase the environmental performance of aircraft.[2]

Aims of DAFNE project are as follows:

- The development of a small-scale series production for titanium aluminide (TiAl) turbine blades for geared turbofan engines, concretely for the last stage of the low-pressure turbine of *PW1524G* test engine (see **Figure 1**) which will be applied in the currently developed *Bombardier CSeries* airliner. The replacement of previously used Ni-base alloys as blade material by γ-TiAl will result in significant weight reduction.
- The stabilization of the turbine blade manufacturing processes. The process steps are as follows: pre-forming (upsetting) of the blank, coating with a ceramic thermal barrier, pre-heating, hot-die forging, jet-cutting of the forging flash, heat treatment and adjustment.
- The optimization of the manufacturing processes.
- The development of an execution plan for the large-scale series production in which up to 24800 turbine blades are manufactured annually until 2023.

Forging is performed on a *Schloemann* hydraulic press (see **Figure 2**) with an adapted control system which enables low deformation speeds and an accurate control of die position, speed and temperature. Due to the use of a conventional hydraulic press the investigated industrial process is called "near-conventional".[3]

In order to produce sound forgings in an economical manufacturing process, following requirements arise for the forging die material:

- temperature resistance and microstructure stability up to temperatures above 800°C
- good mechanical properties at operating temperatures
    - strength and creep strength
    - toughness
    - fatigue strength
- electrical conductivity (for inductive heating)
- high thermal conductivity
- low thermal expansion
- oxidation resistance at operating temperatures
- good processability (to keep die manufacturing costs low)
- good weldability (for repair work)
- affordable material costs

Based on these requirements, a previous materials selection using the software Cambridge Engineering Selector (CES) suggested the use of Ni-base superalloys.[4]

In the present work, based on a physical simulation of the forging process, three such superalloys are investigated regarding their thermomechanical behavior: Inconel 718, a widely applied and thoroughly investigated alloy, is used as reference material and compared to two rather new superalloys, Allvac 718Plus and Haynes 282.

A comparison of the material performance in the physical forging simulations combined with microstructural characterization and interpretation should lead to a recommendation concerning the forging die material selection.

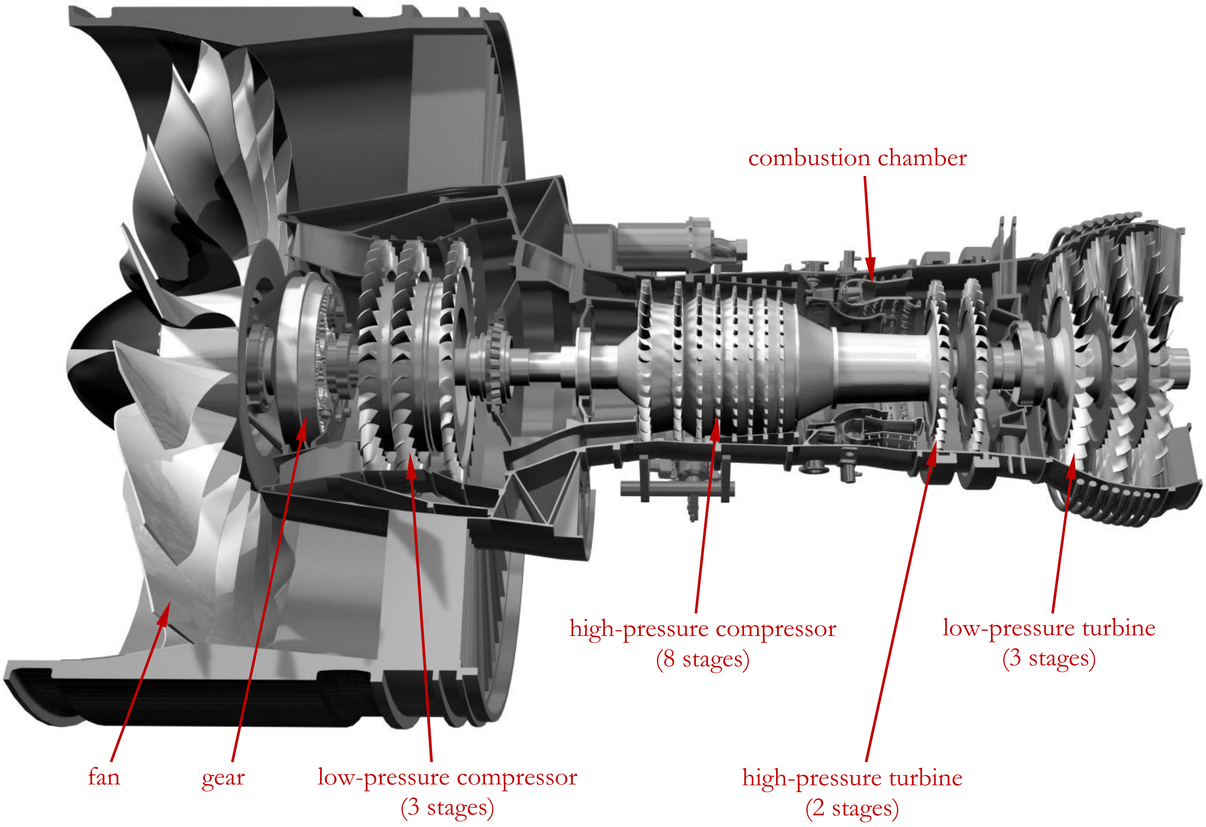

Figure 1. PW1524G test engine

Figure 2. Schloemann hydraulic press

3 Literature Review

3.1 Die forging

According to DIN 8583-4, die forging is defined as a technique in which metal is formed mainly using (uni- or multiaxial) compressive stresses via tools which are moved against each other, enclosing the work piece and containing its shape.[5]

Die forging belongs to the manufacturing technique *bulk forming* as the work piece dimensions are of the same magnitude in all directions (in contrast to sheet metals, for instance). Furthermore, it is a *hot forming* process as it typically takes place at temperatures higher than the metal's recrystallization temperature which enhances the formability and therefore decreases forging forces and stresses.[6, 7]

The process is characterized by tool-dependent shaping of the work pieces (called *forgings*) via impressions of the upper and lower tools (called *forging dies*). Die forging is commonly used for large-batch production of different kinds of products, reaching from semi-finished parts that require further processing to ready-to-mount finished parts. Typical die forged components are crankshafts, front axles, roller bearing rings, gear wheels, wheel hubs and turbine blades.[8]

3.1.1 Die forging process

Starting from the forging blank (which is commonly rolled rod, strip or billet stock), forgings typically run through one or more intermediate forming processes depending on the complexity of the desired geometry. These processes can involve bending or pre-profiling (typically via free forming or die forming processes with partly enclosed work piece) to approach the final contour. This has the following advantages for the final forming process:[8]

- prevention of excessive local flash formation
- improved metal flow in die impressions resulting in reduced forging forces
- reduction of die wear
- improved grain orientation and end form quality of the work piece
- prevention of metal flow in longitudinal direction for elongated work pieces

Figure 3 shows two basic die forging methods of which the process with flash has higher industrial significance. The basic types of die filling processes are material flows parallel to (upsetting), perpendicular to (spreading) or against the tool movement (rising) as illustrated in **Figure 4**.

After filling the impression, excess material is forced through the flash gap. The flash geometry affects the stresses inside the forging and the material flow behavior and should therefore be carefully designed in order to produce sound forgings. After forging, the flash is removed either in hot (≈ forging temperature) or cold (room temperature) condition depending on the material's strength and the work piece geometry.[9, 10]

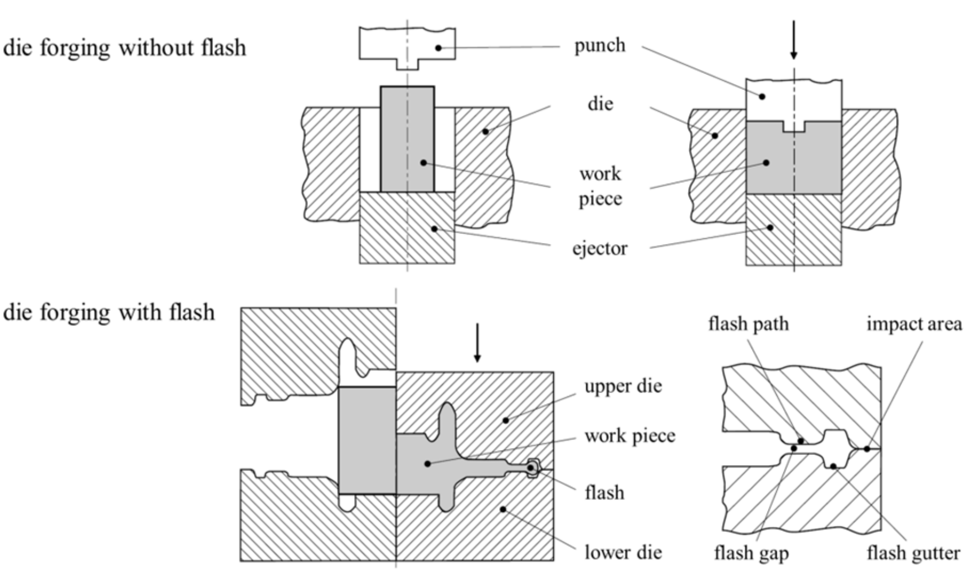

Figure 3. Basic die forging methods (adapted from [8])

Die forging without flash, on the contrary, does not require this flash trimming operation. Furthermore, it reduces the necessary forging force and saves up to 40% material. However, it requires high accuracy of the forging blank's volume, contour and positioning. [11]

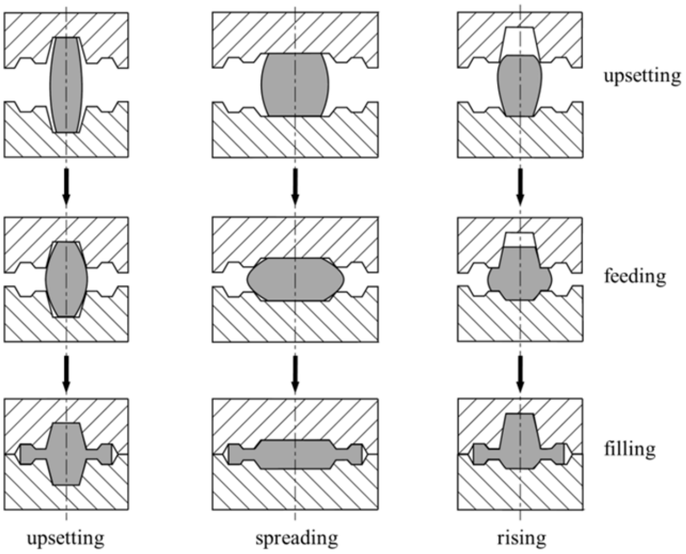

Figure 4. Basic filling processes of forging dies (adapted from [10])

In comparison to cast components, forgings typically obtain better mechanical properties. Pores can form in cast components during the transition from liquid to solid state of the metal due to shrinkage. If located at critical positions, these pores can have fatal influence on the component's lifetime. However, they can be closed when the cast material is rolled, pre-formed and/or forged (i.e. when it is worked). Furthermore, this processing leads to a beneficial grain orientation during forging. For these reasons, forgings obtain higher strength and ductility and thus lower weight which makes them a favorable choice for components working under high static and dynamic loading conditions. [6]

3.1.2 Damage mechanisms of forging dies

Forging dies are subjected to a combination of thermal, mechanical, tribological and chemical exposure. A continuous thermal load results from the elevated die base temperature T_{die} and near-surface cyclic thermal stresses arise from changing surface temperatures during each forging cycle (see **Figure 5**).

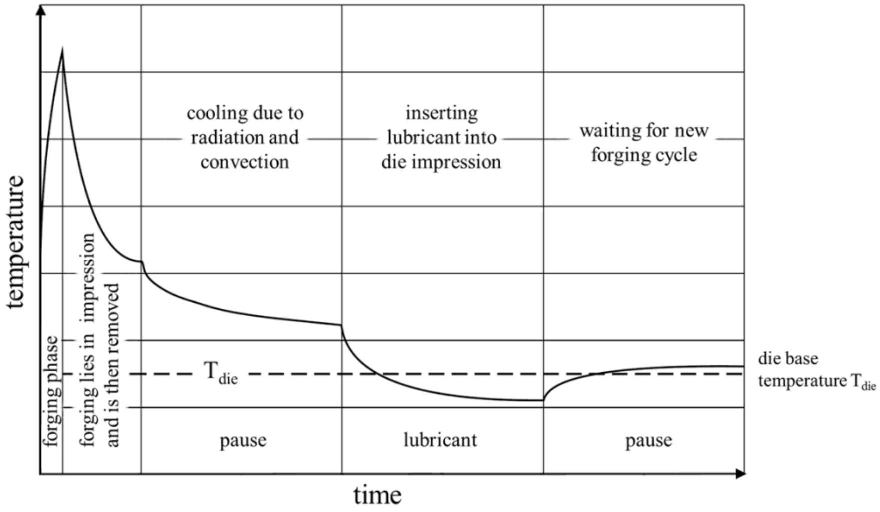

Figure 5. Temperature sequence of the die surface during a forging cycle (adapted from [12])

The peak temperature during the forging phase depends on material, mass and temperature of dies and work piece. Furthermore, it is influenced by normal stress, forging time, an optional thermal barrier as well as the relative movement between tools and work piece resulting from material flow. The peak temperature (and therefore the temperature gradient) determines the maximal thermal compressive stresses resulting from strain constraint. If these compressive stresses locally exceed the die material's yield strength, residual tensile stresses form after a following temperature drop. Due to lubrication of the die impression between forging cycles, its surface temperature can decrease to values lower than the die base temperature. This results in the formation of additional thermal tensile stresses due to strain constraint. Cyclic plastic deformation arising from these alternating stresses can ultimately lead to crack formation and component failure. [10, 12]

Due to the relative movement between tool and work piece, different friction conditions arise in their contact area. The tribological system is influenced by the material flow, the temperature as well as lubricant and reaction products, particularly scales. Therefore, depending also on the surface finish of the friction partners, all conditions from solid state to hydrodynamic fluid friction can appear. Consequently, severe tool wear can occur, especially at positions with high relative velocity and contact pressure. [12]

Figure 6 summarizes common damage mechanisms of forging dies. Crack initiation due to mechanical fatigue typically appears at positions with high stress concentration. However, the real state of stress in the die results from a superposition of mechanical and thermal stresses. Therefore, in order to be able to prevent tool damage, these stresses should be determined as precisely as possible which is typically achieved via numerical forming simulations using the finite element method (FEM). [8]

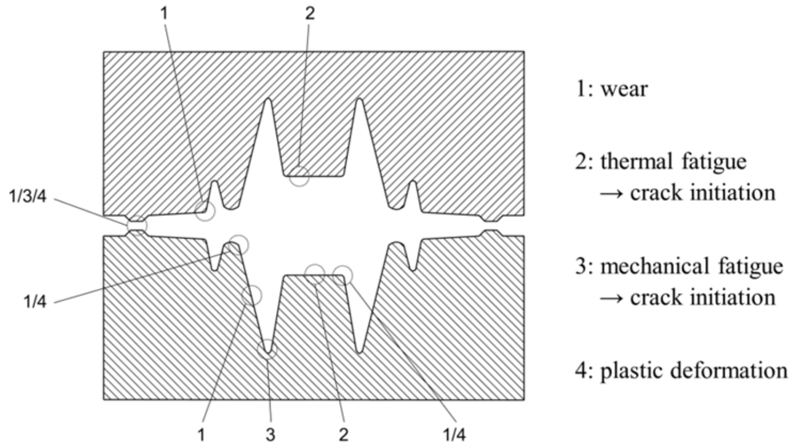

Figure 6. Damage mechanisms of forging dies (adapted from [10])

3.2 Ni-base alloys

3.2.1 Application and properties of Ni-base alloys

Ni-base superalloys belong to high temperature materials which can be used above 550 °C under considerable mechanical load and chemical exposure for long times. They typically contain up to 15 alloying elements and obtain strengthening particle volume fractions of up to around 70% which enables long-term operation at up to 85% of their melting temperature. The main driving force for the development of Ni-base alloys is the gas turbine industry as the efficiency of turbines for power plants and aircraft is raised by increasing the combustion temperatures. However, such superalloys are also widely used for different applications in mechanical and process engineering because their properties generally include: [13, 14]

- good mechanical properties at operating temperatures
  - strength and creep strength
  - ductility and fracture toughness
  - fatigue strength
- corrosion and oxidation resistance at operating temperatures
- thermal microstructure stability
- economical manufacture and processing

3.2.2 Microstructure of Ni-base alloys

Ni-base superalloys feature a face centered cubic (fcc) Ni-Cr (γ) matrix which accounts for several beneficial material properties: [13, 15]

- Ni exhibits no allotropic transformation which may lead to structural destabilization or a change in properties.
- The γ matrix has a high solubility for alloying elements which enables both solid solution strengthening and precipitation hardening.

- A strongly bonding oxide surface layer prevents intrusion of H and S into the material as well as loss of alloying elements.
- The crystal lattice exhibits multiple slip systems which promotes the alloy's ductility and formability.
- Precipitation of ductile strengthening phases is facilitated in contrast to brittle phases.

Figure 7 shows an overview of typical alloying elements for Ni-base alloys with their basic effects and a rough indication concerning their quantity. A more detailed description of these effects is given in **Table 1** for selected alloying elements relevant to the present work.

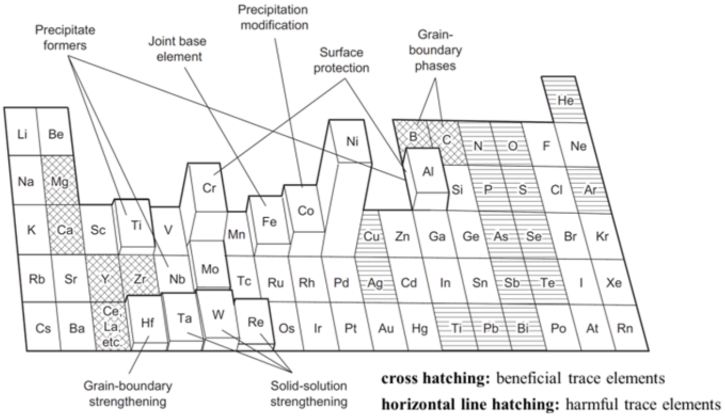

Figure 7. Typical alloying elements of Ni-base alloys and their principal effects [16]

The main microstructural parameters influenced by alloying elements are: [13, 14]

- lattice parameter (i.e. the distance between unit cells in the crystal lattice) of the γ matrix and intermetallic precipitate phases (see **Figure 8**)
- stacking fault energy (affecting dislocation cross-slip and climb movements)
- diffusion coefficients in the matrix and at grain boundaries (affecting microstructure stability)
- modulus of elasticity
- solidus temperature
- oxidation resistance
- type, amount and morphology of precipitate phases

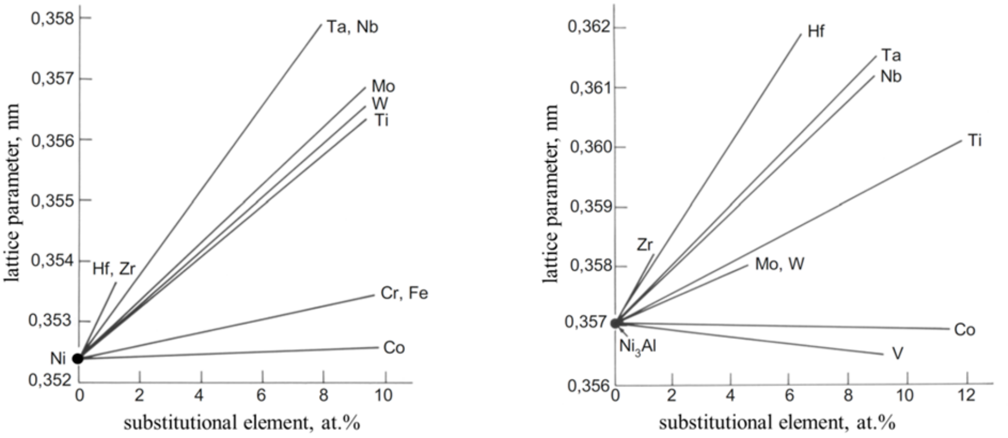

Figure 8. Influence of substitutional elements on the lattice parameters of the Ni solid solution (γ, left) and Ni_3Al phase (γ', right) (adapted from [13])

Table 1. Typical alloying elements of Ni-base alloys and their effects on microstructure and material properties (continued on the next page) [13, 14, 17-21]

element	effects
Al	• strong solid solution strengthening of the γ matrix • forms the γ' phase (Ni_3Al) • forms an Al_2O_3 surface layer to prevent high temperature oxidation (long-term protection for temperatures higher than 950 °C) • with increasing content of Al the phase stability is reduced (more Ni is bound in γ' phase which decreases the content of Ni in the γ matrix)
Ti	• strong solid solution strengthening • substitutes Al in γ' and Nb in γ'' and therefore increases the volume fractions of γ'/γ'' • forms TiC carbides and Ti(C,N) carbonitrides • forms the embrittling η phase (Ni_3Ti) in case of high alloy content • increases the γ/γ' lattice misfit parameter and therefore the γ' coarsening rate • can decrease oxidation resistance
Nb	• strong solid solution strengthening • substitutes Al in γ' therefore increases the volume fraction of γ' • increases the γ/γ' lattice misfit parameter but delays γ' coarsening because of its low diffusion coefficient • forms the metastable γ'' phase (Ni_3Nb) • forms NbC carbides • forms δ phase (Ni_3Nb) preferably at grain boundaries in case of high alloy content • decreases oxidation resistance
Cr	• moderate solid solution strengthening (high solubility in γ matrix) • increases the creep strength by reducing the stacking-fault energy • provides corrosion resistance due to the formation of a Cr_2O_3 surface layer • supports the formation of protective Al_2O_3 surface layer • forms carbides (mainly $M_{23}C_6$ and M_7C_3) • facilitates the formation of TCP phases (σ, Laves)
Fe	• low cost substitute for Ni • facilitates the formation of TCP phases • decreases oxidation resistance in case of high alloy content
Co	• slight solid solution strengthening • increases creep strength by reducing the stacking-fault energy • reduces the solubility of Al and Ti and therefore increases γ' volume fraction • delays γ' coarsening but reduces γ' solvus temperature • can decrease high temperature corrosion resistance in case of high alloy content • counteracts the formation of TCP phases • raises the solidus temperature
Mo	• strong solid solution strengthening • increases creep strength by reducing the stacking-fault energy • increases modulus of elasticity • decreases the diffusion coefficients of other elements in the matrix • increases the γ' solvus temperature • forms carbides (especially M_6C) • facilitates the formation of TCP phases • decreases oxidation and hot gas corrosion resistance
W	• similar effects as Mo • segregates strongly • strongly increases the alloy's density (heavy element)
Ta	• strong solid solution strengthening • substitutes Al in γ' and Nb in γ'' and therefore increases the volume fractions of γ'/γ'' • delays γ' coarsening • reduces the Al_2O_3 surface layer growth rate • forms TaC carbides • facilitates the formation of TCP phases • increases oxidation and hot gas corrosion resistance • strongly increases the alloy's density (heavy element)

element	effects
Mn	• tends to segregate at grain boundaries which has embrittling effect (decreases hot workability and creep ductility) but improves weldability • compounds with S to globular MnS at grain boundaries
B	• effective at grain boundaries (smaller than Ni) • decreases the grain boundary diffusion coefficient and therefore improves creep strength • prevents the formation of carbide films on grain boundaries and carbide coarsening • forms borides (as a replacement of carbides) • affects the susceptibility to hot cracking for higher alloy content • suppresses the formation of Laves phase • strongly decreases the alloy's solidus temperature
C, N	• form carbides and carbonitrides • strongly decrease the alloy's solidus temperature
S	• decreases ductility without influencing strength • does not influence grain structure as well as morphology and quantity of precipitates
P	• increases rupture life and ductility • does not influence grain structure as well as morphology and quantity of precipitates

Figure 9 shows the crystal structure of certain phases typically observed in Ni-base alloys. The intermetallic, face centered cubic γ' phase of nominal stoichiometry Ni_3Al (see **Figure 9**, left) is the predominant strengthening phase in most Ni-base alloys. Typically, γ' precipitates rather quickly and homogeneously in the γ matrix in the form of coherent, nanometer-sized particles acting as effective obstacles for dislocations. The lattice parameter of the phase and therefore its volumetric misfit to the matrix is mainly influenced by alloying elements (see **Figure 8**, right). The lattice misfit is typically very small, which benefits microstructure stability, and determines the shape of the precipitates. With rising misfit, γ' morphology typically changes from spherical (< 0.2%) to cubic and finally to plate-like (> 1.25%). The volume fraction of γ' phase is primarily determined by the (Al+Ti) content of the alloy and its stability by the Al/Ti ratio. The strength of Ni_3Al exhibits a positive temperature dependence resulting in a maximum at around 800 °C. Generally, workability and weldability of an alloy strongly decrease with increasing γ' level while its tensile and creep properties increase. [14, 22, 23]

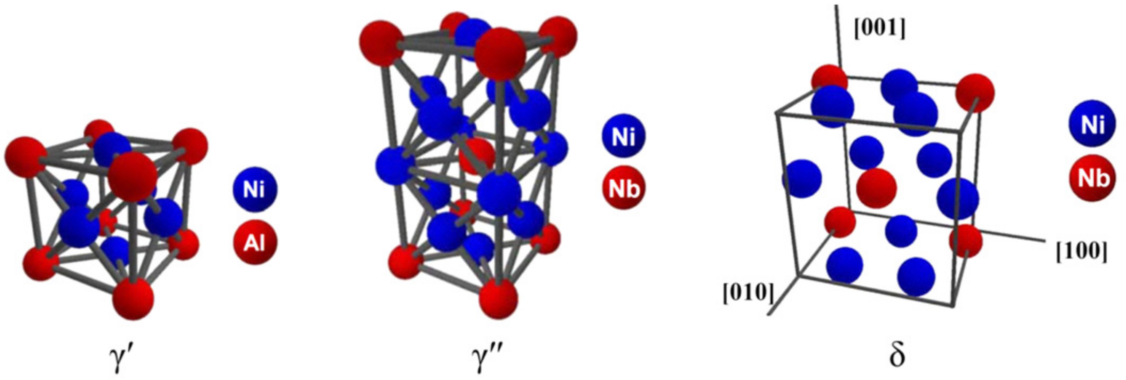

Figure 9. Crystal structure of different precipitate phases in Ni-base alloys [24]

The body centered tetragonal γ'' phase of nominal stoichiometry Ni_3Nb (see **Figure 9**, center) occurs in superalloys with high Nb content. In contrast to γ', the phase is only partially coherent to the γ matrix resulting in plate-like precipitate morphology and high coherence stresses causing an excellent strengthening effect. For the same reason, however, γ'' phase is unstable at elevated temperatures and tends to coarsen and transform to the stable orthorhombic δ phase of the same nominal stoichiometry (see **Figure 9**, right). Latter is an incoherent phase typically occurring at grain boundaries as plate-shaped precipitates. Depending on their size and amount, these δ platelets exert a certain pinning force on grain boundaries and are therefore suitable to control grain growth during hot heat treatment and deformation or to prevent intergranular cracking. For higher volume fractions and larger particle size, however, δ phase has an embrittling effect on the microstructure. [13, 22, 25]

Other important precipitate phases present in Ni-base alloys are carbides mainly of MC, $M_{23}C_6$ and M_6C type. MC are stable primary carbides forming during solidification for which reason they may contain N and are therefore often denoted as M(C,N) or simply MX. Typically, these particles are rather large (> 1μm) and do not have relevant influence on the alloy's mechanical properties. A small amount of MX phase can dissolve during solution annealing and, during subsequent tempering, precipitate as fine particles, preferentially at dislocations, which results in effective strengthening. However, these particles tend to coarsen and transform to $M_{23}C_6$ during long-term thermal exposure. Latter can be considered the most important carbide type in Ni-base alloys. After dissolving during solution annealing, $M_{23}C_6$ precipitates mainly at grain boundaries. This can prevent grain boundary sliding, especially in the case of small, spherically shaped and uniformly distributed particles. However, for certain morphologies and large particle sizes, $M_{23}C_6$ can also have an embrittling effect. [13, 14]

Further precipitates observable in Ni-base alloys are topologically close packed (TCP) phases like μ, Laves or σ. In contrast to geologically close packed phases with their isotropically tightest packing, TCP phases obtain planes with layers of bigger atoms. Therefore, these phases have fewer slip systems which makes them hard and brittle. The formation of TCP phases results in a depletion of solid solution strengthening elements in the matrix. They exhibit complex crystal structures with large elementary cells and are incoherent to the γ matrix. For these reasons, the occurrence of TCP phases decreases the alloy's toughness, fatigue strength and rupture time. [13, 22]

Table 2 summarizes the properties and effects of the most important precipitate phases in Ni-base alloys.

Table 2. Typical precipitate phases in Ni-base alloys and their effects on microstructure and material properties (continued on the next page) [13, 14, 22, 23]

phase	crystal structure	elements/formula	notes
γ'	fcc	$Ni_3(Al,Ti)$	• main strengthening phase in many Ni-base alloys • coherent phase (slight lattice misfit to the γ matrix) • typically obtains high volume fractions • mostly spherically or cubically shaped
γ''	bct	$Ni_3(Nb,Al,Ti,Ta)$	• only occurs at high content of Nb • plate-shaped, partly coherent phase • metastable
δ (or β)	ortho-rhombic	$Ni_3(Nb,Al,Ti,Ta)$	• only occurs at high content of Nb • occurs mostly as coarse plates at grain boundaries • has embrittling effect but can delay grain coarsening
η	hcp	Ni_3Ti	• forms at high Ti/Al ratios after long thermal exposure • cellularly shaped at grain boundaries or as plates with Widmannstätten pattern inside grains • typically forms coarse structures
MX	fcc	M = Ti, Nb (Ta, W, Mo) X = C, N	• irregularly shaped • variable composition • very stable (dissolves above the solidus temperature)

phase	**crystal structure**	**elements/formula**	**notes**
$M_{23}C_6$	cubic	M = Cr, Fe, Mo, W, Ni, Co (Ti, Nb)	• grain boundary precipitates in different shapes (films, globules, plates or cells) • most common type: $Cr_{23}C_6$
M_6C	cubic	M = Fe, Mo, W, Nb, Ta, Ni, Co	• randomly distributed at grain boundaries • occurs at high content of Mo and W • replaces $M_{23}C_6$ at high temperatures
M_7C_3	hexagonal	Cr_7C_3	• block-shaped grain boundary precipitates • less common, typically forms after exposure above 1000 °C • relatively unstable (tends to transform to $M_{23}C_6$)
M_3B_2	tetragonal	M = Mo, Ta, Nb, Ni, Fe	• only occurs at high content of B (> 0.01%) • shaped similarly to carbides
μ	rhombo-hedral	$(Co,Fe)_7(Mo,W)_6$	• TCP phase (decreases creep strength and ductility) • occurs at high content of Mo and W • shaped as coarse, irregular Widmannstätten pattern
Laves	hexagonal	A_2B A = Fe, Co, Cr, Mn, Si B = Mo, W, Nb, Ti, Ta	• TCP phase (decreases creep strength and ductility) • less common (only occurs at high content of Fe and in the presence of Si) • irregularly shaped (elongated globules, platelets)
σ	tetragonal	$(Fe,Ni,Co)_x(Cr,Mo,W)_y$ with $x \approx y \approx 1..7$	• TCP phase (decreases creep strength and ductility) • derived from the intermetallic phase FeCr • less common • irregularly shaped (elongated globules, needles, plates, Widmannstätten pattern) • forms after extended exposure at high temperatures

3.2.3 Investigated materials

3.2.3.1 Inconel 718

Inconel 718 (commonly abbreviated as IN718 or just alloy 718) is a wrought, Fe-rich precipitation-hardenable superalloy used since 1965. Nowadays the alloy accounts for nearly half of the total quantity of globally used Ni-base alloys because of its very high strength, corrosion resistance and creep resistance up to 650 °C. Furthermore, Inconel 718 shows good hot and cold workability, excellent weldability and is moderately priced due to its high Fe and low Co contents. **Table 3** shows the nominal chemical composition of the alloy which is used for a wide range of applications such as components for gas turbines, rocket engines, cryogenics, space and process technology as well as in chemical, oil and gas industry. The alloy was not primarily designed for creep resistance but for high strength up to temperatures of 650 °C. [14, 26, 27]

Table 3. Nominal chemical composition of Inconel 718, wt.% [32]

Ni + Co	Co	Cr	Fe	Nb + Ta	Mo	Ti	Al	C	Mn	Si	Cu	B	P + S
50.00 - 55.00	max. 1.00	17.00 - 21.00	17.90 (bal.)	4.75 - 5.50	2.80 - 3.30	0.65 - 1.15	0.20 - 0.80	max. 0.08	max. 0.35	max. 0.35	max. 0.30	max. 0.006	max. 0.03

In contrary to many γ' hardening superalloys, Inconel 718 exhibits high Nb and rather low Al and Ti contents. This leads to the precipitation of the metastable, partially coherent γ" phase which produces very effective strengthening. For that reason, Inconel 718 typically obtains higher yield strength than most exclusively γ' strengthened superalloys. Depending on the exact chemical composition and heat treatment, the total volume fraction of γ' and γ" strengthening phases is around 15% in precipitation hardened condition and the typical ratio of γ' to γ" is around 1:3. In Inconel 718, γ' preferentially precipitates in areas between γ" particles with a local depletion of Nb (see **Figure 10**).[28, 29]

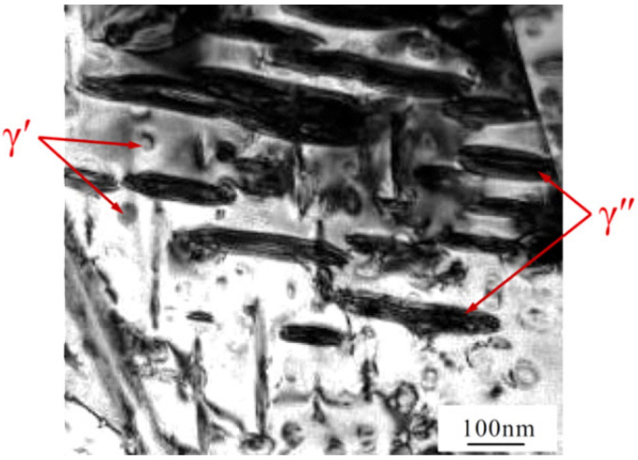

Figure 10. Microstructure of Inconel 718 after 500 hours exposure at 760 °C[27]

Prolonged exposure at temperatures higher than 650 °C leads to overaging of γ" phase which consequently transforms to the stable δ phase. This results in a loss of strength and rupture life. **Figure 11** shows a precipitation-time-temperature (PTT) diagram of γ', γ" and δ phases emphasizing this behavior. The beginning and type of precipitation, however, depends on the material condition after processing, i.e. its residual strain, the concentration of primary δ phase and, most importantly, the amount of Nb segregation. Further commonly observed precipitate phases in Inconel 718 are primary carbides of NbC type and carbonitrides of Ti(C,N) type. After extended thermal exposure, σ phase and α-Cr might also be present in the alloy. Latter is a Cr-rich body centered cubic phase preferentially precipitating at grain boundaries and δ particles and, just like the TCP σ phase, decreasing the alloy's toughness.[27, 29, 30]

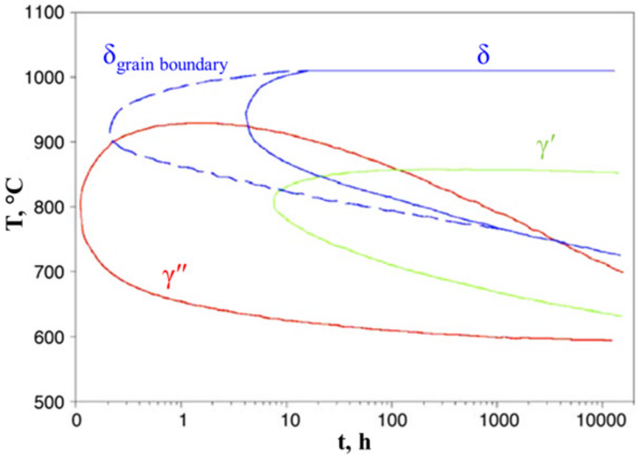

Figure 11. Precipitation-time-temperature diagram for different phases of Inconel 718[31]

Table 4 summarizes the three most important commercial heat treatments of the alloy depending on the desired mechanical properties. Some of the physical and mechanical properties of Inconel 718 are shown in **Table 5**.

Table 4. Commercial heat treatments of Inconel 718 [32, 33]

mechanical properties	solution annealing	precipitation hardening
• highest room temperature yield and tensile strength • best creep properties • highest fatigue strength	1-2 hours at 927-1010 °C followed by air or water cooling to room temperature	8 hours at 718 °C followed by furnace cooling to 621 °C, 8-18 hours aging at 621 °C followed by air cooling
• highest ductility at low temperatures • lower ductility at high temperatures	1-2 hours at 1038-1066 °C followed by air or water cooling to room temperature	10 hours at 760 °C followed by furnace cooling to 649 °C, 20 hours aging at 649 °C followed by air cooling
• slightly lower strength • best corrosion resistance • best microstructure stability at temperatures above 700 °C	1-2 hours at 1010-1038 °C followed by air or water cooling to room temperature	6-8 hours at 788 °C followed by air cooling

Table 5. Physical and mechanical properties of Inconel 718 [32]

ρ	T_{sol}	T_{liq}	λ		α		E		ν	
			20 °C	760 °C	20-100 °C	20-760 °C	20 °C	760 °C	20 °C	760 °C
kg/dm³	°C	°C	W/m·K		10^{-6}/K		GPa		-	
8.19	1260	1336	11.4	23.2	12.8	16.0	208	154	0.294	0.306

Figure 12 shows the temperature dependence of the alloy's tensile properties pointing out its excellent strength up to temperatures of around 760 °C from where a rapid drop in strength and a strong increase in elongation are observable.

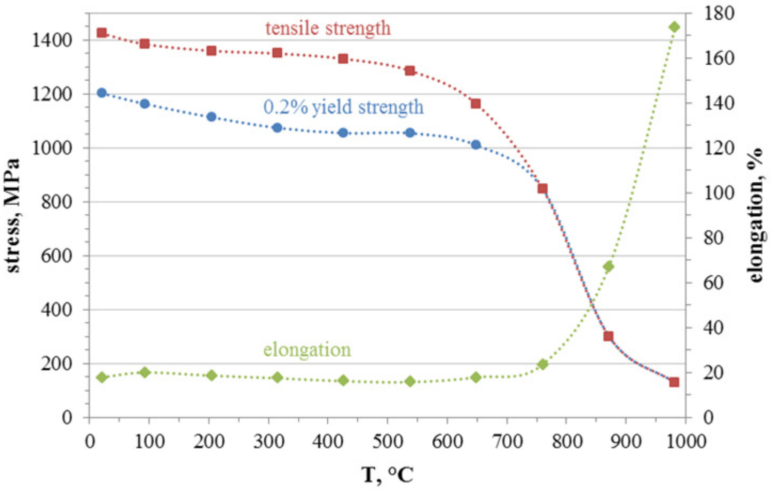

Figure 12. Tensile properties of Inconel 718 (adapted from [32])

3.2.3.2 *Allvac 718Plus*

Allvac 718Plus is a novel Ni-base superalloy developed on the basis of Inconel 718 and maintaining the desirable properties including good weldability, processability and moderate cost. However, mainly due to increased Al content, optimized Al/Ti ratio and the addition of Co and W, rupture life and thermal stability are strongly improved and the alloy's temperature capability was increased by 55 °C. So far, the alloy is used for rotating and non-rotating parts in gas turbines (such as casings, rings, seals, disks and blades) as well as tooling applications (like shear knifes, forging dies or extrusion tools). [26, 34, 35]

As opposed to Inconel 718, the predominant strengthening phase of Allvac 718Plus is γ' phase occurring as spherical nanometer-sized precipitates uniformly distributed in the matrix (see **Figure 13**). The alloy contains high content of Nb and Al and exhibits rather slow precipitation and particle growth rates in contrast to many other γ' strengthened superalloys. Because of its small volumetric misfit, minimal specific surface and high Nb content, γ' phase exhibits high stability during thermal exposure of Allvac 718Plus. Compared to γ" phase in Inconel 718, its coarsening rate is much lower (see **Figure 14**) and its transformation to δ phase happens significantly slower. The second important precipitate phase in Allvac 718Plus, δ phase, occurs in the form of thin, micrometer-sized plates, preferentially at grain boundaries but also at twin boundaries and inside grains. It typically obtains less volume fraction than in Inconel 718 and is more stable with slower coarsening rates at high temperatures. The precipitation of γ'/γ" and δ phases happens faster and at higher temperatures in Allvac 718Plus and their solvus temperatures are higher which benefits the alloy's high temperature properties. Optimal mechanical properties are obtained by carefully controlling the volume fraction, size and distribution of δ phase. Ideally, small plate-shaped δ precipitates are evenly arranged along grain boundaries. However, the precipitation of δ and γ' phases strongly depends on several factors such as the solution annealing conditions and plastic deformation. Depending on the amount of present δ phase, Allvac 718Plus obtains γ' phase fractions of up to 20-23%.[25, 28, 34, 36]

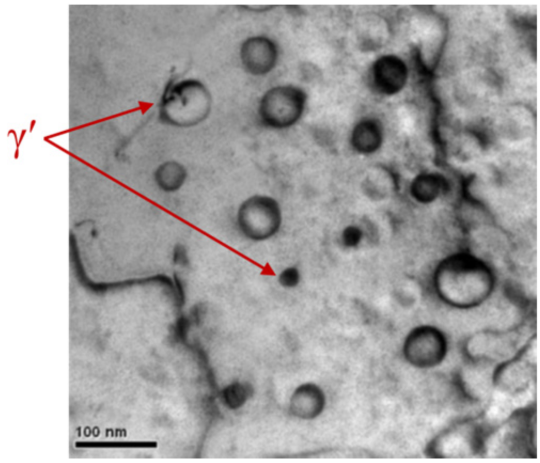

Figure 13. Microstructure of Allvac 718Plus after 2 hours exposure at 875 °C [37]

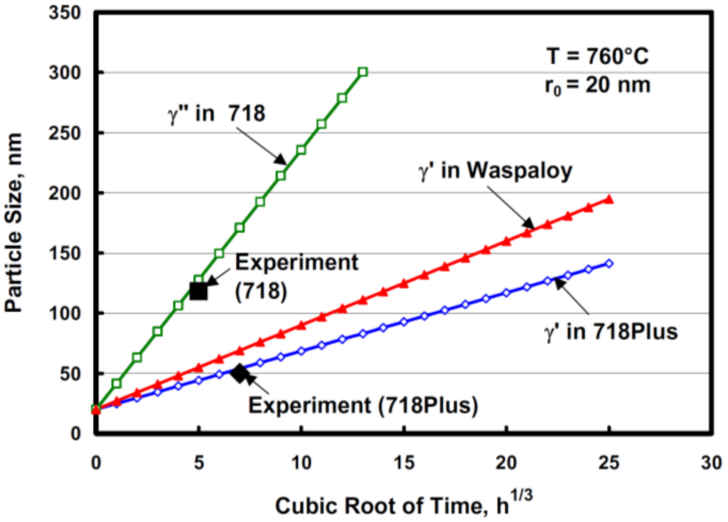

Figure 14. Coarsening rates of strengthening phases in Inconel 718, Allvac 718Plus and Waspaloy [36]

Similar to Inconel 718, primary MX carbonitrides are present in Allvac 718Plus and σ phase might be found after extended thermal exposure. According to recent investigations, no γ'' phase is believed to be present in the alloy. Instead, an additional plate-shaped phase similar to δ phase but with hexagonal close packed structure was found. Its composition is $Ni_3Al_{0.5}Nb_{0.5}$ and it can form as lamellar precipitate at grain boundaries as well as inside grains. [28, 35, 37]

The nominal chemical composition and some physical and mechanical properties of Allvac 718Plus are summarized in **Table 6** and **Table 7**.

Table 6. Nominal chemical composition of Allvac 718Plus, wt.% [38]

Ni	Co	Cr	Fe	Mo	W	Nb	Ti	Al	C	Mn	Si	B	P	S
bal.	8.00 - 10.00	17.00 - 21.00	8.00 - 10.00	2.50 - 3.10	0.008 - 1.400	5.20 - 5.80	0.50 - 1.00	1.20 - 1.70	0.01 - 0.05	max. 0.35	max. 0.035	0.003 - 0.006	0.004 - 0.020	max. 0.025

Table 7. Physical and mechanical properties of Allvac 718Plus [38]

ρ	T_{sol}	T_{liq}	λ		α		E		ν	
			20 °C	760 °C	20-100 °C	20-760 °C	20 °C	760 °C	20 °C	760 °C
kg/dm³	°C	°C	W/m·K		10^{-6}/K		N/mm²		-	
8.25	1260	1343	10.3	23.9	12.3	15.3	214	170	0.308	0.337

The alloy's tensile properties are shown in **Figure 15**. It exhibits slightly higher strength and ductility than Inconel 718 up to a temperature of around 760 °C.

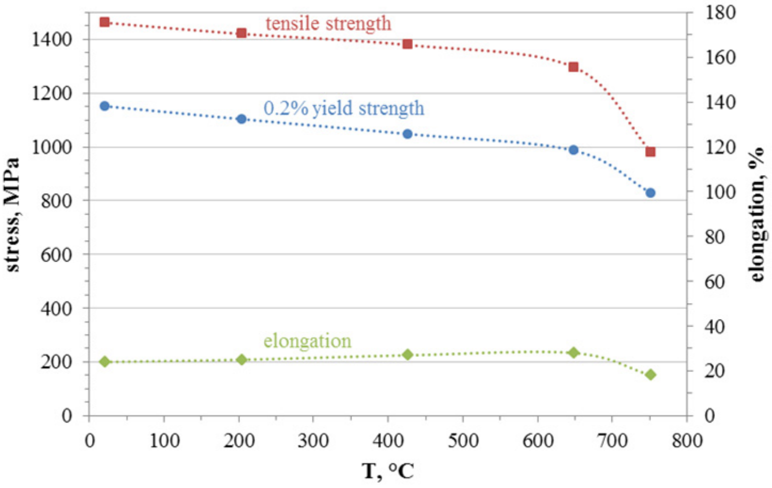

Figure 15. Tensile properties of Allvac 718Plus (adapted from [38])

3.2.3.3 *Haynes 282*

Introduced in 2005, Haynes 282 is a wrought, γ' strengthened superalloy with major amounts of Co, Cr and Mo for solid solution strengthening. It was developed for improved creep resistance at high temperatures (650-930 °C) and obtains very good thermal stability, oxidation resistance and high temperature tensile properties. Furthermore, it exhibits good weldability as well as hot and cold workability. This combination of strength and processability is a result of an optimized γ' level. The alloy is considered for critical components in land-based and aircraft gas turbines, steam turbines as well as in aerospace and automotive applications. [39, 40]

The chemical composition of Haynes 282 and some of its physical and mechanical properties are listed in **Table 8** and **Table 9**. In contrary to Inconel 718 and Allvac 718Plus, it contains no Nb and therefore no γ" and δ phases. In precipitation hardened condition the alloy contains around 20% spherically shaped γ' particles (see **Figure 16**). Further typical phases observed in Haynes 282 are primary MX carbonitrides of the type (Mo,Ti,Cr)(C,N) and $(Mo,Cr)_6C$ carbides. Furthermore, secondary $Cr_{23}C_6$ carbides as well as M_5B_3 borides are typically distributed along grain boundaries.[41, 42]

Table 8. Nominal chemical composition of Haynes 282, wt.%[43]

Ni	**Co**	**Cr**	**Fe**	**Mo**	**Ti**	**Al**	**C**	**Mn**	**Si**	**B**
57.00 (bal.)	10.00	20.00	max. 1.50	8.50	2.10	1.50	0.06	max. 0.30	max. 0.15	0.005

Table 9. Physical and mechanical properties of Haynes 282[43]

ρ	T_{sol}	T_{liq}	λ		α		E		ν	
			20 °C	760 °C	20-100 °C	20-760 °C	20 °C	760 °C	20 °C	760 °C
kg/dm³	°C	°C	W/m·K		10^{-6}/K		GPa		-	
8.29	1300	1375	10.3	25.8	12.1	14.6	217	170	0.319	0.354

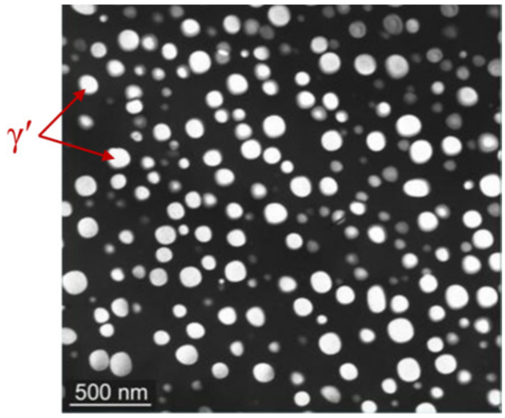

Figure 16. Microstructure of Haynes 282 showing γ' precipitates[44]

Figure 17 shows the temperature dependence of Haynes 282 tensile properties. The alloy exhibits less strength and higher ductility than alloys 718 and 718Plus at temperatures lower than around 700 °C. With rising temperature, however, its strength decreases slower.

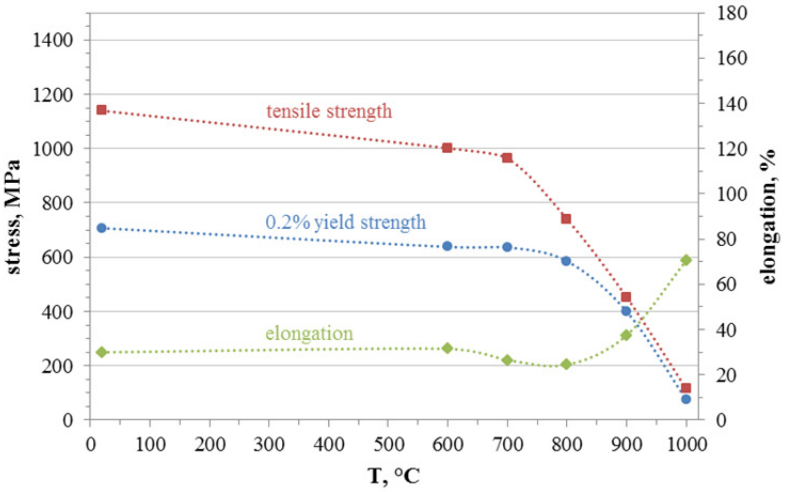

Figure 17. Tensile properties of Haynes 282 (adapted from [43])

3.3 Plasticity and deformed microstructure

Plastic deformation of cubic metals occurs due to dislocation glide or twinning. Former is the predominant deformation mechanism in bcc metals and fcc metals with moderate to high stacking fault energies (such as Ni). Typically, glide (or slip) takes place along the most tightly packed planes and directions of the lattice system (called slip system, {111}<110> for fcc metals). [13, 63]

Figure 18 shows several microstructural features of polycrystalline metals deformed by dislocation glide. During plastic deformation of a polycrystalline material, its dislocation density generally increases (Frank-Read mechanism). Furthermore, the crystal orientation inside a grain changes according to the direction of applied stress and with respect to boundary conditions arising from neighboring grains. These changes include crystallographic rotations and lead to a preferential grain orientation called *texture*. This texture varies with the extent of deformation. Generally, the deformation inside a grain is inhomogeneous which leads to regions of different crystallographic orientation inside the initial grain. In many metals (such as Ni), the majority of dislocations generated during plastic deformation form dislocation boundaries called *cells* or *subgrains* (see **Figure 18**). [63, 45]

In materials which do not form cells due to their low stacking fault energy, the formation of *deformation bands* (and deformation twins) is facilitated. Deformation bands are regions of constant crystallographic orientation inside grains and can be formed via two mechanisms. The first mechanism is based on the fact that different slip systems can be simultaneously activated by the imposed stress and, thus, crystallographic rotation can happen in different directions. According to the second mechanism, different grain regions may undergo different strains if the required energy is less than for homogeneous deformation and overall geometrical compatibility can be achieved. The most important influence factors on the formation of deformation bands are the deformation temperature as well as the orientation and size of initial grains. Typically, deformation banding is less likely to occur at high temperatures and small grain size. In contrast to deformation bands, *shear bands*, which are slim regions of strong shear, form through lattice rotations to geometrically preferential directions and can propagate transgranularly through the whole material. [63, 46]

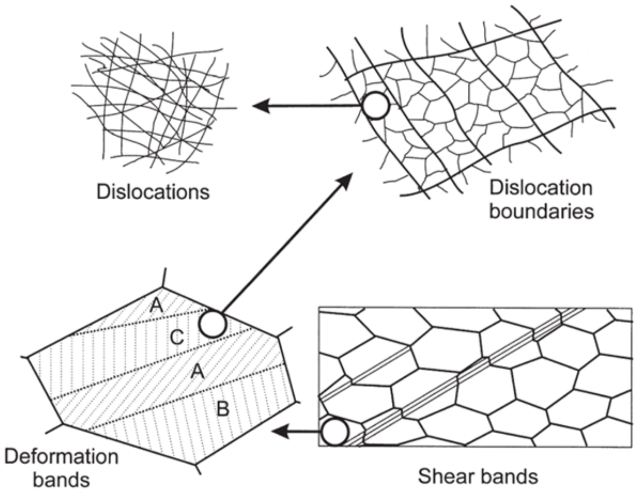

Figure 18. Microstructural features of polycrystalline metals deformed by dislocation glide [63]

3.4 Hot deformation mechanisms

3.4.1 Creep

Creep is defined as time-dependent plastic deformation of a material under constant stress (or load) and temperature. The temperature influence on creep is a result of diffusion processes which have a serious effect above about 40% of the material's melting temperature. **Figure 19** shows a typical creep curve representing the strain behavior of a material under creep conditions and the corresponding strain rate curve with the three stages of creep.

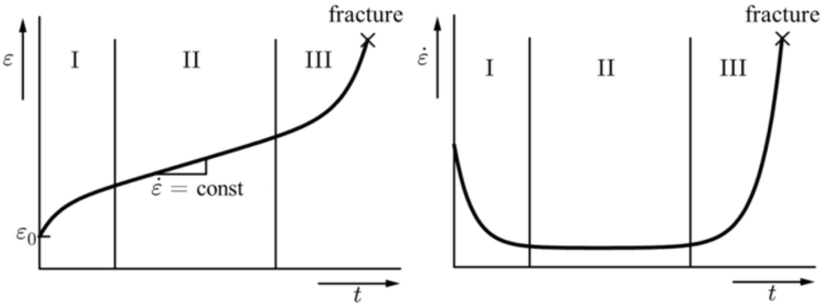

Figure 19. Typical creep curve (left) and corresponding strain rate curve (right) with the three stages of creep [47]

In the primary stage, fast initial plastic deformation takes place after preceding elastic deformation ε_0. However, the creep rate $\dot{\varepsilon}$ decreases due to a reduction of mobile dislocations during work hardening. [48]

The secondary period of creep is characterized by constant creep rate. In this *steady-state* (or power law) creep stage, $\dot{\varepsilon}$ reaches a minimum. This is due to a balance between strain hardening and dynamic recovery processes resulting in constant dislocation density. In general, the steady-state creep rate depends on the applied stress σ, the temperature T and the material's grain size d and can be predicted using constitutive power law relationships (Norton creep law) of the form

$$\dot{\varepsilon} = \frac{d\varepsilon}{dt} = K \frac{\sigma^n}{d^m} e^{-\frac{Q_C}{RT}} \qquad [1]$$

where K is a material constant, n the power law exponent, m the grain size exponent, Q_c the activation energy for creep and R the universal gas constant. [49, 50]

In the tertiary creep period the creep rate rapidly increases due to a degradation of the precipitate microstructure (Oswald ripening, see chapter 3.5.1) or the formation of pores and cracks which ultimately leads to fracture.

Figure 20 (left) shows the stress and temperature dependence of creep strain. Both an increase in stress and in temperature raises the slope of the curve and therefore the creep rate. In **Figure 20** (right) the influence of stress and grain size on the creep rate is shown. At lower stresses, increasing the grain size enhances the creep strength which stands in contrast with room temperature material behavior (Hall-Petch relationship). In general, the grain size dependence is believed to decrease at higher stresses when the creep mechanism changes from diffusion creep to dislocation creep. For many materials (such as Inconel 718), however, it was shown that the creep rate is still grain size dependent during dislocation creep conditions and that positive as well as negative grain size exponents are possible for different alloys. [50, 51]

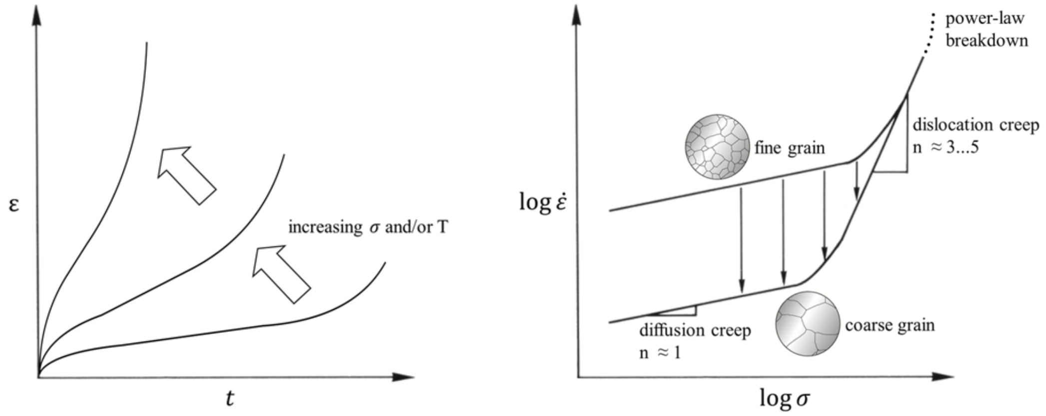

Figure 20. Stress and temperature dependence of creep strain (left) (adapted from [52]) and stress and grain size dependence of the creep rate (right) (adapted from [13])

3.4.1.1 Creep deformation mechanisms

The mechanical strength of metals and alloys generally decrease with increasing temperature and some of their properties become time-dependent. This is attributable to the following microstructural effects: [13, 49, 52]

- higher mobility of atoms and dislocations
- higher equilibrium concentration of vacancies
- activation of new slip systems
- precipitate coarsening (Oswald ripening)
- recrystallization and grain growth
- oxidation and corrosion

Creep is roughly categorized in diffusion and dislocation creep. Creep through grain boundary diffusion (*Coble creep*) has low activation energy, i.e. happens at relatively low temperatures and stresses. At higher temperatures, volume (or bulk) diffusion is predominant (*Nabarro-Herring creep*). **Figure 21** shows a schematic visualization of the two diffusion creep mechanisms and how diffusion creep leads to grain boundary sliding (which can be impeded by grain boundary precipitates). As these mechanisms are diffusion controlled, they can be mitigated by increasing the material's grain size (see also **Figure 20**, right). The power law exponent for diffusion creep typically ranges from 1 to 2.

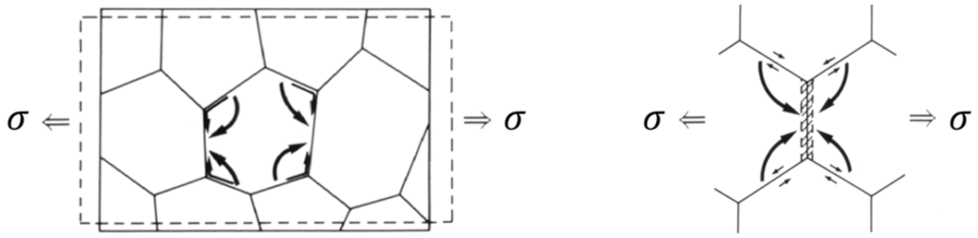

Figure 21. Creep deformation of a polycrystal via volume and grain boundary diffusion (left) and grain boundary sliding caused by volume diffusion (right) [13]

The second major creep mechanism, dislocation creep, is caused by movements of point defects (impurities or vacancies) in the crystal lattice and typically occurs at higher stresses. Dislocations can move by gliding in slip planes, i.e. planes with the closest packed atoms in the lattice system. If there are obstacles (i.e. stress fields caused by coherent precipitates, other dislocations or stacking faults) in their slip plane, dislocations need to climb over them in order to be able to further glide along. The gliding process causes nearly all the strain but the climbing process is the rate controlling mechanism as it requires vacancy diffusion and thus happens preferably at higher temperatures. **Figure 22** shows how diffusion leads to dislocation climb (left), how the climb-glide sequence leads to creep (center) and how dislocation cell structures form.[49]

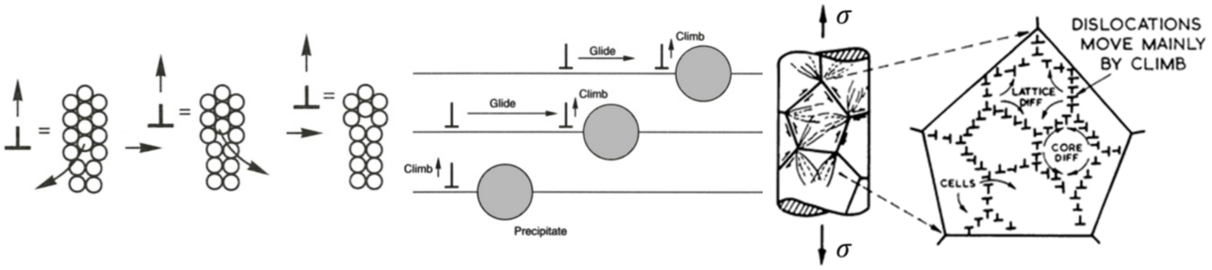

Figure 22. Dislocation climb mechanism (left) enabling dislocation creep via climb-glide sequences (center) leading to dislocation cell formation (right)[53, 54]

Typical power law exponent values for dislocation creep are around 3, 5 or 8. Latter is believed to occur for alloys which do not form subgrains during deformation, i.e. maintain unchanged microstructure due to the presence of stable precipitates or dispersoids.[55]

Figure 23 shows a schematic creep deformation mechanism map with characteristic deformation mechanisms. The ratio of the temperature T to the melting temperature T_m, called homologous temperature T_h, is assigned to the abscissa. The ordinate represents the normalized shear stress τ/G, where G is the material's shear modulus at T. The map is divided into fields which represent the dominant deformation mechanism for the particular mechanical and thermal load.

Beneath the theoretical strength (which the material would exhibit without imperfections), deformation is caused by dislocation glide. At lower stresses, dislocation climb (power law creep) is the dominant deformation mechanism. The field is divided into a low and high temperature region based on different diffusion mechanisms (see **Figure 22**, right). The diffusion creep field with the two discussed mechanisms is located in the low-stress and high temperature region of the deformation mechanism map and elastic deformation predominates mainly at lower temperatures.[53]

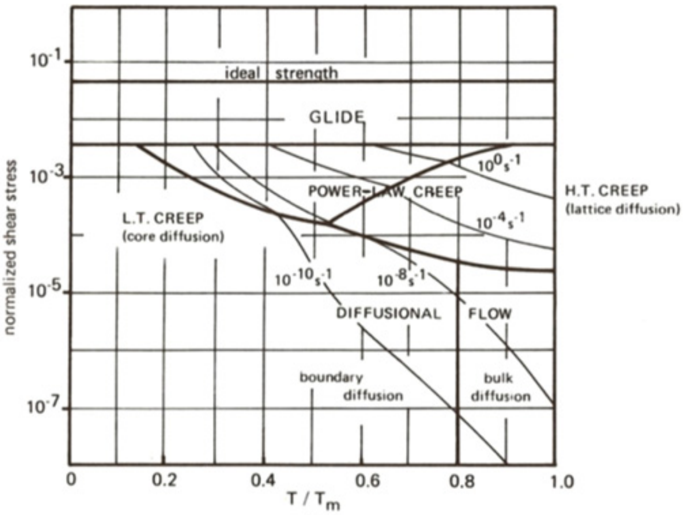

Figure 23. Schematic creep deformation mechanism map [56]

3.4.1.2 *Creep of alloys*

Creep resistance is effectively influenced by alloying, i.e. strengthening mechanisms caused by alloying elements. Depending mainly on the type and amount of solute atoms as well as the temperature, solid solution strengthening accounts for several modifications of the microstructure that influence creep behavior. The interaction of dislocations and substitutional atoms is influenced due to their respective (tensile or compressive) stress fields, resulting in an increase in the necessary stress to pass the atoms. Similar behavior arises from local changes in the shear modulus caused by solute atoms. Furthermore, as already mention in chapter 3.2.2, certain alloying elements reduce the effective diffusion coefficients and the stacking fault energy which is another way to decrease the creep rate. However, the most important mechanism to increase creep strength is strengthening via thermally stable, especially coherent, particles. The strengthening contribution of precipitates is a function of stress, temperature as well as particle size and volume fraction. Furthermore, it is influenced by the dislocation-particle interaction during deformation: cutting (only coherent particles), bypassing, climbing and drag. Cutting and bypassing of particles are temperature independent mechanisms and require certain stresses to occur. Therefore, diffusion controlled dislocation climb is often the rate controlling mechanism during high temperature deformation at intermediate stresses. [13, 49]

Figure 24 (left) shows the beneficial influence of particle strengthening on creep strength characterized by the denoted stress σ_{th}. This *threshold stress* (or *back stress*) takes dislocation pinning of particles into account and can be implemented in the constitutive equation [1] (see chapter 3.4.1) to describe the creep behavior of the respective particle-free material:

$$\dot{\varepsilon} = K\,(\sigma - \sigma_{th})^{n}\, e^{-\frac{Q_C}{R\,T}} \qquad [2]$$

There are different approaches for modeling the threshold stress which is believed to depend on the dislocation-particle interaction mechanism. In particle strengthened alloys, this mechanism changes with increasing stress from dislocation climb to particle cutting (small particles) or bypassing (larger particles).

In the case of bypassing (Orowan looping), the stress is typically modeled as a function of temperature, particle size and volume fraction. Lower particle size at constant phase fraction increases the Orowan stress (see **Figure 24**, right). In case of dislocation climb, however, the back stress is assumed to depend mainly on the external stress and less on the microstructure. [57-61]

Due to this change in the dislocation-particle interaction mechanism, particle strengthened alloys obtain larger stress exponents at higher stresses. A thorough description of modeling of back stresses depending on the predominant interaction mechanism in γ' strengthened superalloys is given by Stevens et al. [59]

In general, the creep rate increases in the course of creep loading due to particle coarsening (increasing precipitate size at constant volume fraction) as the number of dislocation-particle interactions decrease.

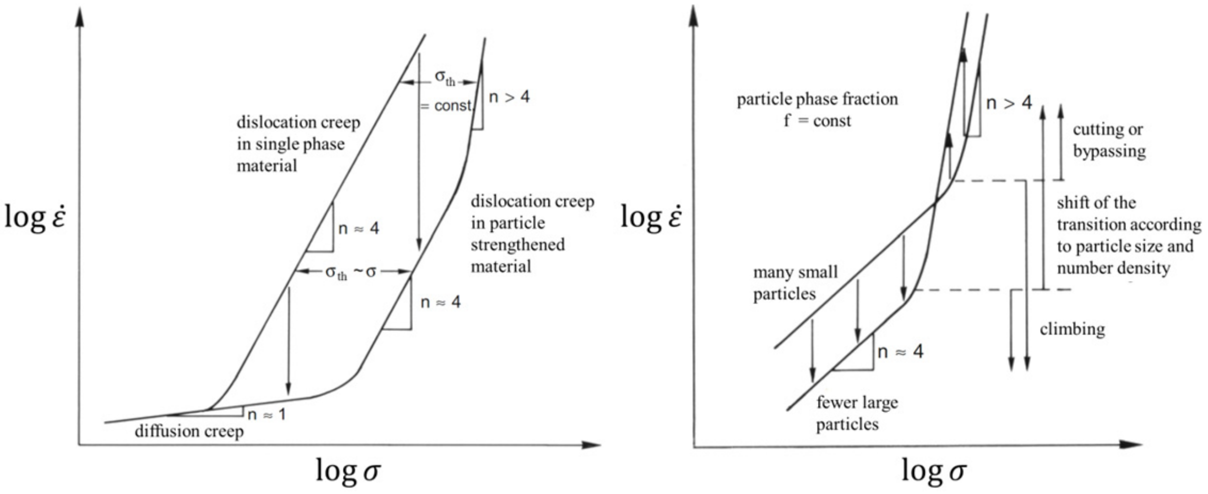

Figure 24. Schematic influence of particle strengthening on creep strength (left) and influence of particle size and dislocation-particle interaction mechanism on the creep rate (right) (adapted from [13])

Figure 25 shows deformation mechanism maps for pure nickel and a particle strengthened Ni-base superalloy (MAR-M200). In both maps, the typical stress-temperature profile of a turbine blade is highlighted by rectangular areas, revealing the strong difference between the materials' strain rates under these conditions and pointing out the excellent creep resistance of superalloys.

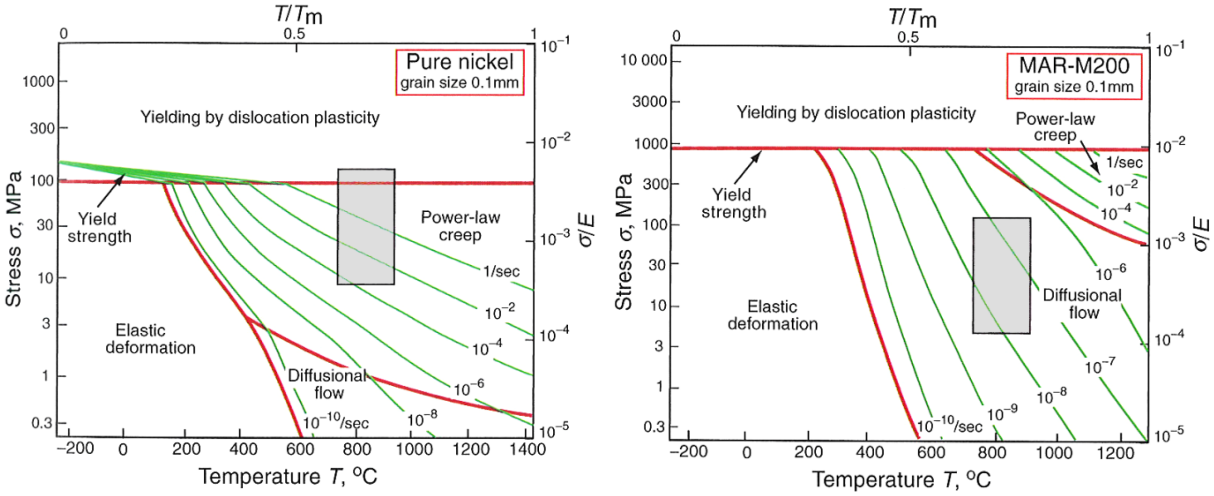

Figure 25. Deformation mechanism maps for pure Ni (left) and the Ni-base alloy MAR-M200 (right) [62]

3.4.1.3 Creep damage

During creep, the creep rate is typically raised due to microstructural changes such as altering dislocation and precipitate structures or the formation of pores and cracks. These pores and cracks are typically referred to as creep damage. Creep damage can occur at very low stresses, propagate at constant stress and is predominantly intergranular. After the formation of crack nuclei (which can occur already in the first stage of creep), they grow to micropores. The number of these pores increases proportionally with the creep strain until eventually micro- and macro-cracks form, typically in the third stage of creep (see **Figure 26**). **Figure 27** shows the two basic mechanisms responsible for creep damage. The first mechanism typically occurs at lower temperatures and is associated with vacancy diffusion due to high localized stresses at grain boundaries, resulting in the formation of pores (*cavities*). In the second mechanism, grain boundary sliding causes stress concentrations at triple points or grain boundary particles. If these stresses are not relaxed by diffusion processes or plastic deformation inside the grain, crack initiation of so called *wedge cracks* occurs. [13, 47, 52]

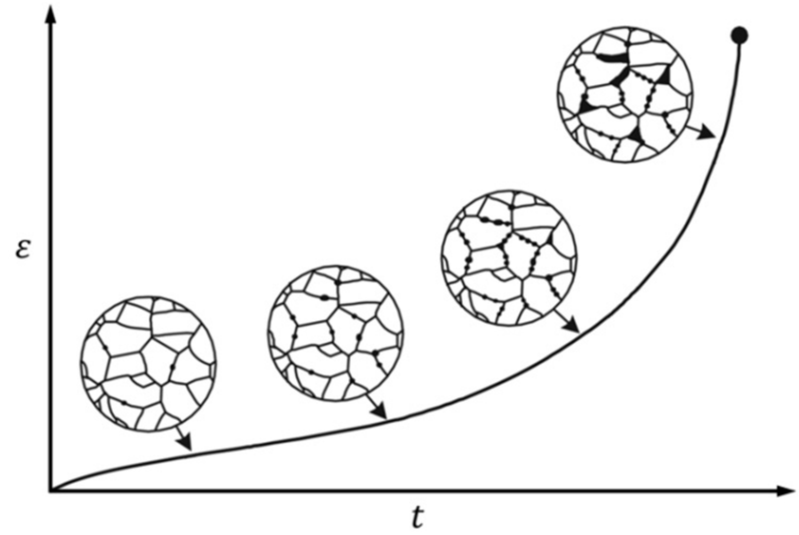

Figure 26. Development of creep damage (adapted from [13])

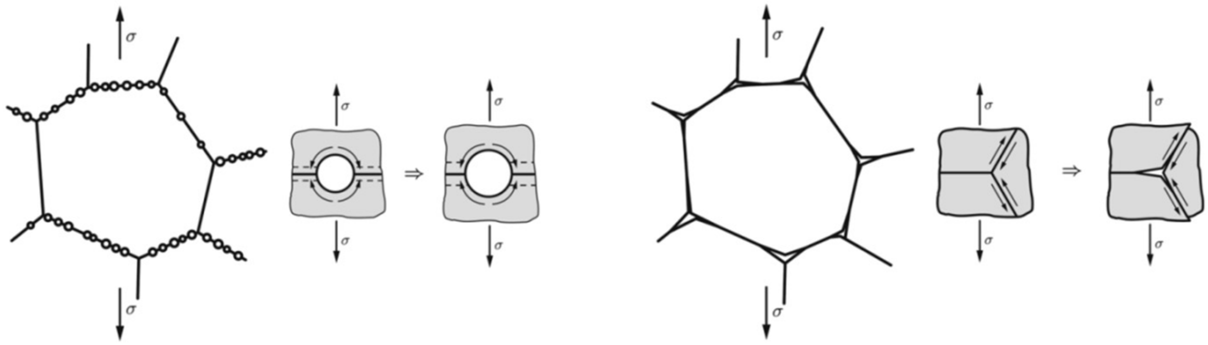

Figure 27. Creep damage formation at grain boundaries (cavities, left) and triple points (wedge cracks, right) [47]

3.4.2 Dynamic recrystallization

In dynamic recrystallization (DRX), deformed grains are replaced by new grains with lower dislocation density during deformation. In general, the driving force for recrystallization is the energy stored in the microstructure, i.e. the dislocation density. Therefore, certain preceding deformation of the microstructure is required to start the recrystallization of a grain to lower its internal energy and to maintain its growth into deformed material. The recrystallized grain size is determined primarily by the extent of deformation (i.e. the strain). For a given strain, the recrystallization temperature generally increases with increasing strain rate and initial grain size (as DRX preferentially occurs at grain boundaries). **Figure 28** shows the schematic microstructure of a polycrystalline material before (left) and after DRX (right). [63, 64]

For precipitation hardened alloys, the particle size and volume fraction has a strong influence on recrystallization kinetics. While a uniform dispersion of many small precipitates can inhibit recrystallization, it is accelerated by larger (typically > 1µm) particles due to *particle stimulated nucleation* in which recrystallization nuclei form directly on the precipitate surface. [63, 65]

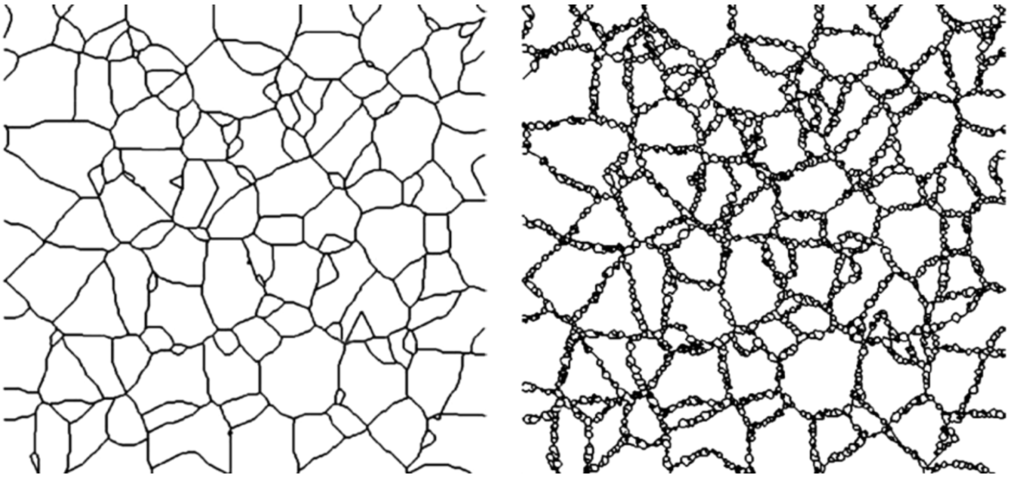

Figure 28. Polycrystalline microstructure before (left) and after partial dynamic recrystallization (right) [65]

Dynamic recrystallization may also occur during (dislocation) creep (see **Figure 29**). The changing dislocation substructure facilitates new waves of primary creep which drastically accelerates the creep rate.[54]

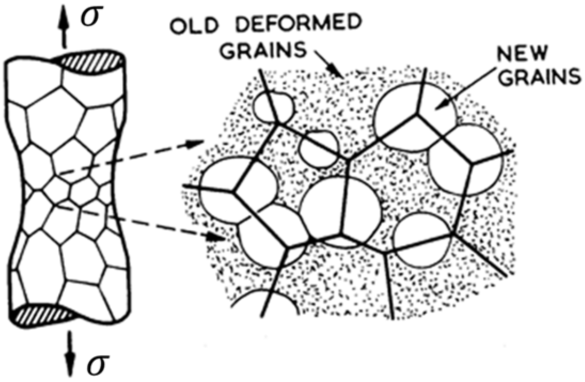

Figure 29. Dynamic recrystallization as a result of creep [54]

3.5 Microstructure modeling and numerical simulation

In general, great amount of experimental work is necessary in order to study the properties of engineering alloys during certain thermomechanical processes (such as cold or hot forming, heat treatment or service).

Mathematical models can help to explain material behavior during such processes. On one side, models are used to establish relations between processing parameters and the microstructural evolution of materials. On the other side, they help to understand the connection between their microstructure and mechanical properties.

Numerical simulations utilizing such models can therefore be used to predict the effects of a given process on material properties or, conversely, to design and/or optimize a process based on knowledge concerning material properties (see **Figure 30**).

However, models of physical processes are typically based on assumptions and simplifications which are often valid only for a limited range of process parameters or describe only certain mechanisms while neglecting others. Nevertheless, when supported by physical process simulations and microstructural investigations, numerical simulations able to predict the microstructural evolution of alloys are a very important tool for material development, processing and application.

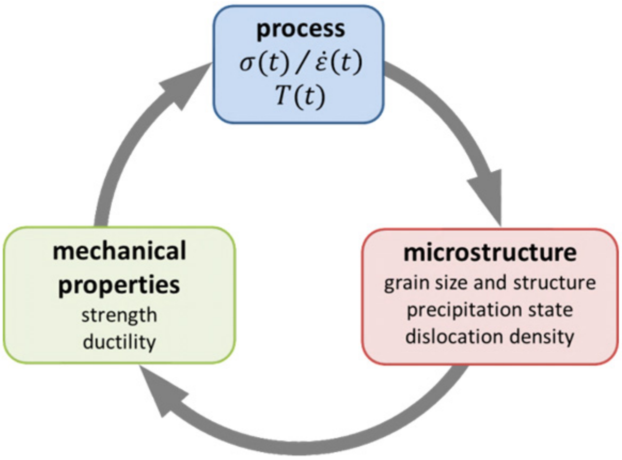

Figure 30. Principal relationship between technical processes, the microstructure of materials and its mechanical properties and their influence on each other

3.5.1 Theory of precipitation kinetics

Precipitation processes occur when the solubility limit of alloying elements in the matrix is exceeded at a certain temperature. **Figure 31** shows the left (i.e. high Ni content) parts of binary phase diagrams with Ti, Al and Nb and different phase regions. With increasing temperature, the fcc γ solid solution can solve more alloying elements which is the basis to achieve precipitation strengthening. Typically, at first, supersaturated solid solution is obtained by annealing in the according phase diagram region. Subsequent rapid cooling suppresses the formation of phase equilibrium enabling finely dispersed precipitation of desirable intermetallic phases during subsequent tempering carried out below the solution (or solvus) temperature of these phases.[13]

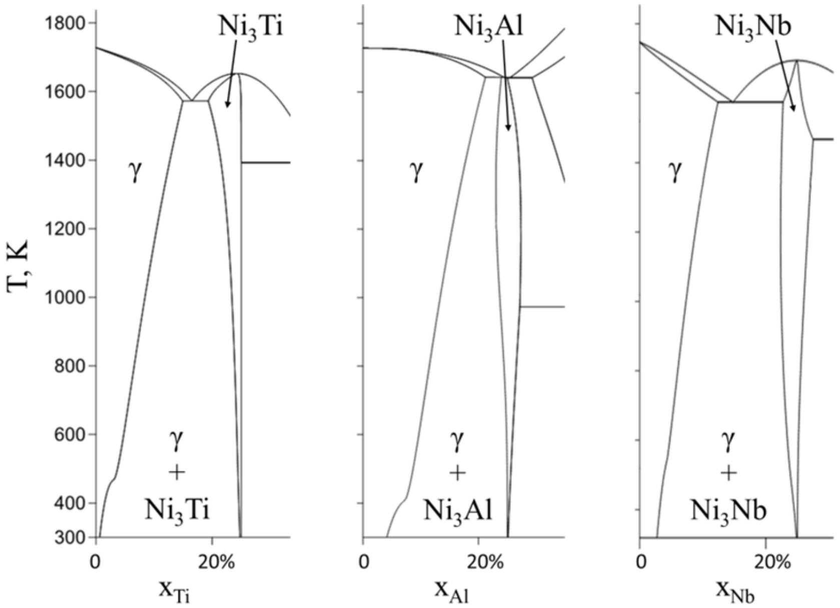

Figure 31. Binary phase diagrams of Ni and typical alloying elements with according intermetallic phases used for precipitation strengthening (adapted from [66])

Precipitation processes proceed in three phases. The first stage, nucleation, is a stochastic process which occurs due to the formation of atom clusters mainly via vacancy diffusion. Once a precipitate nucleus reaches a critical size (d^*), it starts growing due to chemical driving forces. This growth is typically proportional to $\sqrt{t}$ while the particle volume fraction (or phase fraction, f) increases roughly linearly (see **Figure 32**). In the third stage, small precipitates dissolve in favor of larger ones. In this process, the mean particle size increases proportional to $\sqrt[3]{t}$ while the volume fraction remains nearly constant (Oswald ripening). This leads to a steady increase of the inter-particle distance (λ) and, therefore, loss in strength.[13, 67]

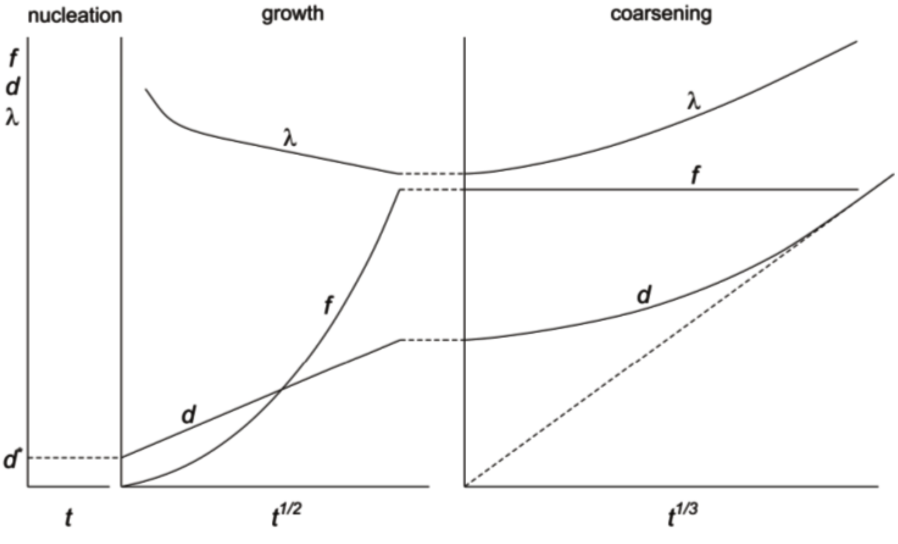

Figure 32. The three stages of precipitate evolution during thermal exposure (adapted from [13])

3.5.2 Numerical simulation software MatCalc

MatCalc[68] is a software package for the numerical simulation of thermodynamic equilibria and precipitation kinetics of multi-component and multi-phase materials using the *CALPHAD* approach. In this method, analytical expressions of Gibbs energy are modeled for each phase as a function of temperature, pressure and chemical composition.[69]

The software is based on the thermodynamic extremal principle of maximum entropy production in which thermodynamic forces are formulated in terms of chemical potentials. MatCalc utilizes databases containing comprehensive thermodynamic and diffusion data and calculates precipitate nucleation kinetics via classical nucleation theory extended for multi-component systems. Once a precipitate has nucleated and reached critical size, its growth rate and the rate of compositional change are obtained by solving linear systems of equations. Details on mathematical modeling, numerical solution and applications are given in work by Kozeschnik and Swoboda et al.[69-73]

Following parameters are needed for the definition of a system to be simulated in MatCalc:

- temperature profile and strain rate resulting from the process of interest
- chemical composition of the alloy
- matrix phases (i.e. precipitation domains)
- dislocation density as well as grain and subgrain size of the matrix phases
- precipitate phases
    - nucleation sites
    - shape
    - volumetric misfit
    - number of particle classes to be simulated
    - optional corrections of the nucleation rate or interface energy

Different precipitate phases are known to nucleate at different microstructural regions such as the bulk, dislocations, grain and subgrain boundaries or other precipitates. The number of nucleation sites available in the matrix phase is therefore determined by its grain and subgrain size as well as its dislocation density. The nucleation rate is directly proportional to the available number of nucleation sites. For this reason, sufficient information about the initial microstructure is of great importance in order to properly predict its evolution in the numerical simulation.

Furthermore, the nucleation rate strongly depends on the interfacial energy of precipitates. MatCalc calculates phase interface energies using a generalized nearest-neighbour broken-bond approach assuming planar and sharp phase interfaces.[74] This approach is rather inaccurate, especially for spherically shaped precipitates near their solvus temperature. For this reason, interface energy correction can be necessary in certain situations. Radis et al., for instance, suggested temperature dependent interface energy correction for γ' and δ phases in Allvac 718Plus to fit experimental data.[75]

MatCalc has been successfully utilized to predict the microstructure of Ni-base superalloys during annealing processes.[35, 76, 77, 78]

4 Experimental

4.1 Materials

For thermomechanical testing, tensile samples of the three studied alloys (Inconel 718, Allvac 718Plus and Haynes 282) were fabricated and heat-treated as described in the following chapters.

4.1.1 Inconel 718

4.1.1.1 Chemical composition

Table 11 shows the measured chemical composition of the received Inconel 718 forged billet according to the manufacturer *Special Metals*.

Table 10. Measured chemical composition of Inconel 718 billet, wt.%

Ni	**Co**	**Cr**	**Fe**	**Cu**	**Mo**	**Nb**	**Ti**	**Al**	**C**	**B**	**Mn**	**Si**	**P**	**S**
53.21	0.15	19.32	bal.	0.03	2.99	5.2	0.95	0.49	0.022	$37 \cdot 10^{-6}$	0.06	0.11	0.007	max. 0.001

4.1.1.2 Sample preparation and heat treatment

A cylindrical billet of Inconel 718 was received from BSTG (see **Figure 33**) and heat-treated at IWS laboratory in a muffle furnace with an internal type S thermocouple (PtRh-Pt). Before heat treatment, the temperature distribution in the furnace chamber was measured with additional type K thermocouples (NiCr-Ni) and a multimeter (*BBC Goerz Metrawatt M4052*).

The thermocouples were placed at different locations inside the chamber. It was shown that the temperature gradient in the measurement area was negligible but the internal thermocouple apparently showed too high temperatures. For this reason, the heat treatment was performed with additional thermocouples fixed onto the billet in order to monitor its surface temperature at different positions.

At first, the billet was solution annealed at 1010 °C in standard atmosphere for one hour and subsequently air cooled. After that, a 10 mm disk was cut with a band-saw and metallographic samples were cut out at different positions of the disk. This was done to examine the homogeneity of the microstructure over the billet's cross section.

The resulting micrographs indicated a certain inhomogeneity of the microstructure (see chapter 5.2.1.1). Grain size and the distribution of large particles differed rather strongly from the billet's center to the border which is most likely attributable to the lower cooling rate of the center.

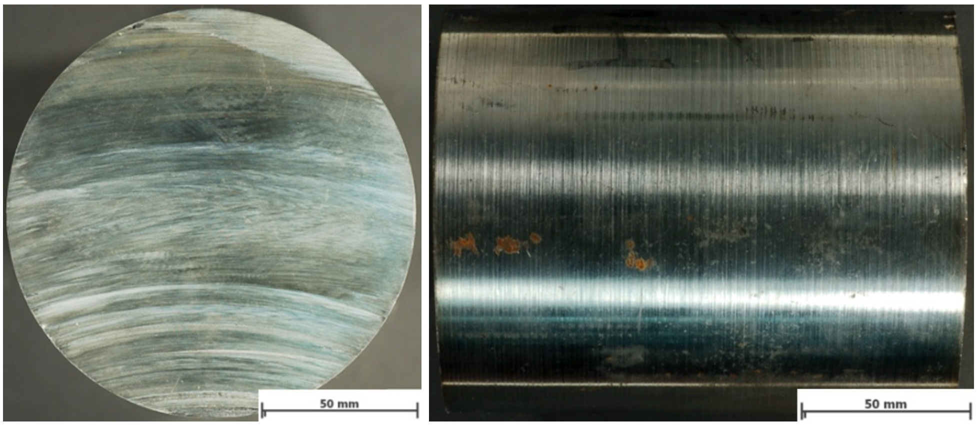

Figure 33. Inconel 718 billet

Therefore, in order to obtain a more uniform microstructure of all samples, they were fabricated to net-shape (except for the threads) via wire-cut electrical discharge machining before heat treatment. Cylindrical samples were cut out parallel to the billet's longitudinal axis (see **Figure 34**, left).

Heat treatment of the samples was then again carried out at standard atmosphere in a muffle furnace while monitoring their temperature via an external type K thermocouple. The temperature profile consisted of another hour of solution annealing at 1010 °C and subsequent precipitation hardening at 788 °C for six hours, each step followed by air cooling (see **Figure 34**, right). The high solution annealing temperature was chosen to solubilize as much Nb as possible and therefore prevent the element from being bound in δ phase. This enables the precipitation of a high amount of γ'' phase during tempering.

The obtained microstructure was examined by producing metallographic samples from waste pieces after both solution annealing and precipitation hardening.

Finally, threads were machined on the cylindrical samples and, before carrying out the thermomechanical tests, a small burr remaining on the specimens after electrical discharge machining was removed using grinding paper.

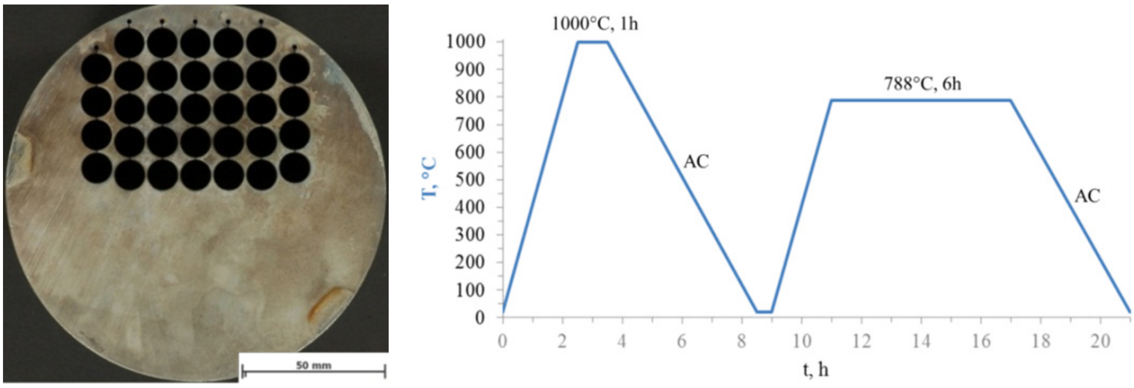

Figure 34. Sampling positions of Inconel 718 tensile samples (left) and conducted heat treatment (right)

4.1.2 Allvac 718Plus

4.1.2.1 Chemical composition

Table 11 shows the measured chemical composition of the received Allvac 718Plus forged billet according to the manufacturer *ATI*. The stated values are averaged between two measuring positions (billet top and bottom).

Table 11. Measured chemical composition of Allvac 718Plus billet, wt.%

Ni	Co	Cr	Fe	Cu	Mo	W	V	Nb	Ti	Al
bal.	9.16	17.92	9.34	0.02	2.695	1.00	0.03	5.50	0.75	1.51

C	B	N	Mn	Si	Zr	Ta	Mg	Sn	P	S
0.022	0.0045	0.00555	0.06	0.06	max. 0.01	max. 0.01	0.00125	0.0031	0.009	max. 0.0003

4.1.2.2 Sample preparation and heat treatment

As for Inconel 718, a pre-cut cylindrical billet of Allvac 718Plus in as-forged condition was used for the tensile specimen fabrication. The billet was heat-treated at BSTG according to **Figure 35**. Solution annealing (968 °C for 1 h) was carried out at intermediate temperature in order to obtain around 2-4% δ phase. Precipitation hardening consisted of a two-stage tempering treatment at 788 °C and 704 °C, respectively, with intermediate furnace cooling (cooling rate 56 °C/h).

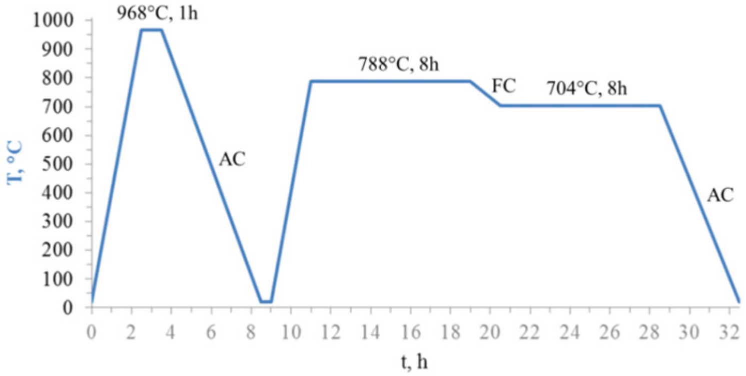

Figure 35. Heat treatment of Allvac 718Plus

In contrast to Inconel 718, tensile samples were taken from Allvac 718Plus billet perpendicular to its longitudinal axis via wire-cut electrical discharge machining (see **Figure 36**).

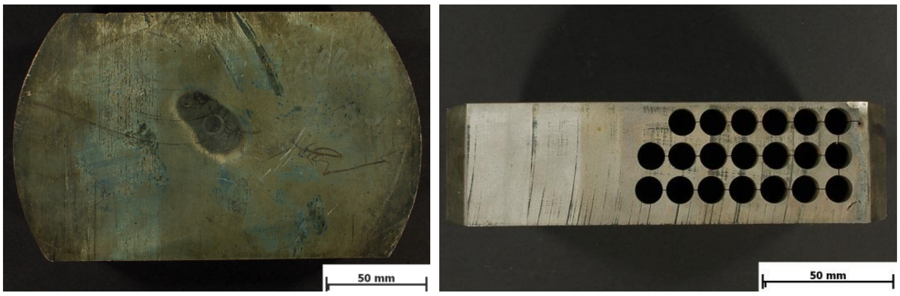

Figure 36. Allvac 718Plus billet and sampling positions of tensile specimens

4.1.3 Haynes 282

4.1.3.1 Chemical composition

Table 12 shows the measured chemical composition of the received Haynes 282 forged billet according to the manufacturer *Haynes International*. As for Allvac 718Plus, the shown values are averaged between two measuring positions (billet top and bottom).

Table 12. Measured chemical composition of Haynes 282 billet, wt.%

Ni	Co	Cr	Fe	Cu	Mo	W	Nb	Ti	Al
bal.	10.375	19.445	0.79	max. 0.01	8.52	max. 0.01	max. 0.1	2.125	1.57

C	B	Mn	Si	Zr	Ta	Mg	P	S
0.0615	0.004	0.04	0.05	max. 0.002	max. 0.01	0.003	max. 0.002	max. 0.002

4.1.3.2 Sample preparation and heat treatment

A pre-cut billet in solution annealed condition (1150 °C for 1 h) was the basis for Haynes 282 tensile samples. Two-stage tempering (1010 °C for 2 h and 788 °C for 8 h, respectively) was performed at BSTG according to **Figure 37**.

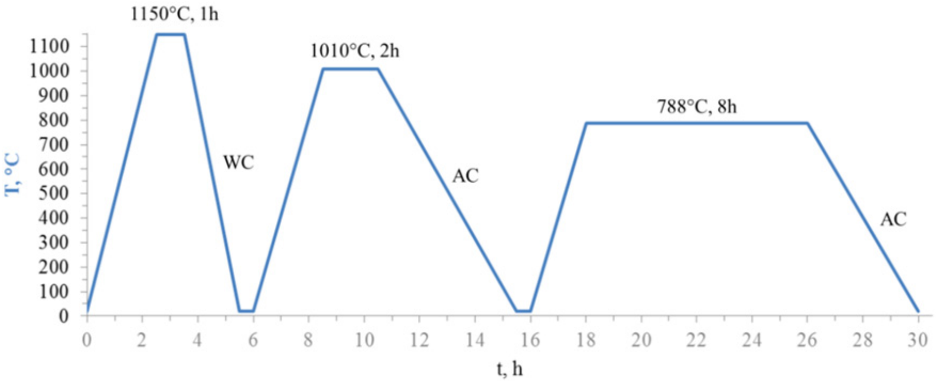

Figure 37. Heat treatment of Haynes 282

Tensile samples were cut from Haynes 282 billet perpendicular to its longitudinal axis (see **Figure 38**).

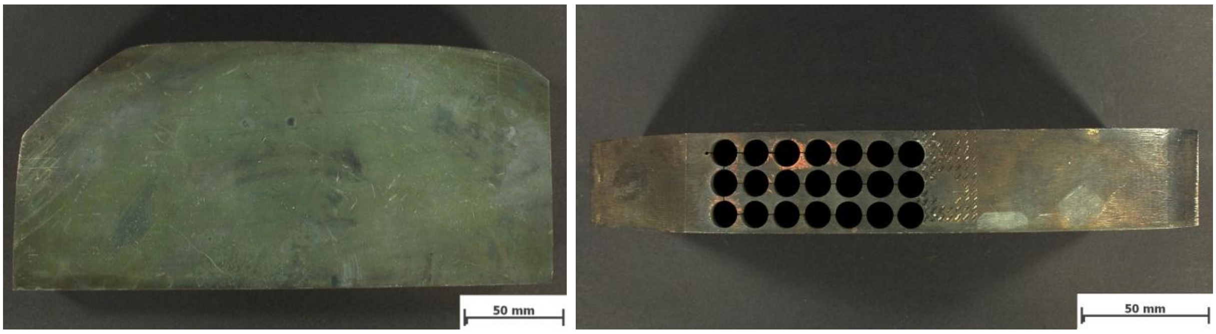

Figure 38. Sampling positions of Haynes 282 tensile specimens

4.2 Thermomechanical testing

Thermomechanical testing was carried out using a *Gleeble 3800* testing system to reproduce the conditions during forging of turbine blades in a physical simulation. The real temperature profile of the thermomechanical tests cannot be published due to confidentiality agreements. All parameters are proprietary of Böhler Schmiedetechnik GmbH & Co KG.[79, 80, 81]

4.2.1 Physical forging simulation

The task of the physical forging simulations was to simulate the mechanical and thermal material load of the real forging process as realistic as possible. **Figure 39** shows CAD models of the turbine blade forging and the lower die which is exposed to the highest temperature and load cycles.

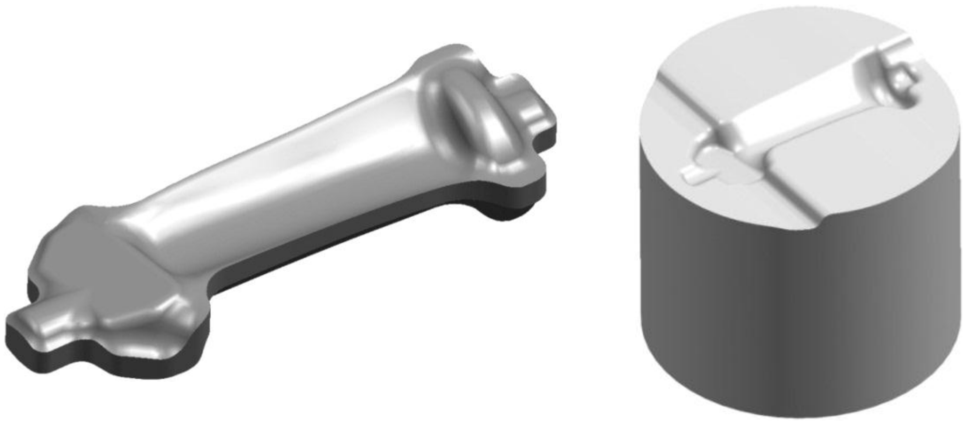

Figure 39. Model of the turbine blade forging (left) and the lower forging die (right)

Temperatures and stresses occurring in the real process were obtained from elastic-plastic FEM simulations in *DEFORM-3D* at BSTG.

The forging procedure is as follows: Prior to forging, the dies are heated inductively to a defined surface temperature measured via pyrometer. Due to the long heating-up time of around two hours and a holding time of 30 minutes it can be assumed that their temperature distributions are homogeneous at that point.

Subsequently, the pre-formed and pre-heated work piece with a temperature above 1200 °C is placed onto the lower die which consequently heats up. Around five seconds later, the upper die touches the work piece and the forging process starts. The process (and therefore the contact between both dies and the work piece) lasts between 30 seconds and one minute. Subsequently, the upper die is lifted and the work piece is removed from the lower die which lasts between 20 seconds and one minute.

After cleaning with a crowbar and compressed air as well as lubricating, the die is closed in order to achieve temperature balance. The next forging cycle starts after around two minutes. **Figure 40** shows the simulated temperature and stress distributions of the lower die during forging.

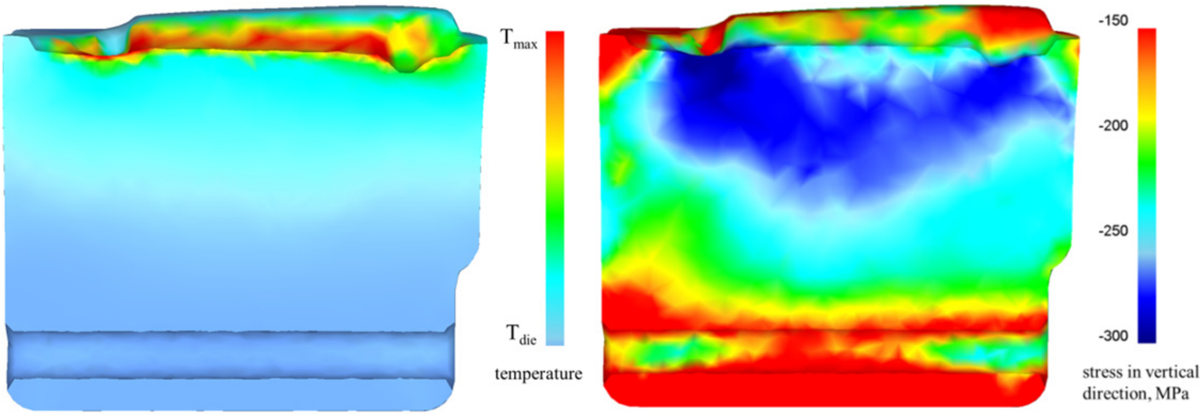

Figure 40. Temperature (left) and stress distribution of the lower die during forging (right)

The temperature of the die's central and lower section (T_{die}) is assumed to stay at a constant level throughout the whole process. Temperature and stress at the most heavily loaded zone of the die surface were used as input parameters for the physical forging simulation. The simulations were executed on a Gleeble 3800 testing system using tensile samples (see **Figure 41**). This sample geometry was chosen because of the possibility to load it in compressive as well as tensile direction which was necessary as the dies are exposed to compressive as well as tensile stresses in the course of the real forging process.

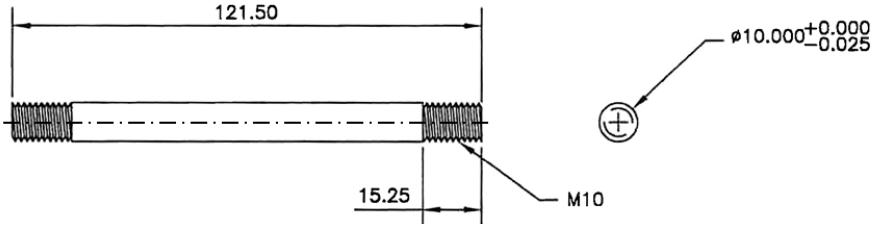

Figure 41. Tensile sample for physical forging simulation

During forging, the die surface is loaded with compressive stress due to the forging force. This mechanical stress is accompanied by thermal stresses which result from temperature gradients inside the die. These thermal stresses occur due to prevented material extension and can be positive or negative. For the uniaxial stress state (and therefore tensile specimens), this strain constraint can be expressed according to

$$\varepsilon = \frac{\sigma}{E} + \alpha \, \Delta T = 0 \tag{3}$$

where E is the modulus of elasticity and α the coefficient of thermal expansion (CTE). The resulting thermal stress σ_t is obtained by solving the equation for σ:

$$\sigma_t = -E \, \alpha \, \Delta T \tag{4}$$

For an assumed maximum die surface temperature T_{max} due to heat input via the hot work piece and a minimum temperature T_{min} due to cleaning and lubricating, the temperature difference ΔT is 90 °C during and -70 °C after forging, respectively. This leads to an exposure of the die surface to compressive stress σ_{tX} during forging ($\Delta T > 0$) and tensile stress σ_{tY} after forging ($\Delta T < 0$).

Figure 42 shows a schematic illustration of the lower die during a whole forging cycle with the assumptions concerning stresses and temperatures. The maximum stress values used in the forging simulation were based on the resulting maximum equivalent *von Mises stress* and the maximum stress in vertical direction, respectively, obtained from FEM simulations in which mechanical (σ_m) and thermal shares (σ_t) were considered:

$$\sigma = \sigma_m + \sigma_t \tag{5}$$

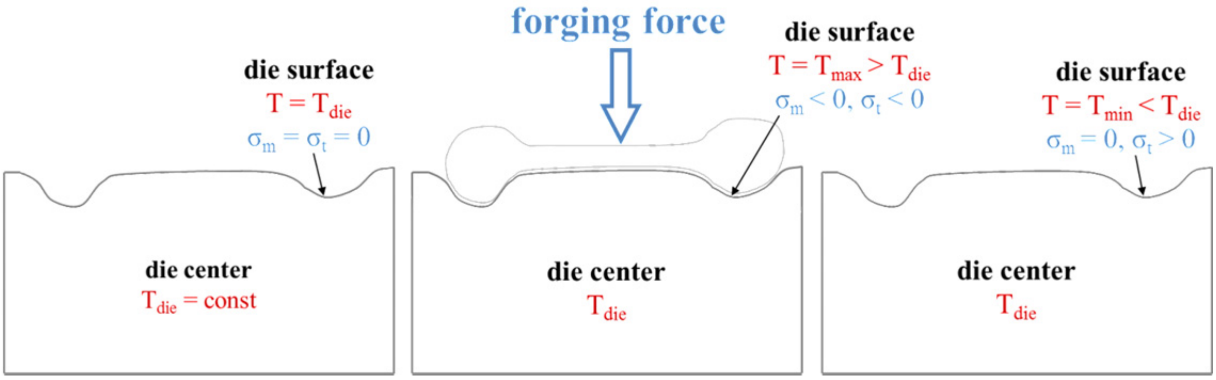

Figure 42. Schematic illustration of the lower die before (left), during (center) and after forging (right)

The physical forging simulations were carried out stress controlled. Therefore, no direct consideration of the thermal stresses due to strain constraint was possible for which reason this thermal share was added to the external specimen load. **Figure 43** shows the thermal and mechanical cycles of the physical forging simulation with the stress components resulting from abstraction of the real forging process. The total stress σ was used as mechanical control variable during the tests. The highest compressive stress occurring during the forging cycles is denoted as maximum stress (σ_{max}) as it obtains the highest absolute value.

The following parameters were chosen for the temperature and stress profiles in order to make the tests both realistic and time-efficient:

- heating-up time from room temperature to T_{die}	20 s
- holding time at T_{die}	5 s
- heating-up time from T_{die} to T_{max} and load build-up to σ_{max}	15 s
- holding time at T_{max}	40 s
- load duration at σ_{max}	30 s
- load decay to σ_{tX}	5 s
- load duration at σ_{tX}	5 s
- cooling-down time from T_{max} to T_{die} and load decay to $\sigma = 0$	10 s
- holding time at T_{die} and $\sigma = 0$	5 s
- cooling-down time from T_{die} to T_{min} and load build-up to σ_{tY}	5 s
- holding time at T_{min} and σ_{tY}	0 s
- heating-up time from T_{min} to T_{max} and load build-up to σ_{max}	20 s
- etc.	

These parameters result in a total forging cycle duration of 80 s which is around 150% to 250% faster compared to the real process.

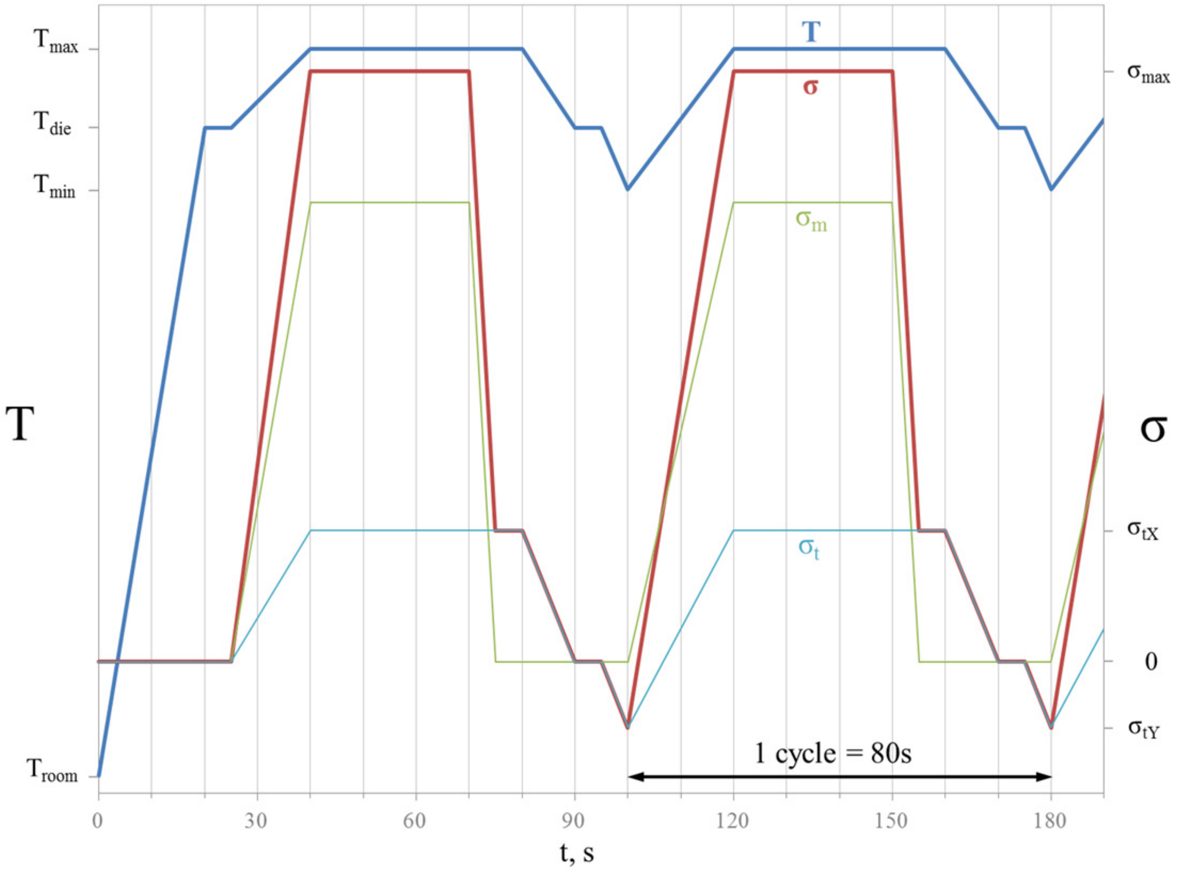

Figure 43. Thermal and mechanical load cycles used in physical forging simulations

In order to gain insight into the material behavior under different loading conditions and to consider possible future changes of the forging force, the maximum compressive stress σ_{max} was varied. A total of 36 specimens were tested at maximum stress values between -300 and -450 MPa (see **Table 13**) for different amounts of simulated forging cycles.

Table 13. Specimen designations and testing conditions

		σ_{max}		
		-450 MPa	**-350 MPa**	**-300 MPa**
specimen no.	**Inconel 718**	1, 2, 3	4, 5, 9, 10, 13	6, 7, 8, 11, 12
	Haynes 282	0, 7, 8, 11	2, 3, 5, 9	1, 4, 6, 10
	Allvac 718Plus	0, 5, 8	1, 2, 6, 9	3, 4, 7

4.2.2 Calibration measurement for thermal stresses

Thermal stresses resulting from a change in the die surface temperature during and after forging were calculated and verified by measurements. In these measurements, specimens were heated from room temperature to T_{die} force-controlled to simulate free specimen extension. The control mode was then changed to extension and the specimens were heated to T_{max} and subsequently cooled to T_{min} (see **Figure 44**).

During this thermal cycle, the specimen extension was held zero to simulate strain constraint and, thus, to measure the resulting thermal stresses σ_{tX} and σ_{tY}.

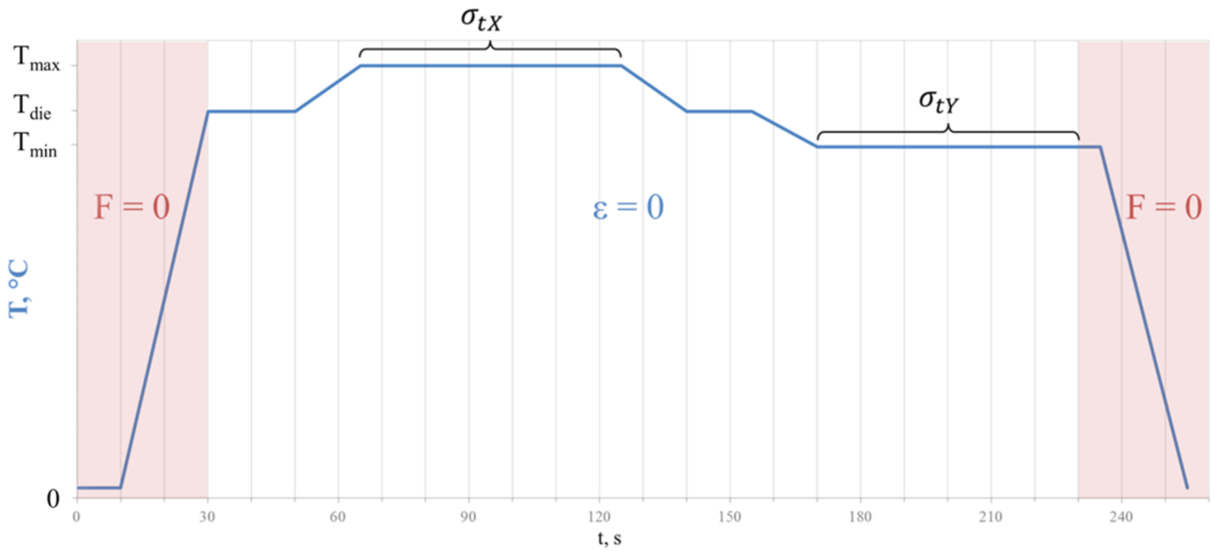

Figure 44. Temperature cycle used for calibration measurements

4.2.3 Gleeble 3800 testing system

All thermomechanical tests were carried out on a *DSI Gleeble 3800* testing system used for material testing and physical simulation (see **Figure 45**). All necessary signals to control different variables (such as force, extension or temperature) are provided by a digital closed-loop mechanical and thermal control system. [82]

Figure 45. Gleeble 3800 testing system used for thermomechanical testing [82]

The device contains a resistance heating system for heating rates of up to 10 000 °C/s. Specimens are clamped with high thermal conductivity jaws and can be optionally quenched with air, inert gas or water to achieve cooling rates of up to 10 000 °C/s (depending on sample geometry and temperature). Thermocouples welded to the specimen provide signals for specimen temperature control, allowing the realization of practically any desired thermal cycle due to their accuracy and fast thermal response.

The Gleeble 3800 hydraulic servo system is capable of exerting static forces of up to 98 kN in tension and 196 kN in compression with a maximal strain rate of 2000 mm/s.

Force and displacement are measured via load cells and linear variable differential transformer transducers. Available control modes include force, stroke, (true or engineering) stress or strain as well as signals from external extensometers.

Depending on the desired mechanical testing principle (such as compression/tension or torsion) and deformation speed, the system can be equipped with different mobile conversion units. For this work, the basic pocket jaw unit for compressive and tensile tests was used. **Figure 46** shows the setup of the system's sample chamber with its most important components.

The mechanical and thermal control modes, status messages as well as all control and measured variables can be monitored on a status display before and during tests (see **Figure 47**). Adjacent control knobs are used to set the respective variables zero and, in the case of *stroke*, move the shaft for specimen assembly before a test.

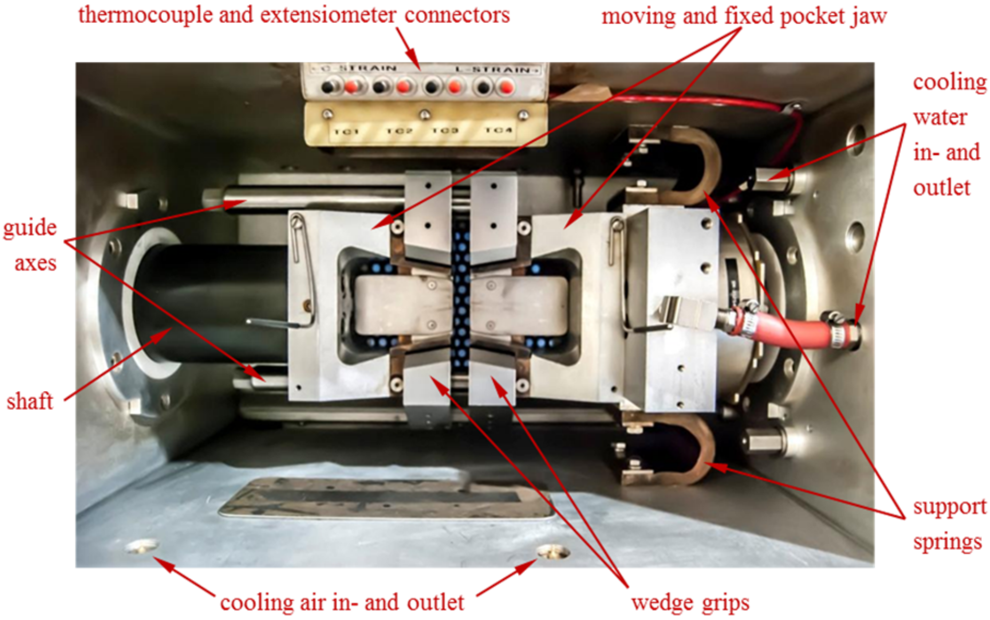

Figure 46. Gleeble 3800 sample chamber

```
137:HZT071 module passed.
139:Self test passed.
 17:Checking autoexec ...
 15:Running autoexec
 67:User Connected
115:VALUED CUSTOMER logged in
163:67.1GiB disk space free
```

MechMode: Stroke
Force: -0.0kN (-0.3kN)
CGauge: -0.00mm (0.00mm)
HZT071: -0.00mm (0.05mm)
Pram: 0.00
AirRamPres: 0.0kN
Strain: 0.00
Stress: -0.00MPa
TC1: 8000C K
TC2: 8000C K
TC3: 8000C K
TC4: 8000C S
SysTime: 14:50:56
OilTemp: 30C
PowAngle: 0%
vacState: vStandby
chamberRead: 5.9x10^1torr
diffPres: 0.0x10^0torr
RunTime: 01:46:32
Trouble
PanicSafety ●
DoorSafety ●
TempMode: TC1
PTemp: 0
TempTrim: 0C
ConTemp: 8000
Stroke: -0.00mm (-51.26mm)

Figure 47. Gleeble 3800 status display

The desired thermal and mechanical load cycles as shown in **Figure 43** were defined in the application software *QuikSim 2*. **Figure 48** shows a screenshot of the program for a typical test with a maximum stress of -350 MPa, three thermocouples (TC1-TC3) and 1000 desired forging cycles.

The data obtained from thermomechanical tests was processed and visualized using the data analysis software *OriginPro 8*. Curve smoothing was accomplished via Fast Fourier transform (FFT) filtering.

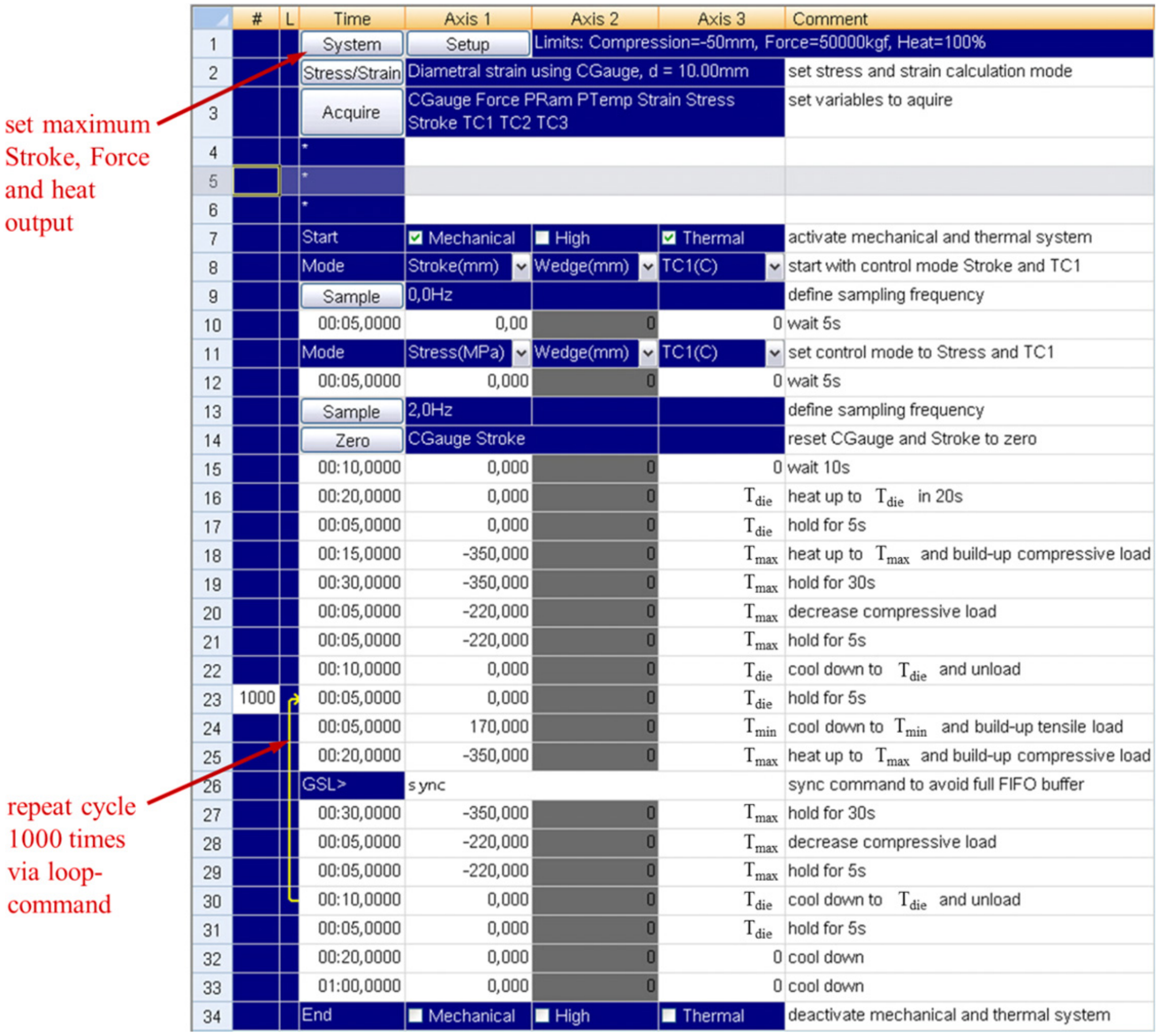

set maximum Stroke, Force and heat output

repeat cycle 1000 times via loop-command

	#	L	Time	Axis 1	Axis 2	Axis 3	Comment
1			System	Setup	Limits: Compression=-50mm, Force=50000kgf, Heat=100%		
2			Stress/Strain	Diametral strain using CGauge, d = 10.00mm			set stress and strain calculation mode
3			Acquire	CGauge Force PRam PTemp Strain Stress Stroke TC1 TC2 TC3			set variables to aquire
4			*				
5			*				
6			*				
7			Start	☑ Mechanical	☐ High	☑ Thermal	activate mechanical and thermal system
8			Mode	Stroke(mm)	Wedge(mm)	TC1(C)	start with control mode Stroke and TC1
9			Sample	0,0Hz			define sampling frequency
10			00:05,0000	0,00	0	0	wait 5s
11			Mode	Stress(MPa)	Wedge(mm)	TC1(C)	set control mode to Stress and TC1
12			00:05,0000	0,000	0	0	wait 5s
13			Sample	2,0Hz			define sampling frequency
14			Zero	CGauge Stroke			reset CGauge and Stroke to zero
15			00:10,0000	0,000	0	0	wait 10s
16			00:20,0000	0,000	0	T_{die}	heat up to T_{die} in 20s
17			00:05,0000	0,000	0	T_{die}	hold for 5s
18			00:15,0000	-350,000	0	T_{max}	heat up to T_{max} and build-up compressive load
19			00:30,0000	-350,000	0	T_{max}	hold for 30s
20			00:05,0000	-220,000	0	T_{max}	decrease compressive load
21			00:05,0000	-220,000	0	T_{max}	hold for 5s
22			00:10,0000	0,000	0	T_{die}	cool down to T_{die} and unload
23	1000		00:05,0000	0,000	0	T_{die}	hold for 5s
24			00:05,0000	170,000	0	T_{min}	cool down to T_{min} and build-up tensile load
25			00:20,0000	-350,000	0	T_{max}	heat up to T_{max} and build-up compressive load
26			GSL>	sync			sync command to avoid full FIFO buffer
27			00:30,0000	-350,000	0	T_{max}	hold for 30s
28			00:05,0000	-220,000	0	T_{max}	decrease compressive load
29			00:05,0000	-220,000	0	T_{max}	hold for 5s
30			00:10,0000	0,000	0	T_{die}	cool down to T_{die} and unload
31			00:05,0000	0,000	0	T_{die}	hold for 5s
32			00:20,0000	0,000	0	0	cool down
33			01:00,0000	0,000	0	0	cool down
34			End	☐ Mechanical	☐ High	☐ Thermal	deactivate mechanical and thermal system

Figure 48. QuikSim 2 program for physical forging simulations

4.2.3.1 *Temperature measurement*

Depending on the desired testing temperature range, different thermocouple types are suitable to measure and control the specimen temperature. For this work, type K thermocouples (NiCr-Ni) were used because of their low cost, uncomplicated weldability to Ni-base alloy specimens and sufficient maximum operating temperature of 1372°C. [83]

Thermocouple wires with a diameter of 0.2 mm were welded on the middle of each specimen perpendicular to its axis 1 mm apart from each other using a *DSI Thermocouple Welder 35200* (see **Figure 49**).

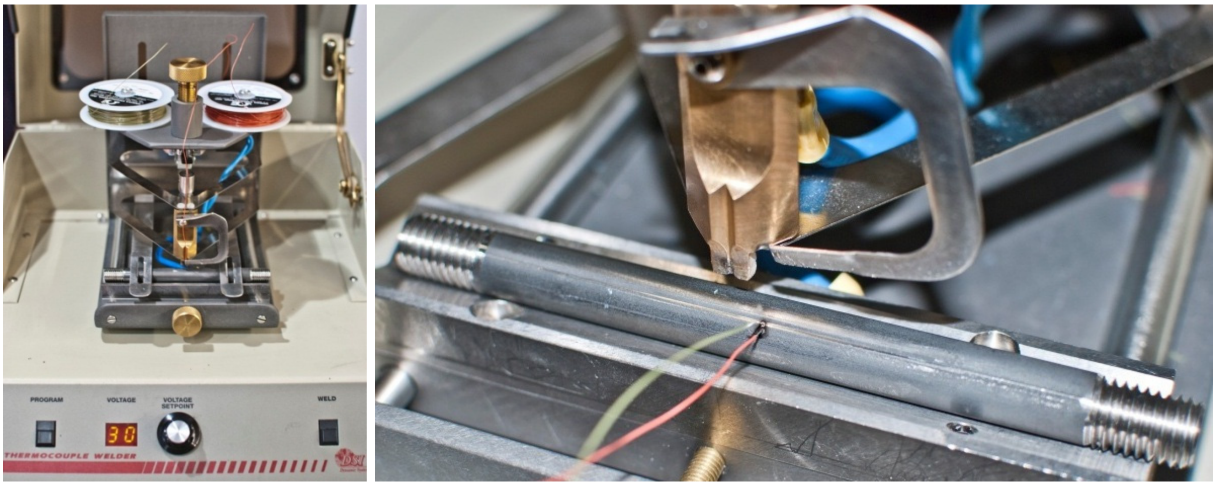

Figure 49. Thermocouple Welder (left) and thermocouple wires welded on a tensile specimen (right)

4.2.3.2 *Specimen clamping*

For the physical simulation of the forging process, the tensile specimens needed to be firmly fixed in axial direction. This was done in a two-stage clamping process. At first, the specimen was clamped in tensile direction pneumatically via copper jaws and locking nuts (see **Figure 50**, left). Subsequently, clamping in the opposite (compressive) direction from both sides was achieved via counterpieces consisting of shims, setscrews and nuts (see **Figure 50**, right).

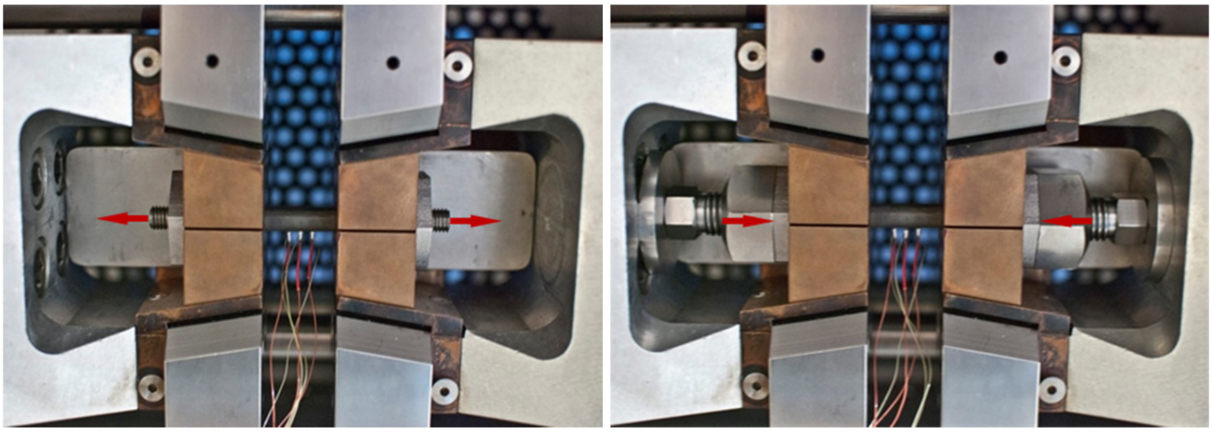

Figure 50. Two-stage clamping process of the tensile specimens in tensile (left) and compressive direction (right)

4.2.3.3 Stress and strain measurement

During the thermomechanical tests, specimen stress and strain had to be precisely determined. Therefore, instead of using the machine's stroke displacement signal, the specimen extension was measured directly on the specimen surface with external extensometers. This was done to eliminate the influence of thermal expansion and elastic deformation of machine components which ultimately results in measurement errors.

For the physical forging simulation, an *Epsilon diametral extensometer* (see **Figure 51**) was used to measure the specimen diameter during the tests. The sensor was placed at the middle of the specimens and held in its position by a rubber band (see **Figure 52**). The specimen cross section was positioned between the extensometer's quartz rods of which one is movable. Thus, changes in the specimen diameter during thermomechanical testing lead to displacements of the movable rod resulting in changes of the measuring signal. With this *CGauge* signal, the true strain and stress can be determined as follows.[84]

The true strain ε is defined as

$$\varepsilon = \int_{l_0}^{l} \frac{dl}{l} = \ln \frac{l}{l_0} \qquad [6]$$

where l_0 is the initial length of the specimen and l its actual length. Assuming volume consistency ($l_0\, A_0 = l\, A$), equation [6] can be rewritten as

$$\varepsilon = ln \frac{A_0}{A} = 2\, ln \frac{d_0}{d_0 + \Delta d} \qquad [7]$$

where A_0 and A are the initial and actual specimen cross sections, respectively, and d_0 the initial specimen diameter. The true stress σ can be expressed as a function of the force F and the change in diameter Δd according to

$$\sigma = \frac{F}{A} = \frac{4\, F}{\pi\, (d_0 + \Delta d)^2} \qquad [8]$$

This true stress was controlled using CGauge signal in the physical forging simulation.

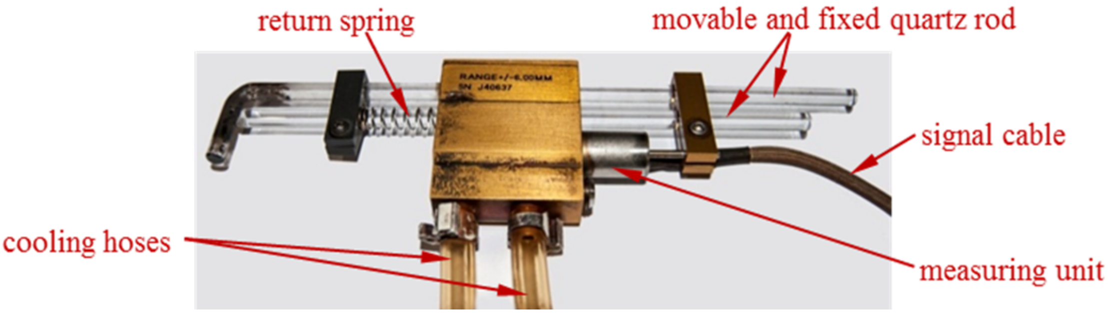

Figure 51. Diametral extensometer used for physical forging simulations (CGauge signal)

Figure 52. Setup of CGauge sensor (left) for strain determination during thermomechanical testing (right)

For calibration measurements (see chapter 4.2.2), however, a different approach was chosen to determine stress and strain. The axial specimen extension was measured with an *Epsilon axial extensometer* (see **Figure 53**). The main components of this sensor are two edged ceramic rods one of which is movable in transverse direction. These knife edges are positioned so that they touch the specimen radially in the middle at a distance of 10 mm. They are held in this position via ceramic fiber cords and tension springs. As the specimen length changes, the distance between the knife edges changes which results in a proportional alteration of the measuring signal.

This *HZT071* signal (corresponding to Δl) was used as mechanical control value during the calibration measurements. The axial extension was kept zero during the thermal cycle and the resulting thermal stresses were determined via the following definition of the engineering stress:

$$\sigma = \frac{F}{A_0} = \frac{4\,F}{\pi\, {d_0}^2} \qquad [9]$$

This approach was used because the Epsilon axial extensometer supplies a more accurate signal at low strains.

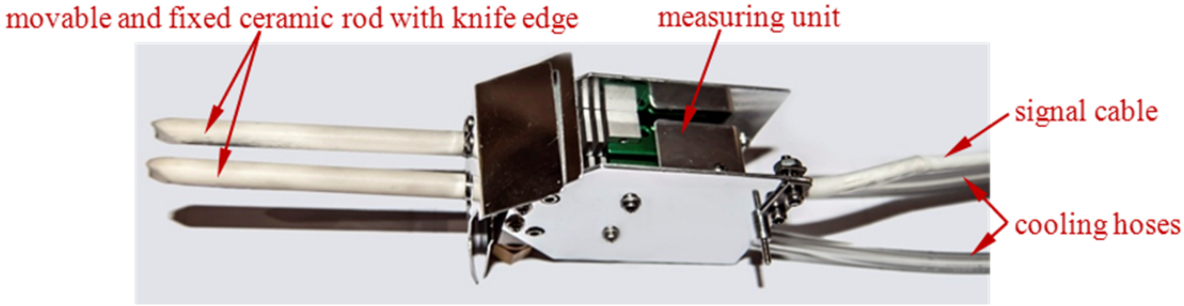

Figure 53. Axial extensometer used for calibration measurements (HZT071 signal)

Both extensometers were air cooled during thermomechanical testing to avoid damage by overheating and measurement errors due to excessive thermal expansion of sensor components.

4.3 Metallography and microscopy

Microstructural investigations using light optical microscopy (LOM) and scanning electron microscopy (SEM) were performed at IWS. Furthermore, high-resolution field emission SEM (FEG-SEM) observations were carried out at Vienna University of Technology.

Metallographic samples were cut with an abrasive cutting machine (*WOCO TOP 350*) using coolant to minimize heat generation. **Figure 54** shows the typical sampling position on a deformed specimen and roughly indicates the specimen regions where detailed metallographic investigations on the base material (i.e. undeformed zone) and the deformed material were performed. Unless specified differently, all micrographs presented in this work were taken in longitudinal specimen direction, i.e. the direction of external load.

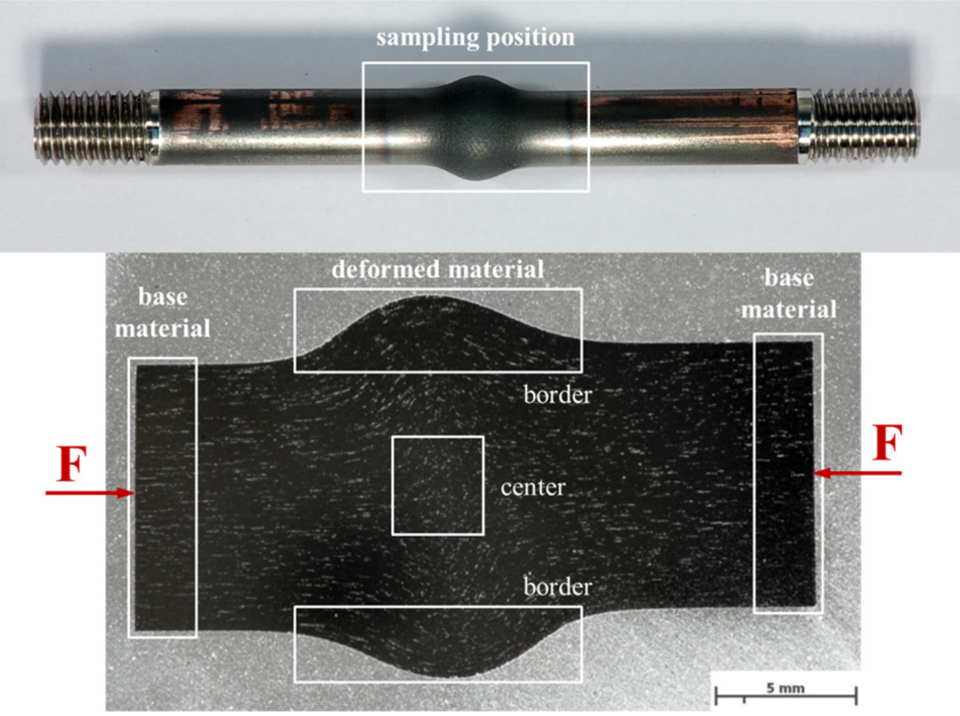

Figure 54. Metallographic sampling position and investigated regions of deformed specimens

Metallographic samples were mounted using a hot mounting press (*Struers CitoPress-20*) and epoxy resin (*Struers DuroFast*) at 250 bar and 180 °C for 4 minutes followed by water cooling for 2.5 minutes. Subsequently, the samples were wet grinded with a grinding/polishing machine (*Struers TegraPol-31*) using 120, 180, 320, 500, 800, 1200 and 2400 grit/inch SiC grinding papers. After that, the samples were polished on the same machine using polishing cloths and a diamond suspension (*Struers DiaDuo-2*) consisting of diamond particles (3µm and 1µm, respectively) and cooling lubricant. SEM and FEG-SEM samples were further polished using oxide polishing suspension (*Struers OP-S*) for up to 20 minutes.

Finally, metallographic etching was performed on LOM and certain SEM samples. Different etching agents and methods were tested and the best results were obtained using the etchants shown in **Table 14**. After each mentioned preparation step, the samples were cleaned with water and ethanol. For SEM and FEG-SEM samples, ultrasonic cleaning in alcohol was performed as last preparation step.

Table 14. Metallographic etchants for the investigated Ni-base alloys

	etchant		etching time at room temperature
Inconel 718	100 ml	hydrochloric acid (HCl)	10-15 s
Allvac 718Plus	+ 4 ml	hydrogen peroxide (H_2O_2)	20-30 s
Haynes 282	60 ml + 20 ml + 2,5 mg	HCl nitric acid (HNO_3) Cupric chloride ($CuCl_2$)	30-40 s

LOM examinations were performed using *Zeiss Axio Observer.Z1m* and *Zeiss Discovery.V20 SteREO* microscopes and the image analysis software *AxioVision*. SEM was carried out on *LEO 1450 VP* (Graz University of Technology) and *FEI Quanta 200 FEGSEM* (Vienna University of Technology) scanning electron microscopes equipped with SE/BSE detectors and EDX systems.

Grain size evaluations were performed using the linear intercept method according to ASTM E112 with the help of a *MATLAB* script.[85, 86] For each evaluation, at least four micrographs of different specimen base material positions at sufficiently low magnifications (50 x - 125 x) were investigated in order to minimize statistical errors. Only regular grain boundaries were used for interceptions, i.e. coherent as well as incoherent twin boundaries were neglected.

Precipitate quantification was performed using FEG-SEM images with magnifications of at least 30 000 x. The mean diameters and phase fractions of the investigated phases were determined by simple image analysis. Selected micrographs were first processed for optimal brightness and contrast in *Adobe Photoshop CS6*. Then, a threshold filter was applied to generate black and white images highlighting the precipitates (see **Figure 55**). Their dimensions were measured in pixel and converted to nm via the corresponding image scale. At least 20 particles were gauged per micrograph and up to three micrographs were evaluated for each alloy. For each processed micrograph, the precipitate phase fraction was determined via

$$f = \frac{A_p}{A_{tot}} \qquad [10]$$

where A_p is the area of all precipitates (black) and A_{tot} the total image area. The final mean diameter and phase fraction was then obtained by averaging the corresponding values of each micrograph.

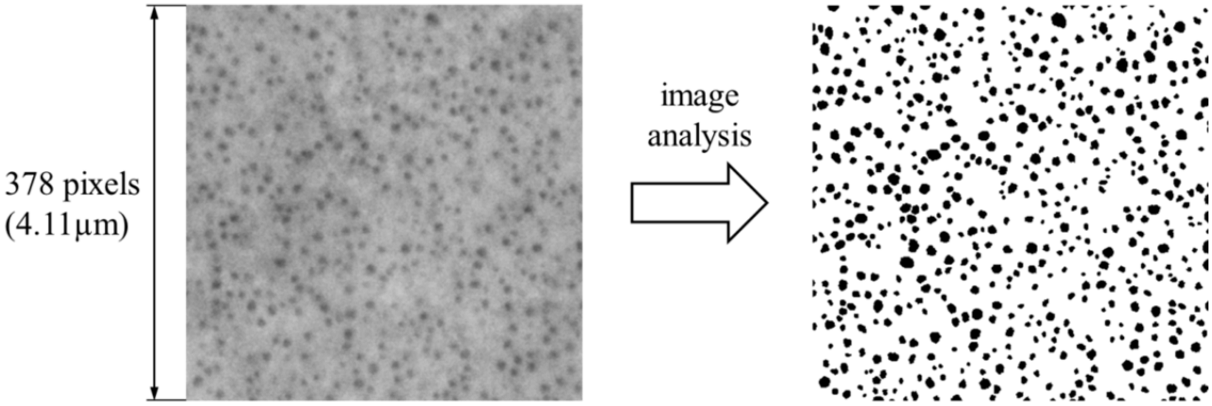

Figure 55. FEG-SEM BSE-image of Allvac 718Plus base material before (left) and after image analysis (right) as used for precipitate quantification

4.4 Numerical simulation

All simulations were performed with Mat*Calc 5.51 (release 1.011)* using the thermodynamic database *mc_ni_v2.000.tdb* and the diffusion database *mc_ni_v2.000.ddb.*[68]

For all calculations, simplified chemical compositions were chosen according to the measured compositions of the received alloys (see **Table 15**).

Table 15. Chemical compositions of the alloys used in MatCalc simulations, wt.%

	Co	Cr	Fe	Mo	W	Al	Ti	Nb	C	B
Inconel 718	0.150	19.320	17.50	2.990	-	0.49	0.950	5.20	0.0220	$37 \cdot 10^{-6}$
Allvac 718Plus	9.160	17.920	9.34	2.695	1.0	1.51	0.750	5.50	0.0220	0.0045
Haynes 282	10.375	19.445	0.79	8.520	-	1.57	2.125	-	0.0615	0.0040

4.4.1 Thermodynamic equilibrium

To obtain information about occurring equilibrium phases and their solvus temperatures, stepped equilibrium calculations were performed in a temperature range between 550 °C and 1400 °C. In these calculations, the chemical composition of the materials as well as expected phases had to be specified (see **Table 16**). These considered phases were mainly chosen according to literature (see chapters 3.2.2 and 3.2.3).

Table 16. Phases considered for equilibrium calculations and their MatCalc designations

	equilibrium phases	
Inconel 718	• liquid (*liquid*) • γ (*fcc_a1*) • γ' (*gamma_prime*) • γ'' (*gamma_dp*) • δ (*delta*) • η (*ni3ti*) • M_2B (*m2b*)	• MX (*fcc_a1#01*) • $M_{23}C_6$ (*m23c6*) • M_6C (*m6c*) • M_7C_3 (*m7c3*) • σ (*sigma*) • μ (*mu_phase*) • Laves (*lav_c15*)
Allvac 718Plus	same as for Inconel 718 but without γ''	
Haynes 282	same as for Inconel 718 but without γ'' and δ	

4.4.2 Precipitation of primary carbides during solidification

In order to determine the composition and phase fraction of primary MC precipitates, Scheil-Gulliver solidification simulations[87] were performed in a temperature range between 1400 °C and 1000 °C according to preliminary analyses by Rindler et al.[88]

In these simulations, the same phases as for the corresponding equilibrium calculations were considered and back-diffusion of C and B was permitted.

4.4.3 Precipitation kinetics during heat treatment and forging

For precipitation kinetics simulations, the respective temperature profiles of each alloy during heat treatment and forging was defined as MatCalc heat treatment. However, different amounts of forging cycles were simulated for each alloy as their experimentally determined minimum strain rates differed (see chapter 5.1).

In MatCalc, deformation was modeled to occur only in the 40 seconds long forging phases at T_{max}. For this reason, twice the absolute value of the experimentally obtained average strain rate (for a maximum stress of -350 MPa) was used during this phase. During the remaining 40 seconds of the forging cycle the strain rate was set zero.

Table 17 summarizes the microstructural parameters used for the γ (*fcc_a1*) matrix phase in heat treatment and forging simulations. Linear functions for the temperature dependency of elastic moduli and Poisson's ratios (in °C) were derived from literature values.[32, 38, 43]

Grain sizes were chosen according to experimental results (see chapter 5.2) while no subgrain sizes were defined.

For all three alloys, the equilibrium dislocation density of the γ matrix was assumed to be 10^{11} m^{-3} and a novel model for dynamic dislocation evolution during deformation was applied. This model takes dislocation creation (A), annihilation of parallel dislocations with opposite Burger's vectors (B) and annihilation by dislocation climb (C) into account via material parameters.[89] The same parameters were used for all three alloys, i.e. A = 50, B = 5 and C = 10^{-3}. Furthermore, excess vacancy formation was considered during deformation at T_{max} and a vacancy diffusion correction factor of 10 was applied.

Table 17. Microstructural parameters of the γ matrix and forging parameters used in MatCalc

	grain size, m	**elastic modulus**, Pa	**Poisson's ratio**	**strain rate**, s^{-1}	**forging cycles**
Inconel 718	$100 \cdot 10^{-6}$	$(206 - 65/830 \cdot T) \cdot 10^{9}$	$0.293 + 0.033/830 \cdot T$	$2.4 \cdot 10^{-4}$	10
Allvac 718Plus	$50 \cdot 10^{-6}$	$(215 - 47/830 \cdot T) \cdot 10^{9}$	$0.308 + 0.032/830 \cdot T$	$5.0 \cdot 10^{-5}$	50
Haynes 282	$150 \cdot 10^{-6}$	$(218 - 57/830 \cdot T) \cdot 10^{9}$	$0.318 + 0.037/830 \cdot T$	$2.2 \cdot 10^{-6}$	500

Different combinations of considered phases were tested for heat treatment and forging simulations according to experimental results, equilibrium calculations and suggestions from literature. **Table 18** shows the precipitation phases chosen for the final calculations and their nucleation sites.

According to experimental results, two possible nucleation sites were defined for δ phase in Inconel 718 and Allvac 718Plus during forging. For that reason, two separate populations of the phase were considered in the calculations. For all three alloys, the predefined MX phase in MatCalc, *fcc_a1#01*, was disabled and replaced by a *MC* phase with predefined constituents according to the composition of primary carbides determined in Scheil-Gulliver simulations (see chapter 5.3.2). This was done to reduce calculation time. Two populations of this MC phase with different nucleation sites were considered for Haynes 282.

For γ'' and δ phases, a shape correction factor of 0.1 was used to take their platelet shape into account. All other phases were assumed to be spherical.

The stated numbers of precipitate size classes for the computations in MatCalc were chosen both to obtain accurate results and to optimize calculation time.

Table 18. Phases considered for precipitation kinetics simulations in MatCalc and their nucleation sites

	precipitate phase	nucleation sites		number of precipitate size classes
		heat treatment	forging	
Inconel 718	γ'/γ''	bulk		30
	δ	grain boundaries	dislocations and grain boundaries	30
	MC	dislocations		10
Allvac 718Plus	same as for Inconel 718 but without γ''			
Haynes 282	γ'	bulk		30
	MC	dislocations and grain boundaries		10
	$M_{23}C_6$	grain boundaries		10
	M_6C	grain boundaries		10

The contribution of coherence stresses via volumetric misfits of γ' and γ'' precipitates during nucleation and deformation was taken into account in the calculations. **Table 19** shows the used misfit values of the regarding phases in each alloy taken from literature.[78, 90, 91]

Furthermore, interfacial energy correction of γ', γ'' and δ phases was accomplished via temperature dependent correction factors. For Inconel 718 and Haynes 282, these factors were adapted from those used by Radis et al. for Allvac 718Plus[75] (see **Table 19**). This was done to consider the differing solution temperatures of the regarding phases in each alloy as determined from equilibrium calculations (see chapters 5.3.1).

Table 19. Volumetric misfit and suggested interfacial energy correction factors of precipitate phases in MatCalc

	phases	volumetric misfit	interface energy correction factors
Inconel 718	γ''	0.021[91]	1.00 at 20 °C 0.95 at 800 °C 0.60 at 900 °C
	γ'	0.004[91]	
	δ	-	
Allvac 718Plus	γ'	-0.003[78]	1.00 at 20 °C[7] 0.95 at 850 °C 0.60 at 975 °C
	δ	-	
Haynes 282	γ'	0.002 at 590 °C[90] 0.000 at 725 °C -0.002 at 880 °C	1.00 at 20 °C 0.95 at 900 °C 0.60 at 1040 °C

5 Results

5.1 Thermomechanical testing

5.1.1 Specimen temperature distribution

Figure 56 shows the results of temperature measurements at different specimen positions for Inconel 718 and Haynes 282 specimens. The temperature distribution along the specimen is symmetric, small deviations can be explained with inaccurate thermal element welding positions.

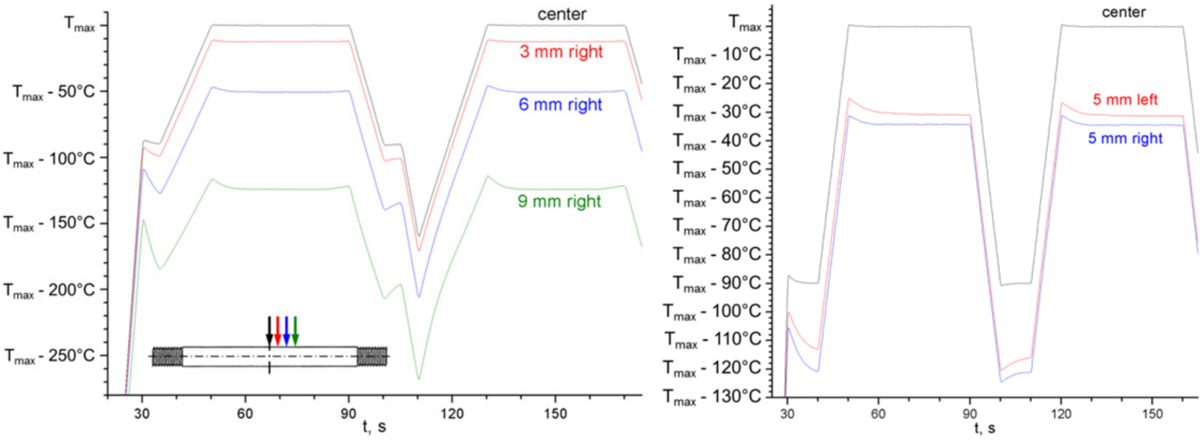

Figure 56. Temperature distribution in Haynes 282 (left) and Inconel 718 specimens (right)

5.1.2 Calibration measurements

The result of Inconel 718 calibration measurement is shown in **Figure 57** (left). The indicated maximum thermal compressive and tensile stresses were considered as input parameters for its forging simulation.

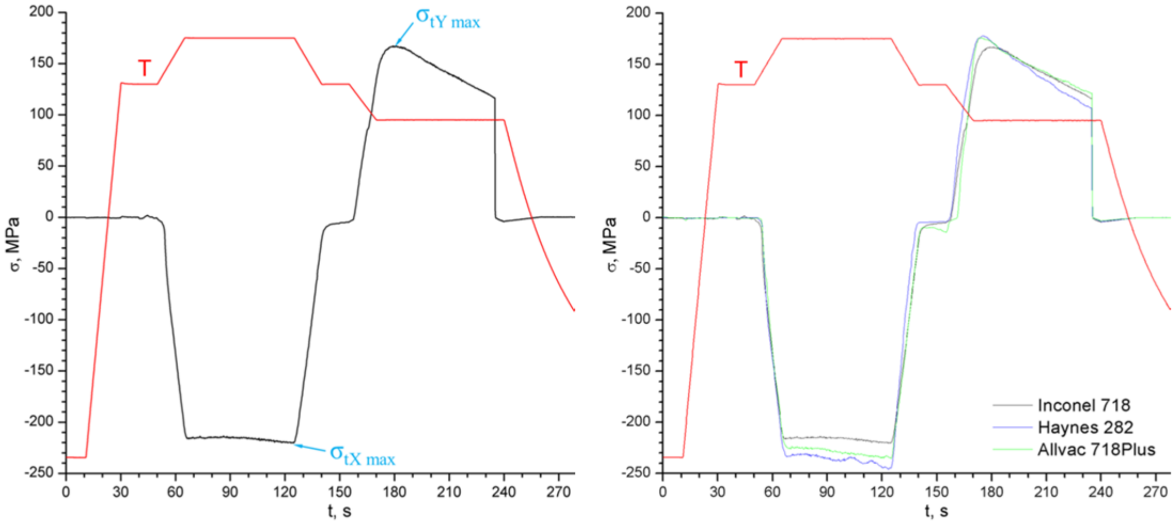

Figure 57. Stress and temperature signals of Inconel 718 calibration measurement (left) and comparison of the resulting thermal stresses (right)

To validate both the calibration measurement and the stress values calculated for the other alloys, calibration tests were also performed with them. **Table 20** shows the calculated and measured thermal stresses of all three investigated materials. The values were calculated according to equation [4] (see chapter 4.2.1) using the alloys' respective elastic moduli and CTE at T_{die}.

Deviations between calculated and measured values are rather small and their variation between the alloys was considered negligible especially as the stress curves showed good agreement (see **Figure 57**, right). For these reasons, it was considered appropriate to choose the same thermal stresses for the physical forging simulations of all three alloys (σ_{tX} = -220 MPa/σ_{tY} = 170 MPa).

Table 20. Calculated and measured thermal stresses during and after forging for the three investigated materials

	Inconel 718		Allvac 718Plus		Haynes 282	
	σ_{tX}, MPa	σ_{tY}, MPa	σ_{tX}, MPa	σ_{tY}, MPa	σ_{tX}, MPa	σ_{tY}, MPa
calculated	-233.3	181.4	-234.1	182.1	-223.4	173.7
measured	-220.3	167.3	-235.3	176.2	-246.2	178.4
deviation	5,6%	7.8%	-0.5%	3.2%	-10.2%	-2,7%

5.1.3 Physical forging simulation

5.1.3.1 Inconel 718

Figure 58 shows stress, temperature and strain signals of Inconel 718 physical forging simulations carried out at a maximum stress of -450 MPa (specimens 1-3). After heating-up to T_{die} for the first time, the specimen strain was zeroed in order to obtain only the plastic share ε_{pl}. At the end of each strain curve the number of the according specimen is denoted. It is apparent that all three specimens experienced severe plastic strain already after two cycles. Specimens 1 and 3 were used for performed pre- and calibration tests before the physical forging simulation. Their higher strain rates compared to specimen 2 could be explained by micro-structural changes during these tests.

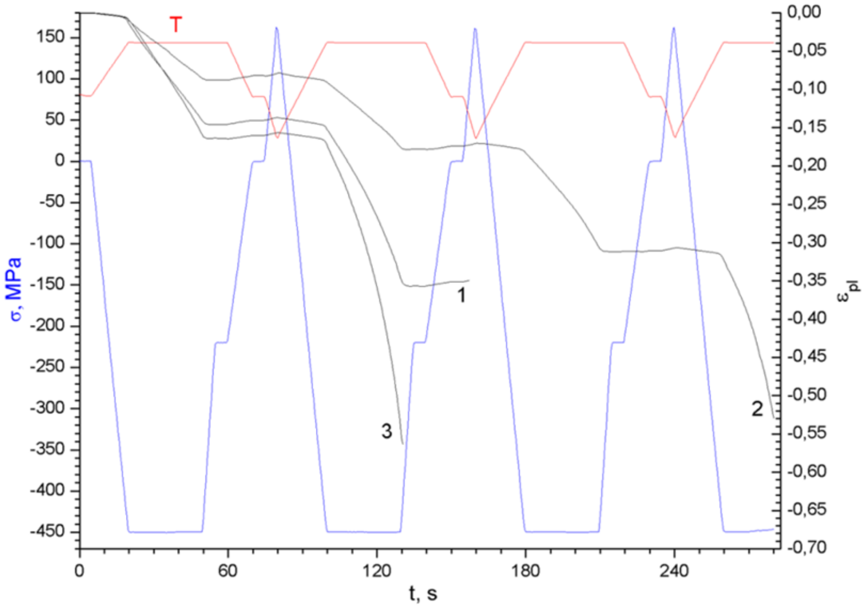

Figure 58. Results of Inconel 718 physical forging simulations (maximum stress -450 MPa)

Figure 59 shows the progression of plastic strain during physical forging simulations carried out at -350 and -300 MPa maximum stress, respectively (specimens 4-13). Contrary to **Figure 58**, the time axis is scaled in forging cycles. As expected, the material performance increased with decreasing stress. Generally, the results show good agreement. Specimens 7 and 9, however, exhibited considerably divergent minimum strain rates compared to the other specimens tested at the same maximum stress level.

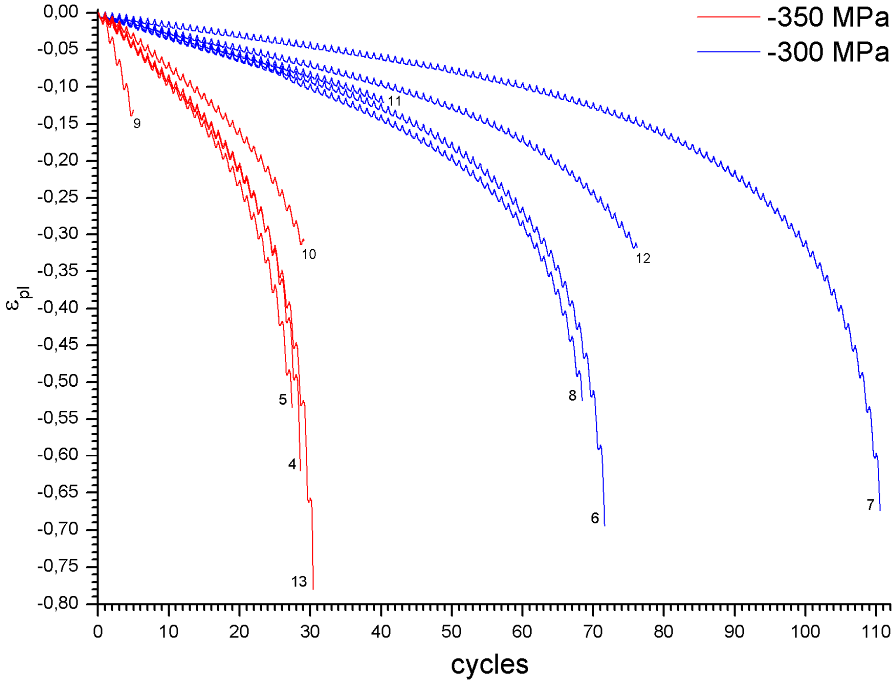

Figure 59. Results of Inconel 718 physical forging simulations (maximum stresses -350 and -300 MPa)

The curves can be roughly divided into two stages. Plastic strain increases linearly to a certain value (between around 0.07 and 0.15) from where on its increase is progressive (see **Figure 60**). The minimum strain rate for each specimen was estimated by evaluating the slope of the linear first stage of the strain curves according to

$$\dot{\varepsilon}_{min} = \frac{\Delta\varepsilon}{\Delta t} = \frac{\varepsilon_{pl\,1}}{t_1} \qquad [11]$$

where $\varepsilon_{pl\,1}$ and t_1 are plastic strain and time, respectively, at the end of the linear sections.

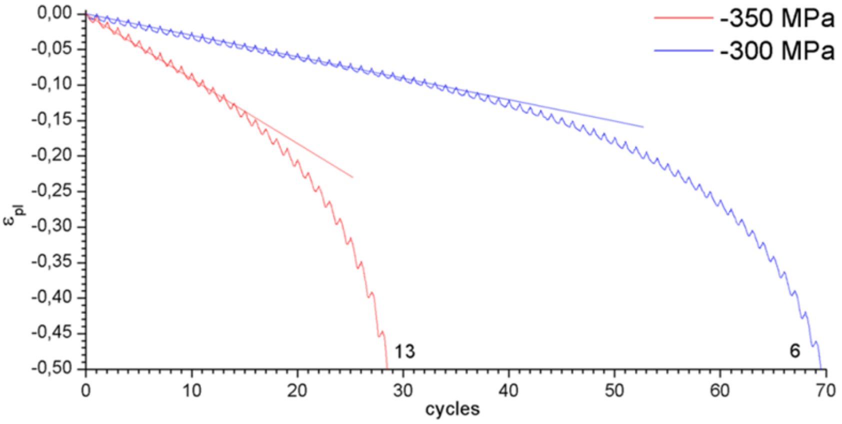

Figure 60. Inconel 718 strain rate curves showing linear and progressive stages

Table 21 summarizes the results of the physical forging simulations for Inconel 718. For each specimen, the plastic strain ε_{pl}, the number of forging cycles and the calculate minimum strain rate $\dot{\varepsilon}_{min}$ are denoted.

Table 21. Result overview of Inconel 718 physical forging simulations

specimen no.	σ_{max}, MPa	ε_{pl}	**cycles**	$\dot{\varepsilon}_{min}$, s^{-1}	**comments**
0	-	-	-	-	used for pre-tests with two additional thermocouples (-5 and 5 mm from specimen center)
1	-450	-0.35	2.0	$-2.1 \cdot 10^{-3}$	previously used for pre- and calibration tests
2	-450	-0.53	3.5	$-1.3 \cdot 10^{-3}$	-
3	-450	-0.56	1.6	$-2.5 \cdot 10^{-3}$	previously used for calibration tests
4	-350	-0.62	28.6	$-1.2 \cdot 10^{-4}$	-
5	-350	-0.53	27.4	$-1.3 \cdot 10^{-4}$	-
6	-300	-0.69	71.6	$-3.7 \cdot 10^{-5}$	-
7	-300	-0.67	110.5	$-1.8 \cdot 10^{-5}$	-
8	-300	-0.53	68.4	$-3.9 \cdot 10^{-5}$	-
9	-350	-0.13	5.0	$-2.9 \cdot 10^{-4}$	-
10	-350	-0.31	29.1	$-1.1 \cdot 10^{-4}$	-
11	-300	-0.12	40.4	$-3.5 \cdot 10^{-5}$	-
12	-300	-0.32	76.2	$-3.0 \cdot 10^{-5}$	-
13	-350	-1.17	32.7	$-1.1 \cdot 10^{-4}$	CGauge sensor slipped off at ε_{pl} = -0.8 → ε_{pl} calculated from equation [7] after test

5.1.3.2 Allvac 718Plus

Figure 61 shows the strain curves resulting from physical forging simulations with Allvac 718Plus specimens. The strain curves were smoothed and the time axis is displayed logarithmically for a better visual representation. Except for specimen 4, the results show excellent agreement for all maximum stress levels.

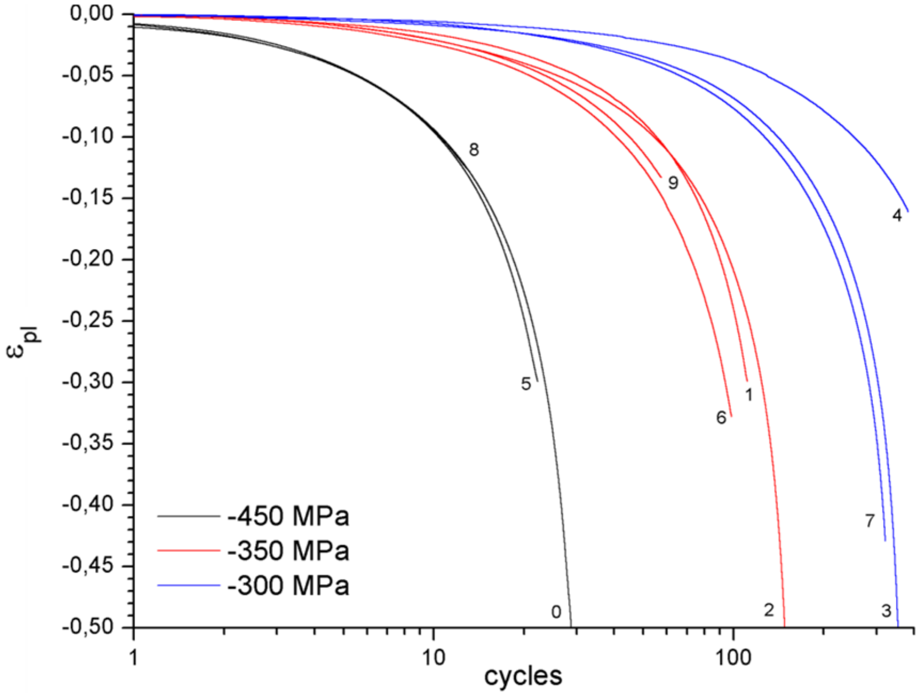

Figure 61. Results of Allvac 718Plus physical forging simulations

Similar to Inconel 718, many curves show linear behavior in the low strain region. Especially at lower maximum stresses, however, some specimens exhibited an initial degressive increase in strain. Therefore, these curves can be roughly divided in three stages (see **Figure 62**). The minimum strain rate was evaluated from the second, linear section of such curves.

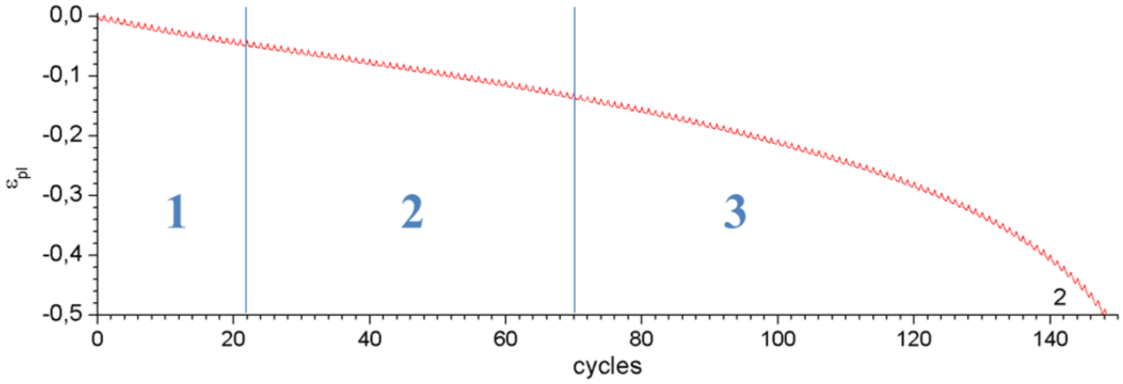

Figure 62. Allvac 718Plus strain rate curve showing three stages

Table 22 summarizes the results of the physical forging simulations for Allvac 718Plus.

Table 22. Result overview of Allvac 718Plus physical forging simulations

specimen no.	σ_{max}, MPa	ε_{pl}	**cycles**	$\dot{\varepsilon}_{min}$, s^{-1}	**comments**
0	-450	-0.53	28.6	$-1.2 \cdot 10^{-4}$	previously used for calibration tests
1	-350	-0.31	111.6	$-2.2 \cdot 10^{-5}$	specimen fractured because machine cooling failed during test
2	-350	-0.52	149.5	$-2.2 \cdot 10^{-5}$	CGauge sensor placed slightly off-center → ε_{pl} calculated from equation [7] after test
3	-300	-0.50	352.7	$-8.1 \cdot 10^{-6}$	-
4	-300	-0.17	382.7	$-5.1 \cdot 10^{-6}$	-
5	-450	-0.31	22.4	$-1.2 \cdot 10^{-4}$	-
6	-350	-0.33	98.7	$-3.1 \cdot 10^{-5}$	-
7	-300	-0.43	320.3	$-9.4 \cdot 10^{-6}$	-
8	-450	-0.13	13.2	$-1.2 \cdot 10^{-4}$	-
9	-350	-0.14	58.3	$-2.8 \cdot 10^{-5}$	-

5.1.3.3 Haynes 282

Figure 63 shows smoothed strain curves resulting from Haynes 282 physical forging simulations. The results show good agreement for all stress levels. Specimen 0, however, showed considerably better performance compared to the other specimens tested at a maximum stress of -450 MPa. This could be due to microstructural changes (such as an increase in dislocation density or the formation of new strengthening precipitates) during previously performed calibration tests.

Figure 64 (left) shows two representative strain curves of -450 MPa and -350 MPa tests, respectively. In contrast to Inconel 718 and Allvac 718Plus, these curves do not exhibit a linear first stage. Minimum strain rates were therefore simply determined from their slope at $\varepsilon_{pl} = 0$. At lower maximum stress, some curves show slightly different behavior. Similar to Allvac 718Plus, they show a degressive first stage (see **Figure 64**, right) followed either by a short linear section or directly by the progressive section observed in all curves.

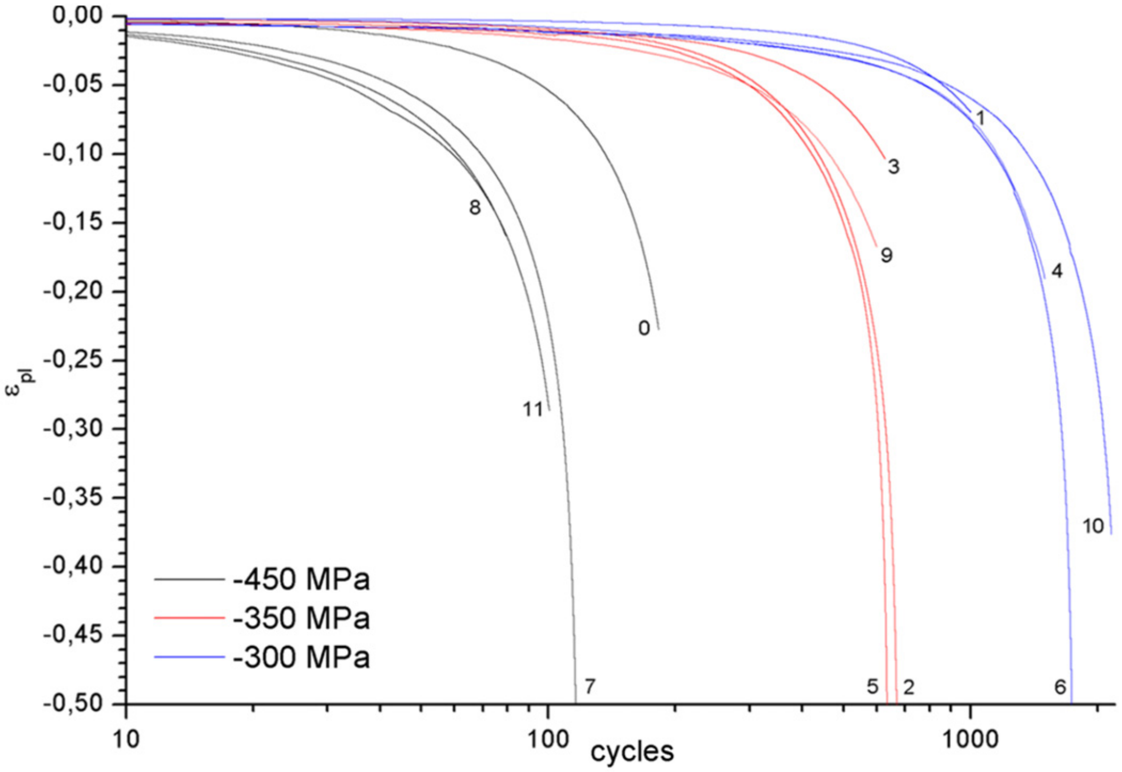

Figure 63. Results of Haynes 282 physical forging simulations

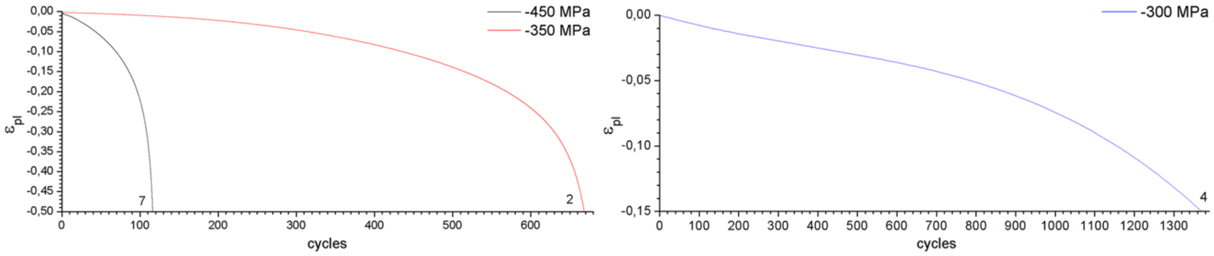

Figure 64. Haynes 282 strain rate curves showing different shapes at high (left) and low stresses (right)

Table 23 summarizes the results of the physical forging simulations for Haynes 282.

Table 23. Result overview of Haynes 282 physical forging simulations

specimen no.	σ_{max}, MPa	ε_{pl}	cycles	$\dot{\varepsilon}_{min}$, s^{-1}	comments
0	-450	-0.23	182.8	$-9.5 \cdot 10^{-6}$	previously used for calibration tests
1	-300	-0.07	1002.3	$-3.5 \cdot 10^{-7}$	-
2	-350	-0.56	672.2	$-8.7 \cdot 10^{-7}$	CGauge sensor placed slightly off-center → ε_{pl} calculated from equation [7] after test
3	-350	-0.10	628.7	$-6.9 \cdot 10^{-7}$	-
4	-300	-0.19	1501.5	$-6.4 \cdot 10^{-7}$	long test (33 h) → stopped and resumed (curves merged), tested with three additional thermocouples (3, 6 and 9 mm from specimen center)
5	-350	-0.56	635.3	$-8.\ 9 \cdot 10^{-7}$	CGauge sensor slipped off because rubber band ripped after 104 cycles → curve offset corrected
6	-300	-0.83	1764.8	$-5.2 \cdot 10^{-7}$	test continued for 736 more cycles after reaching stroke end stop → specimen fractured
7	-450	-0.61	117.4	$-9.8 \cdot 10^{-6}$	-
8	-450	-0.17	80.3	$-1.3 \cdot 10^{-5}$	-
9	-350	-0.17	600.3	$-1.6 \cdot 10^{-6}$	-
10	-300	-0.38	2155.8	$-5.5 \cdot 10^{-7}$	long test (48 h) → stopped and resumed twice (curves merged)
11	-450	-0.29	100.7	$-1.8 \cdot 10^{-5}$	-

5.1.3.4 Hot deformation mechanism

In order to identify the alloys' deformation mechanisms during the physical forging simulations, their stress exponents were assessed from obtained Gleeble data. Therefore, the simplifying assumption was made that the tests were carried out at constant temperature (T_{max}) and constant stress (σ_{max}).

Table 24 summarizes the average minimum strain rates of each alloy. Inconel 718 exhibited the highest strain rates at all stress levels. The values are roughly one order of magnitude higher compared to Allvac 718Plus and two orders of magnitude higher compared to Haynes 282.

Figure 65 shows a graphical representation of the results including linear fit. In this double-logarithmic display, the strain rate vs. stress dependence shows linear behavior in good approximation as indicated by high coefficients of determination (R^2). Therefore, the strain rates could be expressed by a simplified formulation of the constitutive equation [1] (see chapter 3.4.1) as the temperature profile was the same in all tests:

$$\dot{\varepsilon} = K\,\sigma^n \;\leftrightarrow\; \log\dot{\varepsilon} = \log K + n\log\sigma \qquad [12]$$

Evidently, the slope of this linear equation corresponds to the stress exponent n. The resulting stress exponent values, denoted in **Figure 65**, suggest that different deformation mechanisms occurred for each alloy. Their large values, however, indicate possible dislocation pinning by precipitates which seems reasonable for the present γ'/γ" hardened alloys.

Table 24. Minimum strain rates of the alloys during physical forging simulations

		$\dot{\varepsilon}_{min}$, s^{-1}		
		Inconel 718	**Allvac 718Plus**	**Haynes 282**
σ_{max}, MPa	**-450**	$(-2.0 \pm 0.6) \cdot 10^{-3}$	$(-1.2 \pm 0.3) \cdot 10^{-4}$	$(-1.3 \pm 0.4) \cdot 10^{-5}$
	-350	$(-1.2 \pm 0.1) \cdot 10^{-4}$	$(-2.5 \pm 0.4) \cdot 10^{-5}$	$(-1.1 \pm 0.5) \cdot 10^{-6}$
	-300	$(-3.2 \pm 0.7) \cdot 10^{-5}$	$(-7.5 \pm 1.8) \cdot 10^{-6}$	$(-5.2 \pm 1.0) \cdot 10^{-7}$

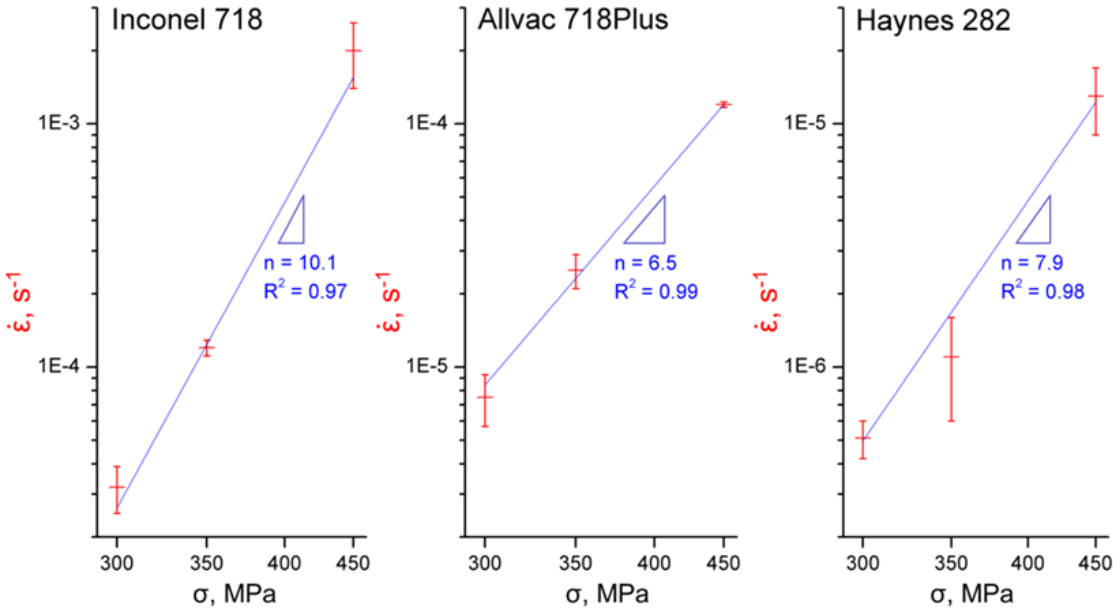

Figure 65. Stress dependence of minimum strain rates during physical forging simulations

5.2 Metallography and microscopy

5.2.1 Inconel 718

5.2.1.1 Base material

As mentioned in chapter 4.1.1.2, the microstructure of Inconel 718 billet after solution annealing was inhomogeneous across its cross section concerning grain size and the distribution of large particles (see **Figure 66**). Therefore, depending on their sampling position, the grain size of tensile samples differed quite strongly.

However, the grain structure was similar in transverse and longitudinal direction in the undeformed material. **Table 25** shows the average grain size of certain specimens in longitudinal direction.

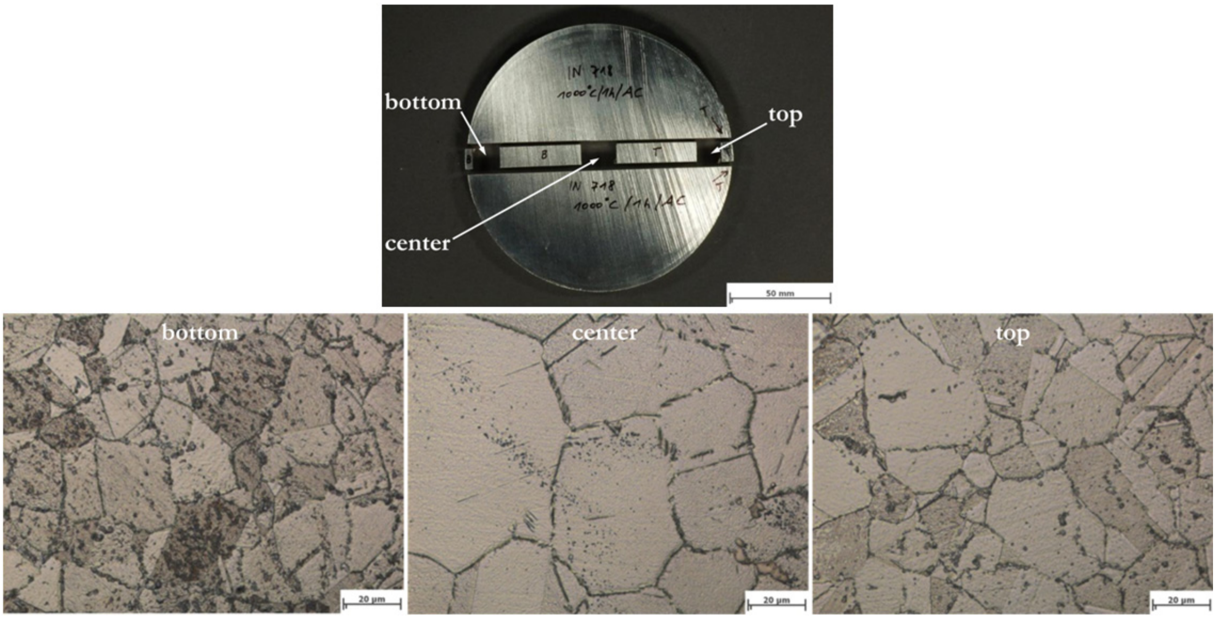

Figure 66. Metallographic sample positions and corresponding micrographs of solution annealed Inconel 718 in transverse billet direction

Table 25. Grain size of Inconel 718 specimens in the undeformed zone

specimen	**grain size**, µm
2	85 ± 40
4	140 ± 85
5	120 ± 60
6	70 ± 40
7	90 ± 55
9	75 ± 45
10	100 ± 50
12	95 ± 60
13	60 ± 40

Figure 67 to **Figure 69** show different micrographs of Inconel 718 base material. In **Figure 67**, band-shaped structures of particles in longitudinal specimen (and therefore billet) direction are observable. These structures of rather large (> 1 µm), randomly shaped particles were found in all

specimens and are assumed to result from the hot forming process of the billet. The particles show light grey appearance in LOM. Furthermore, even larger, randomly distributed and often rhombically shaped orange precipitates were observed (see **Figure 67**).

Figure 68 shows SEM micrographs in which these particles are observable. EDX line-scans and mappings were performed in order to identify their chemical composition. The particles forming band-shaped structures show light appearance in SEM BSE-images (see **Figure 68**, left). They are rich in Nb and also contain smaller amounts of Ti. The larger, rhombically shaped precipitates, on the other hand, appear dark and contain much Ti and only little Nb. This leads to the suggestion that these particles are primary NbC and Ti(C,N) precipitates, respectively.

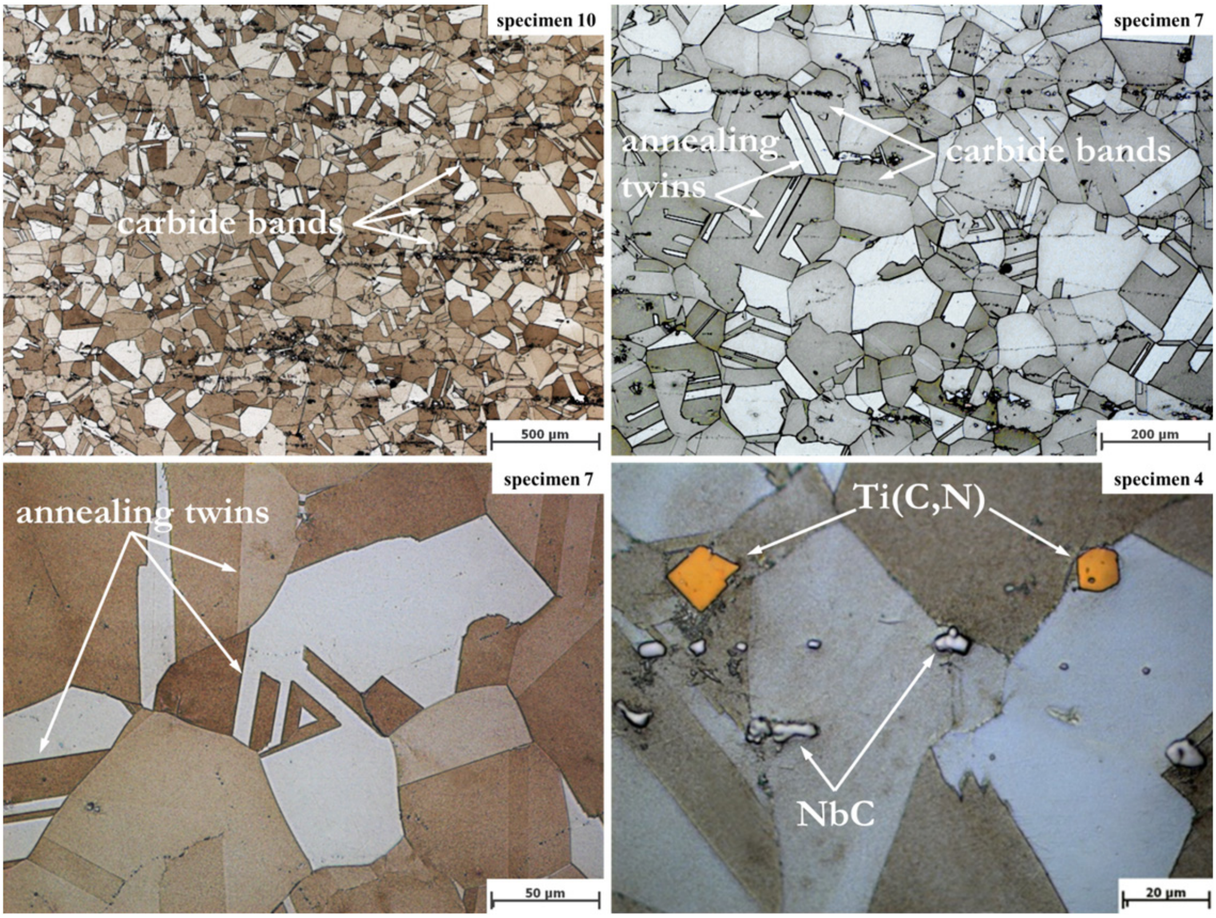

Figure 67. LOM micrographs of Inconel 718 base material showing annealing twins and large primary carbides

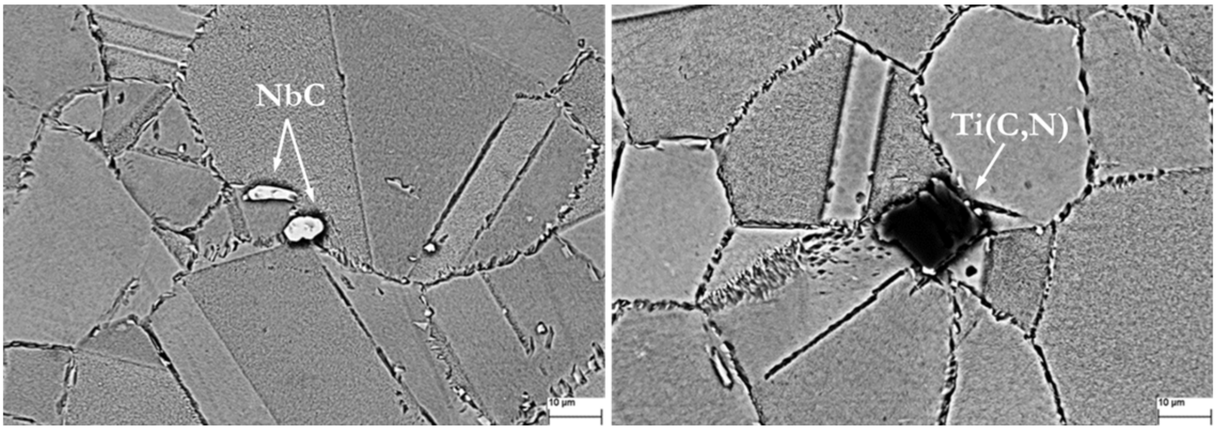

Figure 68. SEM BSE-images of etched Inconel 718 base material showing carbides and grain boundary precipitates

Furthermore, grain boundary particles were observed (see **Figure 68**) but they were too small for EDX characterization. However, the plate-like shape and light appearance of these particles suggests that they are δ phase (Ni_3Nb). Twin boundaries appear to be almost free of such precipitates.

Figure 69 shows high resolution images of Inconel 718 base material revealing light, elongated particles at grain boundaries and inside grains. Due to their small size, no EDX characterization of these precipitates was possible. However, it is assumed that they are δ and γ'' phases, respectively. The disk-shaped precipitates inside grains exhibit a volume fraction of 14% and a characteristic size of 70 ± 15 nm which was determined by averaging the measured particle thickness and diameter as suggested by Dumont et al.[92] The phase fraction is in excellent agreement with values typically stated for γ'' phase[29, 91] and the aspect ratio of the particles (i.e. the ratio of particle thickness to diameter) of 0.35 ± 0.1 is in good agreement with values obtained for γ'' precipitates by Devaux et al.[93]

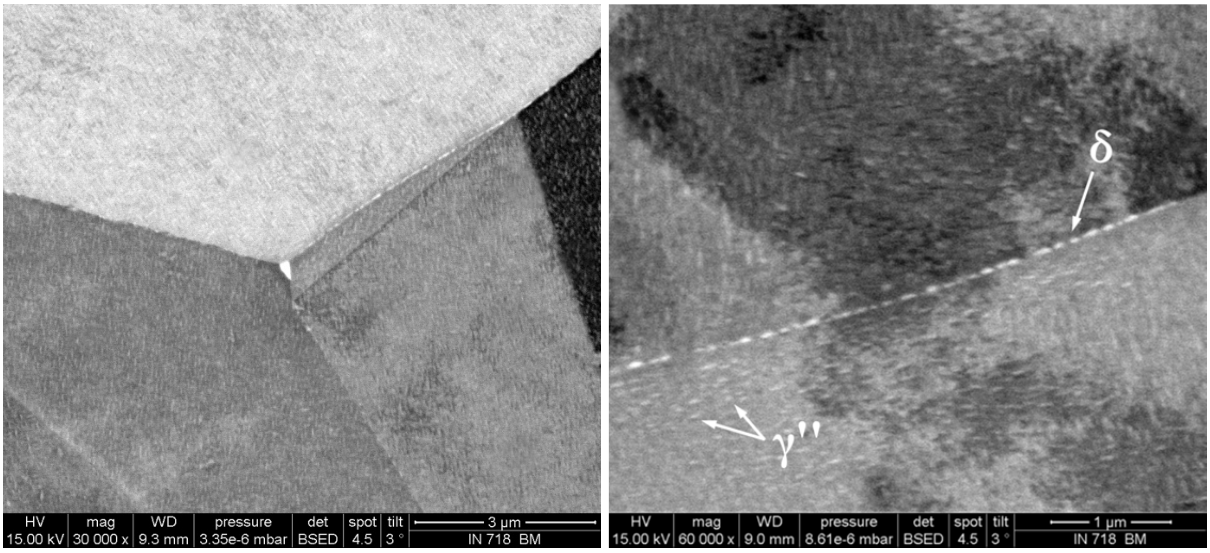

Figure 69. FEG-SEM BSE-images of Inconel 718 base material showing different precipitates at grain boundaries and inside grains

5.2.1.2 Deformed material

Figure 70 shows stereo-micrographs of deformed specimens after physical forging simulations. The deformed carbide band structure revealed in the left image gives indication of the material flow during deformation. From this pattern and the bulged shape of the deformed specimen it is evident that different states of stress occurred in the deformation zone and that uniaxial compression/tension predominated only in the specimen center.

The right image shows the grain morphology of deformed microstructure. Both specimens deformed slightly unsymmetrically which could be either explained by experimental errors (such as unsymmetrical positioning of the thermocouple or deformation of certain parts of the clamping system) or by crystallographic texture.

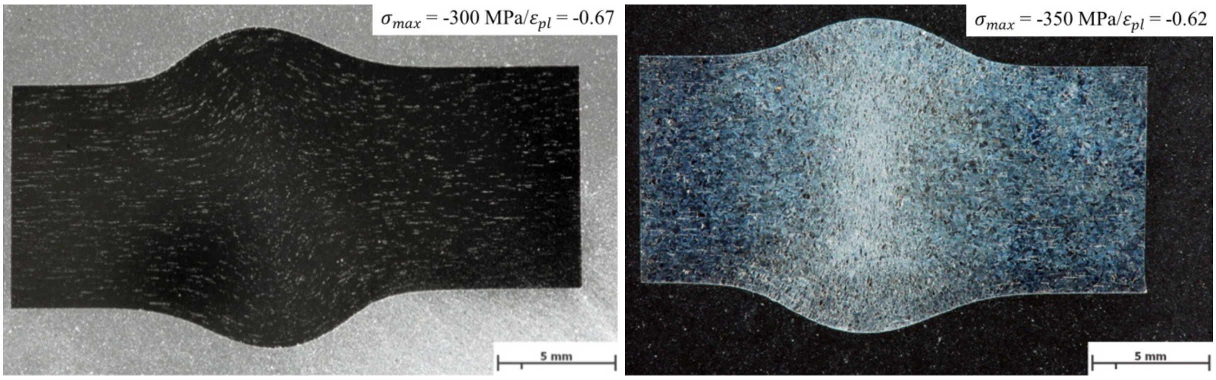

Figure 70. Stereo-micrographs of polished Inconel 718 specimen 7 (left) and etched specimen 4 (right) after deformation

Figure 71 shows LOM micrographs of severely deformed microstructure in the specimen center with grains elongated orthogonally to the direction of external load.

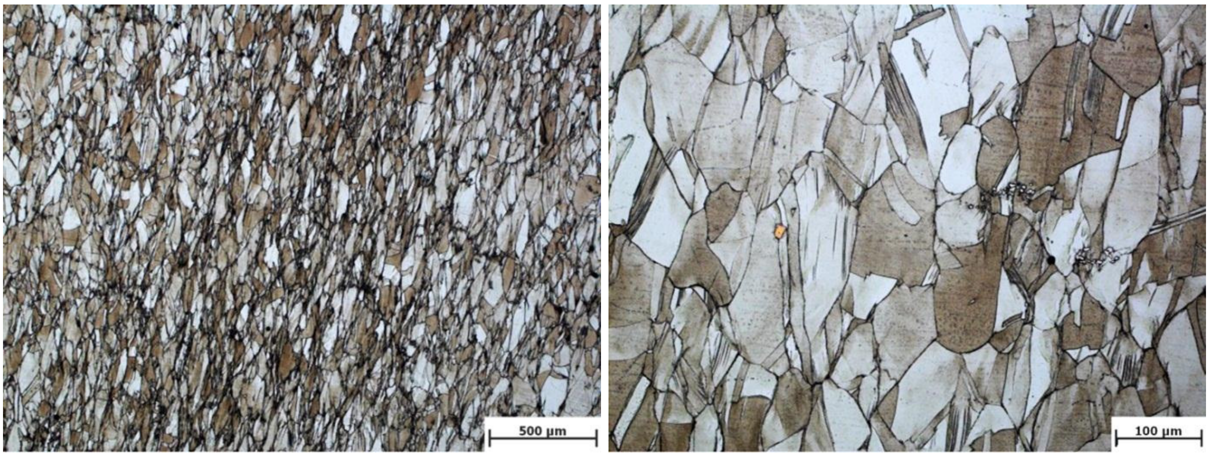

Figure 71. LOM micrographs of deformed Inconel 718 microstructure in the specimen center showing deformed grains (specimen 5, σ_{max} = -350 MPa/ε_{pl} = -0.53)

Figure 72 shows the deformed microstructure of different specimens near their border. Deformation bands as well as pores and, apparently, incipient intergranular cracking are observable. Few small pores were also found in the specimen center, either in the vicinity of carbides or at grain boundaries (see **Figure 73**).

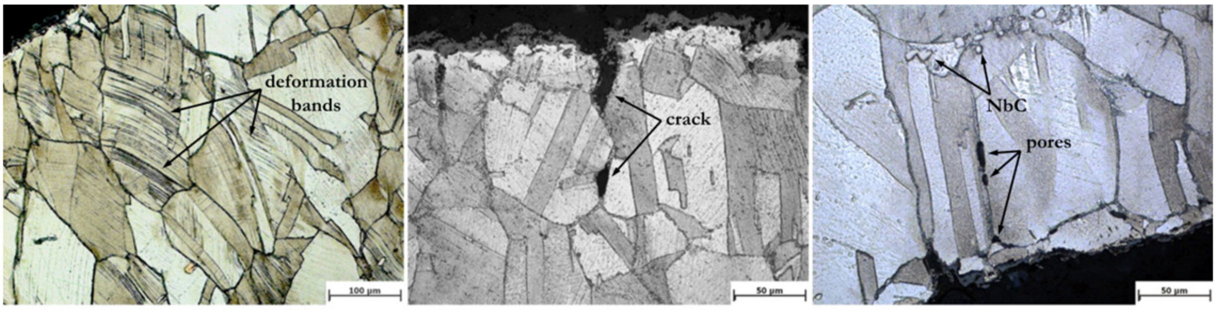

specimen 7, σ_{max} = -300 MPa/ε_{pl} = -0.67 specimen 6, σ_{max} = -300 MPa/ε_{pl} = -0.69 specimen 4, σ_{max} = -350 MPa/ε_{pl} = -0.62

Figure 72. LOM micrographs of deformed Inconel 718 microstructure at the specimen border showing deformation bands, pores and cracks

Figure 74 shows FEG-SEM micrographs of deformed microstructure near the specimen border. Microstructural features such as precipitates inside grains and along grain boundaries as well as deformation bands are observable. These deformation bands form during plastic deformation and represent subdivided parts of the grain with different crystallographic orientation (see chapter 3.3).

Furthermore, light/dark patterns are observed inside grains which are assumed to result from energy stored in the microstructure due to the generation of dislocations during plastic deformation. From these patterns, an inhomogeneity of stored energy is evident, i.e. plastic deformation did not occur homogeneously inside the grains. This can also be observed from local changes in the alignment of small precipitates inside grains (see **Figure 74**, right).

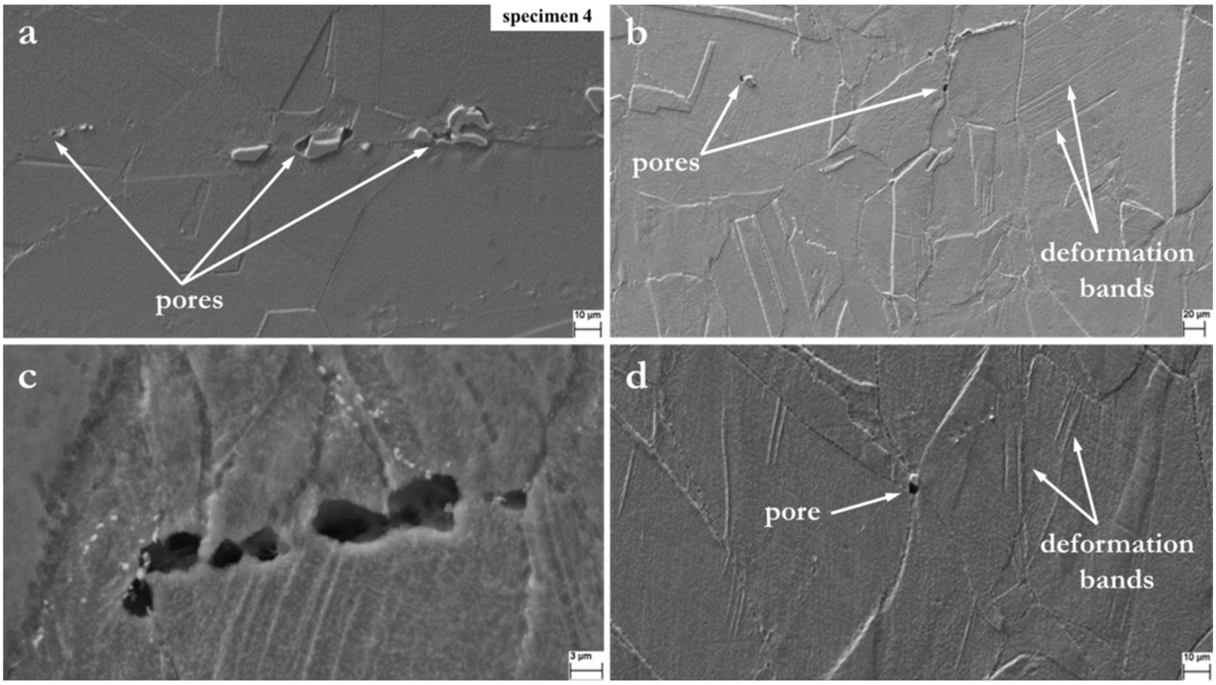

Figure 73. SEM SE-images of undeformed (a) and deformed Inconel 718 microstructure (b-d) showing pores at grain boundaries and particles (specimen 4, σ_{max} = -350 MPa/ε_{pl} = -0.62)

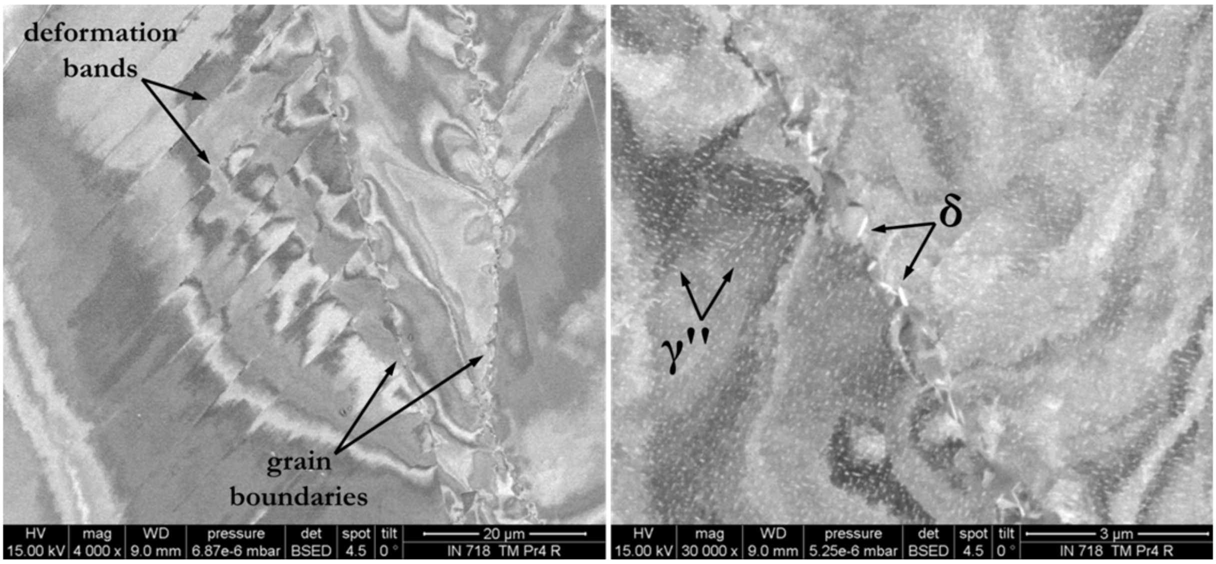

Figure 74. FEG-SEM BSE-image of deformed Inconel 718 microstructure at the specimen border showing deformation bands and different precipitates (specimen 4)

Figure 75 shows FEG-SEM images of deformed microstructure in the specimen center. At all three investigated positions, coarse elongated particles and small (< 1 µm) grains are found at prior grain boundaries and carbides suggesting that DRX occurred. Some of these new grains show annealing twins but they do not contain strengthening γ'' precipitates.

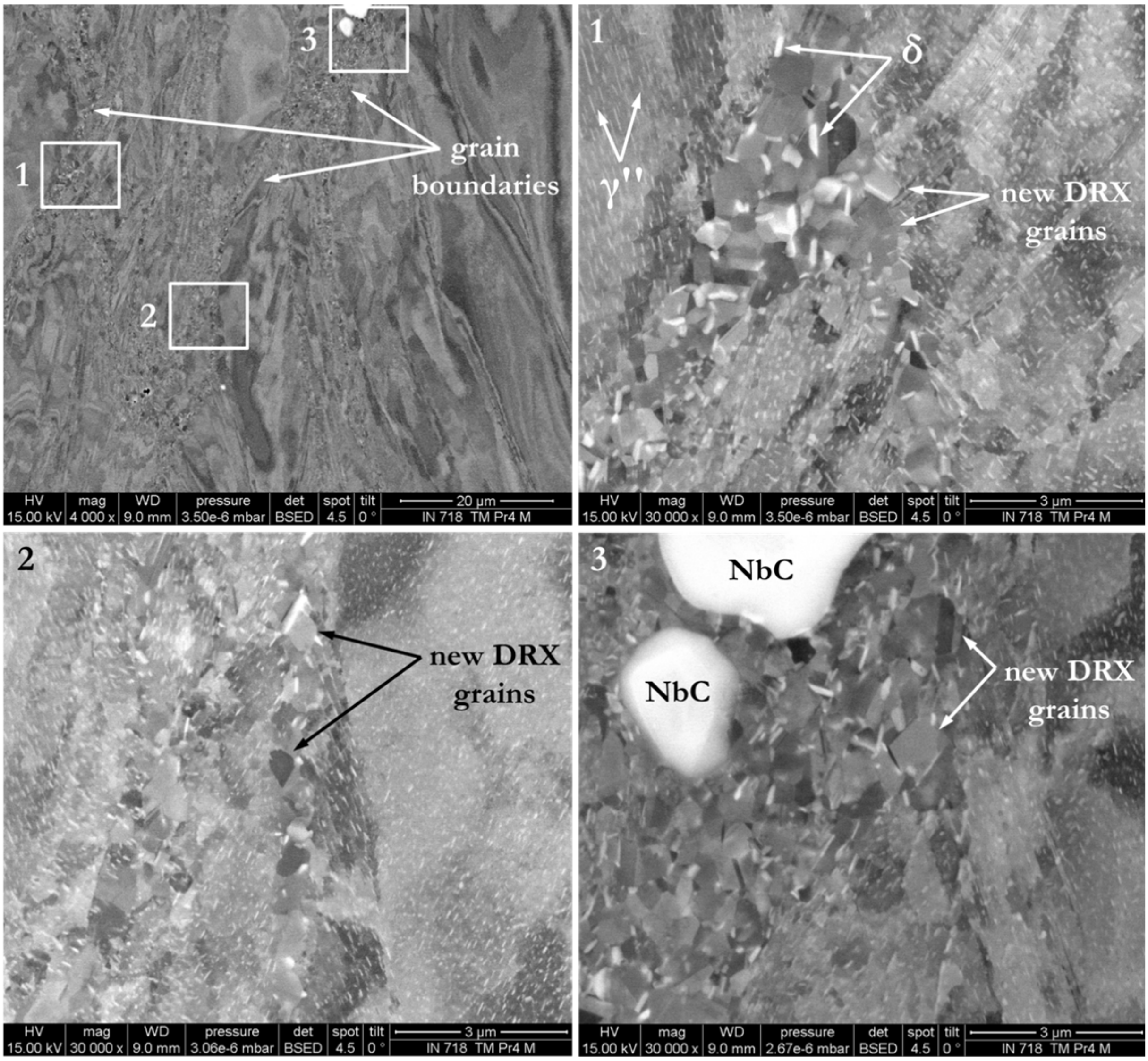

Figure 75. FEG-SEM BSE-images of deformed Inconel 718 microstructure in the specimen center showing different precipitates and recrystallized grains at grain boundaries (specimen 4)

Figure 76 shows a high-resolution micrograph revealing the morphology and alignment of small precipitates (light, elongated γ'' and possibly dark, spherical γ') inside a grain. Local changes in the alignment of the particles are evident. Furthermore, slight coarsening or possibly partial transformation to δ phase can be observed.

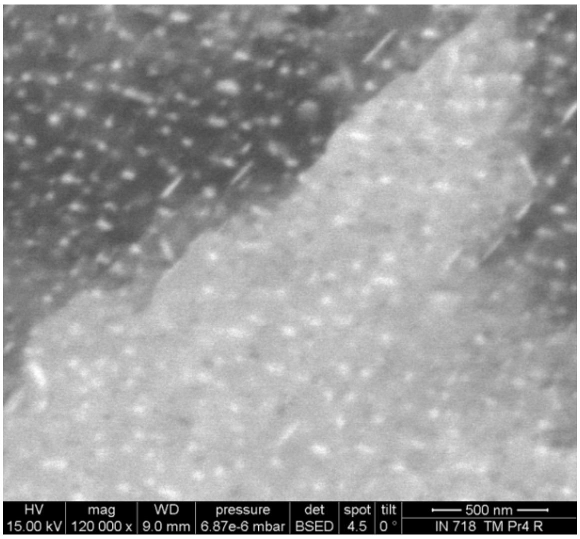

Figure 76. FEG-SEM BSE-image of deformed Inconel 718 microstructure in the specimen center showing small precipitates (specimen 4)

5.2.2 Allvac 718Plus

5.2.2.1 Base material

Figure 77 shows micrographs of undeformed Allvac 718Plus in longitudinal specimen (i.e. in transverse billet) direction. Again, grain size and morphology do not differ strongly in orthogonal direction (see **Figure 78**) and large primary carbides/carbonitrides were found mostly inside grains. It is assumed that they are of NbC and Ti(C,N) type as in Inconel 718. Similar to Inconel 718, ordered structures of these particles were observable. However, these bands occurred to a lower extent in Allvac 718Plus and, due to the sampling position of the tensile specimens, in transverse specimen direction (see **Figure 78**, left). Furthermore, the microstructure shows smaller grain size and more grain-boundary precipitates (see also **Figure 79**). The grain size slightly varied over the specimen length which is also attributable to the sampling direction perpendicular to the billet axis. However, all investigated specimens showed similar grain size with generally lower variation than Inconel 718 (see **Table 26**).

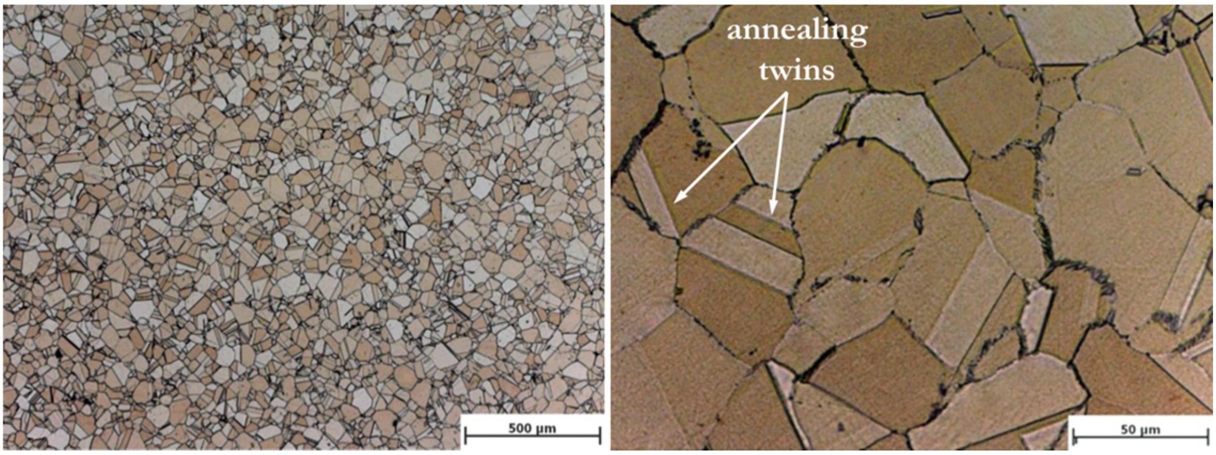

Figure 77. LOM micrographs of Allvac 718Plus base material showing annealing twins (specimen 2)

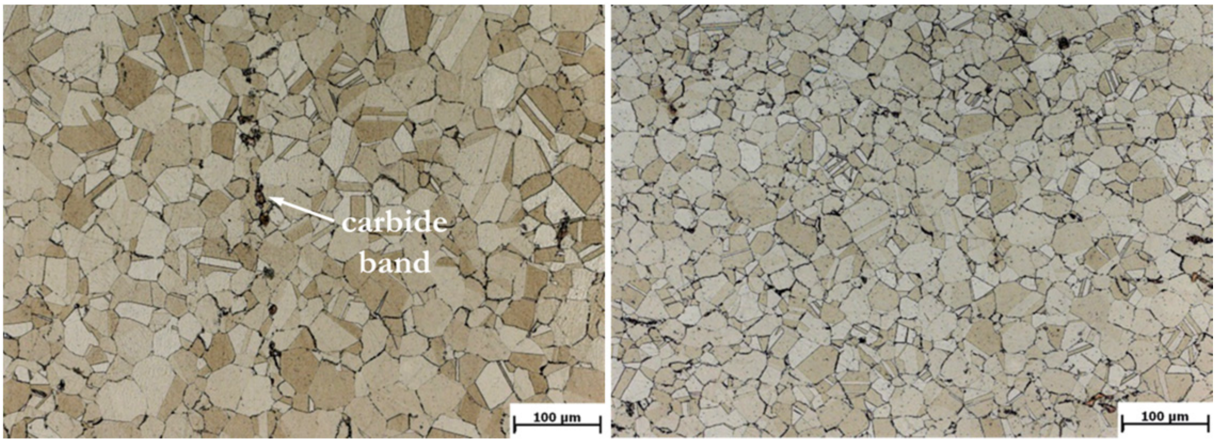

Figure 78. LOM micrographs of Allvac 718Plus in longitudinal (left, specimen 5) and transverse specimen direction (right) showing carbide bands and annealing twins

Table 26. Grain size of Allvac 718Plus specimens in the undeformed zone

specimen	**grain size**, µm
0	45 ± 25
2	55 ± 30
4	50 ± 25
7	50 ± 30
8	50 ± 25
9	45 ± 20

The light, needle-shaped grain-boundary precipitates observed in **Figure 78** are assumed to be δ phase. As for Inconel 718, twin boundaries seem to be mostly free of precipitates. **Figure 79** also shows dark, spherical precipitates inside grains. These particles with a diameter of 80 ± 15 nm and a volume fraction of 16% are suggested to be γ' phase.

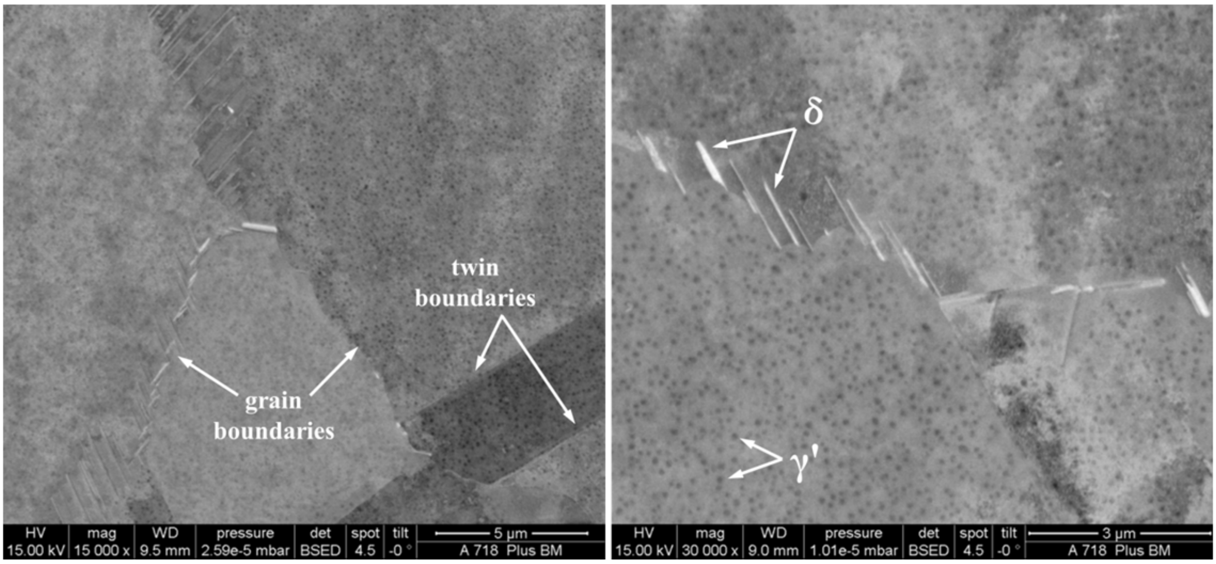

Figure 79. FEG-SEM BSE-image of Allvac 718Plus base material showing precipitates at grain boundaries and inside grains

5.2.2.2 *Deformed material*

Figure 80 shows LOM micrographs of the deformed microstructure in the specimen center. Similar to Inconel 718, grains are elongated orthogonally to the direction of external stress. **Figure 81** shows the deformed microstructure near the specimen border. As in Inconel 718, deformation bands and few pores near carbides are observed (see also **Figure 82**).

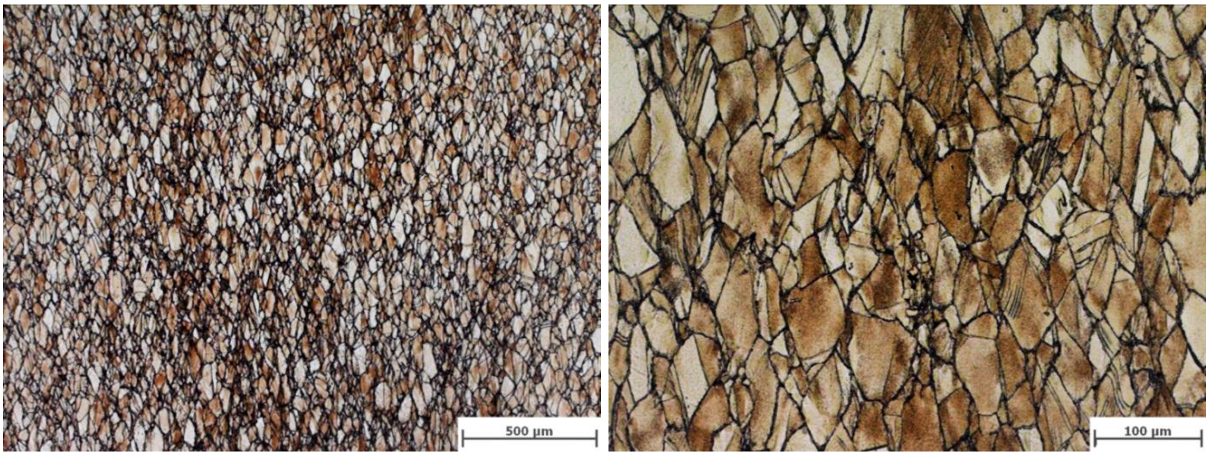

Figure 80. LOM micrographs of deformed Allvac 718Plus microstructure in the specimen center showing deformed grains (specimen 2, σ_{max} = -350 MPa/ε_{pl} = 0.52)

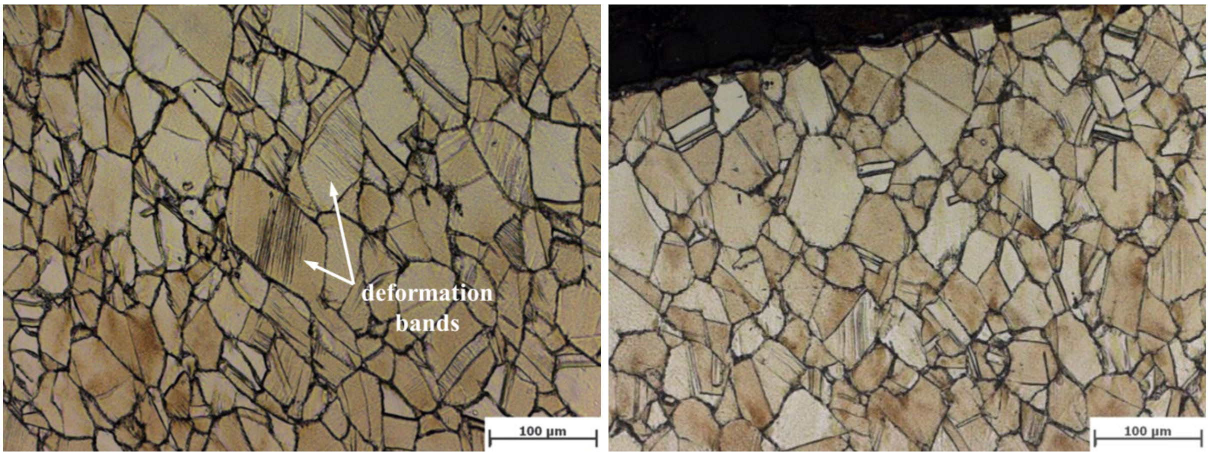

Figure 81. LOM micrographs of deformed Allvac 718Plus microstructure at the specimen border showing deformation bands (specimen 2)

Figure 83 shows different positions of the deformed microstructure in the specimen center near grain boundaries. Compared to the base material, no considerable coarsening of γ' particles could be observed. There are, however, less spherical γ' precipitates observable inside grains. Instead, new small needle-shaped particles of different size and orientation are found. This suggests that a partly transformation of γ' to δ phase occurred during the forging simulation.

As in Inconel 718, small recrystallized grains are observed at grain boundaries. In comparison, however, their number seems to be slightly lower and fewer coarse grain boundary δ precipitates are observed.

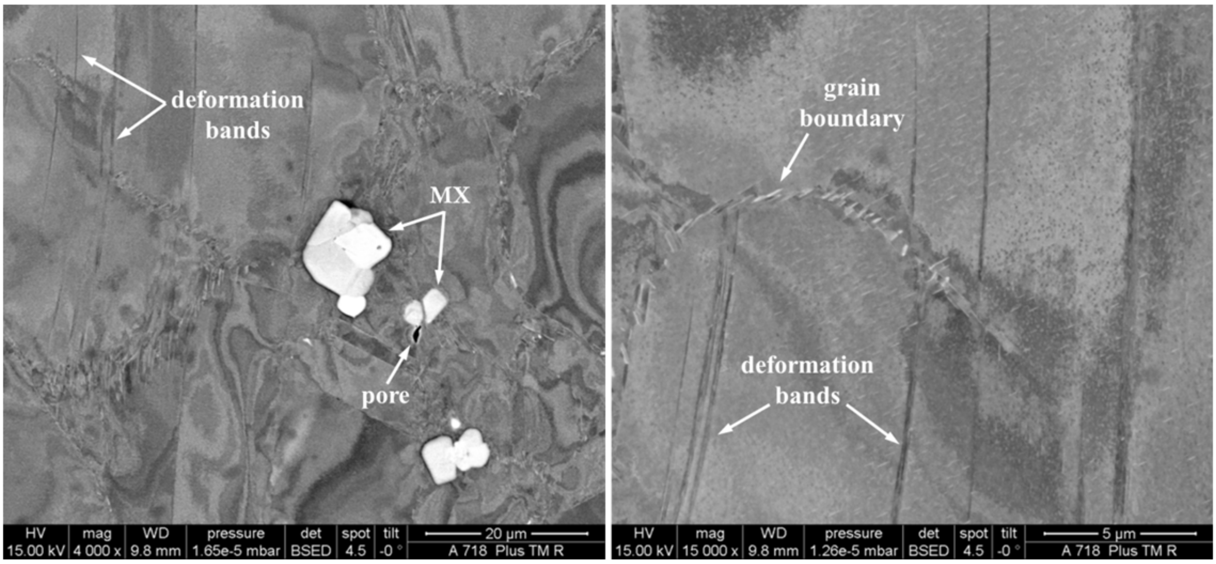

Figure 82. FEG-SEM BSE-images of deformed Allvac 718Plus microstructure at the specimen border showing deformation bands, precipitates and pores (specimen 2)

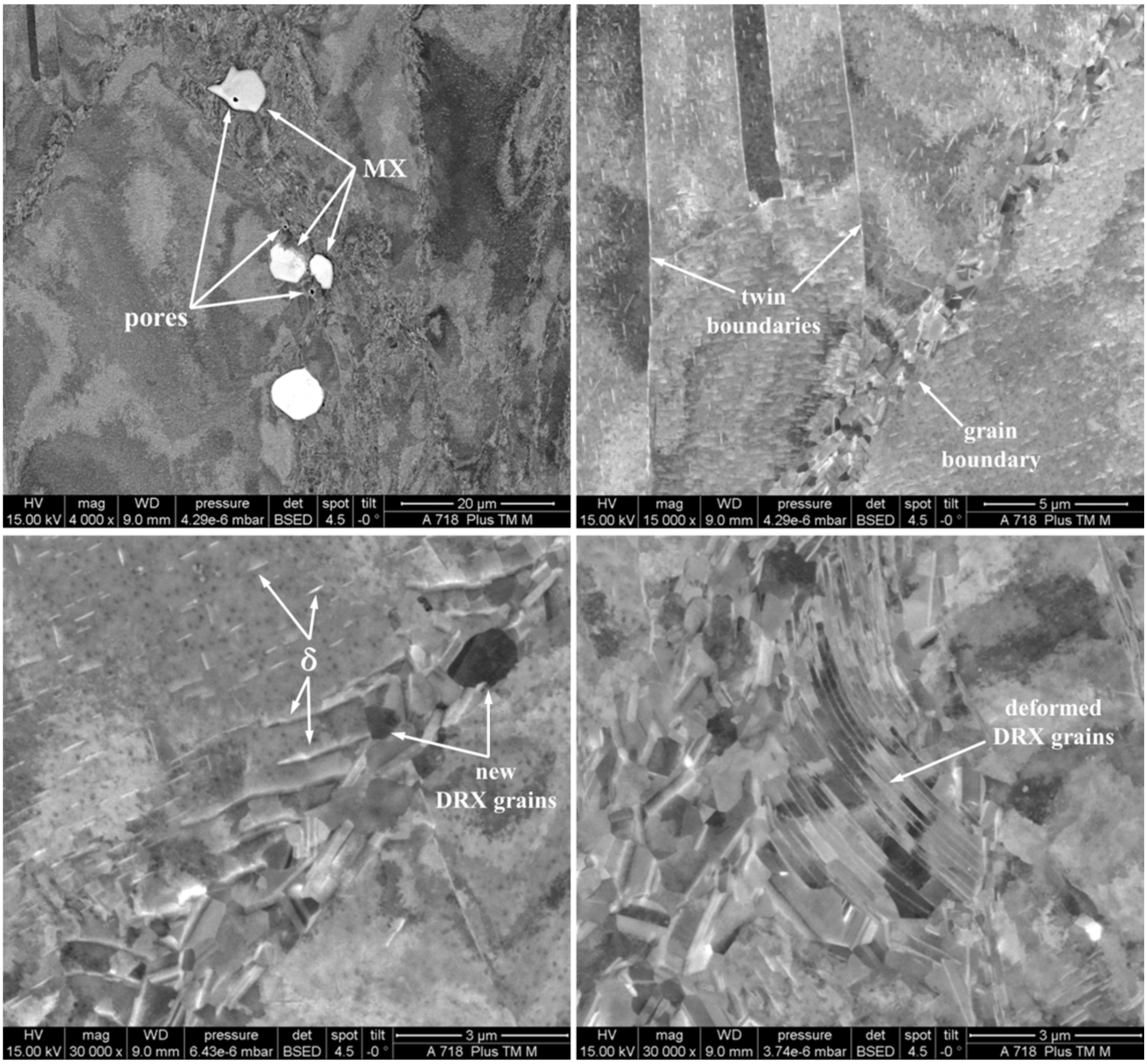

Figure 83. FEG-SEM BSE-images of deformed Allvac 718Plus microstructure in the specimen center showing different precipitates, recrystallized grains and pores (specimen 2)

5.2.3 Haynes 282

5.2.3.1 Base material

Figure 84 shows micrographs of undeformed Haynes 282 base material in longitudinal specimen (i.e. in transverse billet) direction. As for the other investigated alloys, the grain morphology is similar in transverse and longitudinal direction (see **Figure 85**).

As shown in **Table 27**, Haynes 282 microstructure shows the largest average grain size. There are, however, large variations in grain size, i.e. there are many small but also few very large grains (see **Figure 86**). Slight grain size variation over the specimen length was observable for certain specimens.

As in the other alloys, many large particles of different shape were found inside grains. Due to their grey and orange appearance, they are suggested to be primary carbonitrides of MX type (see **Figure 84**). As in Allvac 718Plus, these particles partly exhibit ordered band structure in longitudinal billet (i.e. transverse specimen) direction.

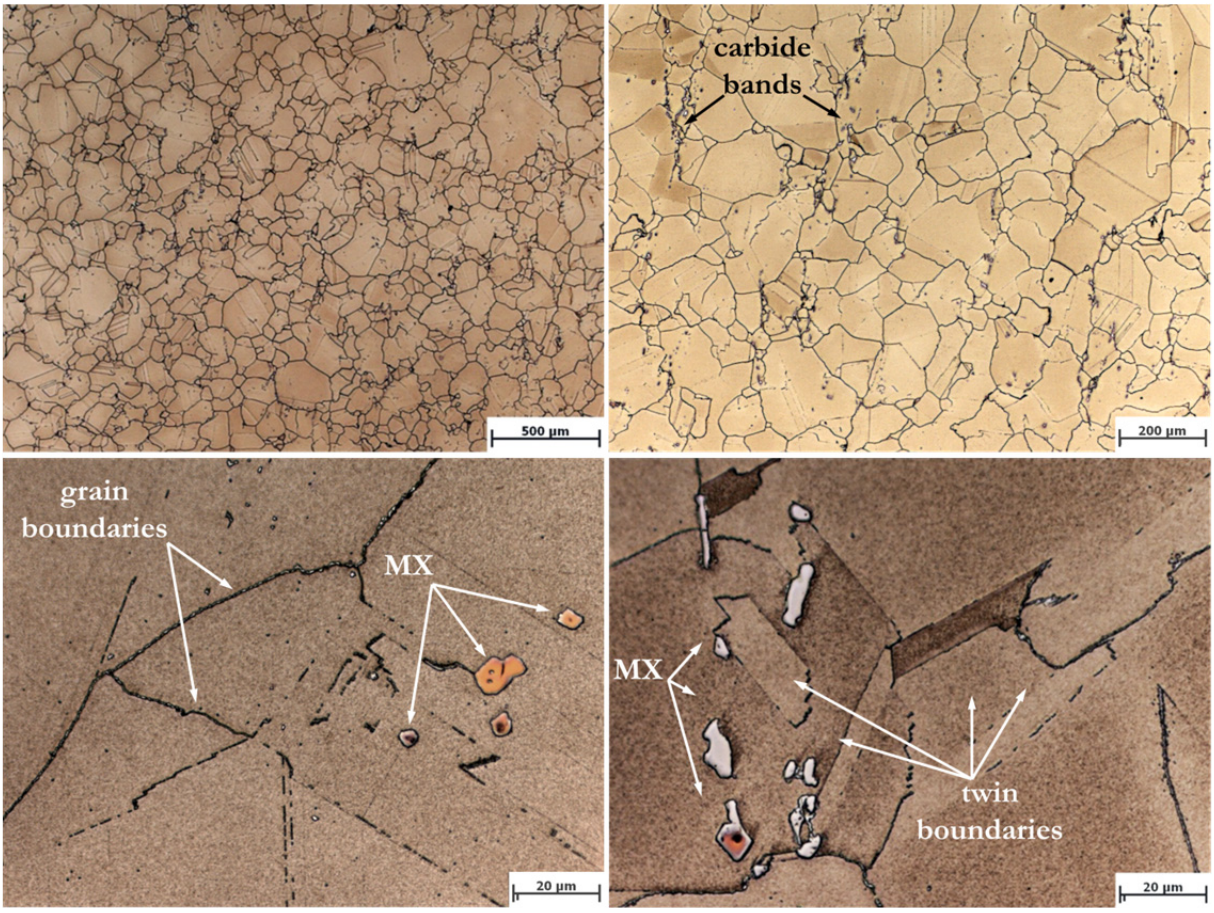

Figure 84. LOM micrographs of Haynes 282 base material showing carbides (specimen 9)

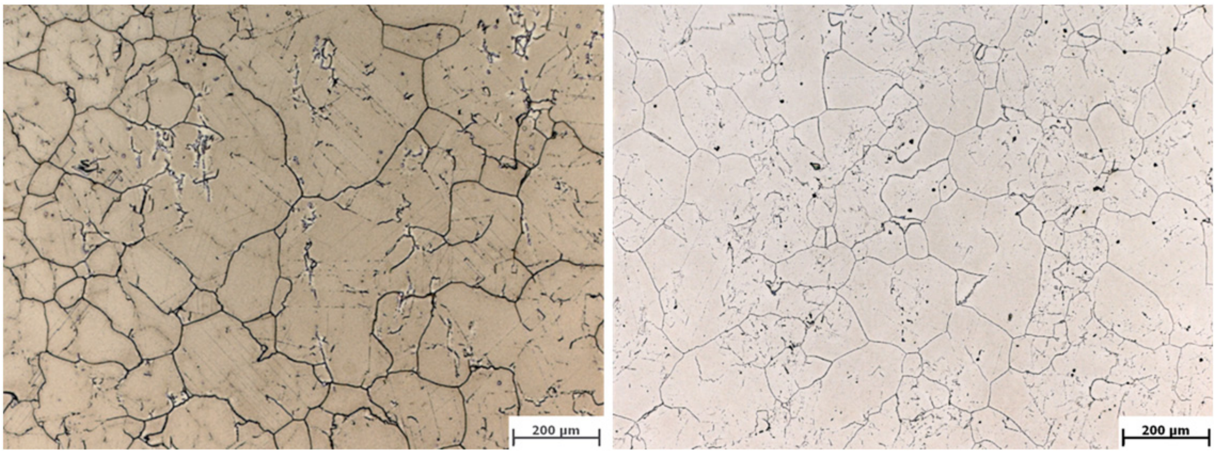

Figure 85. LOM micrographs of Haynes in transverse (left, specimen 4) and longitudinal billet direction (right)

Table 27. Grain size of Haynes 282 specimens in the undeformed zone

specimen	**grain size**, µm
0	150 ± 90
1	125 ± 75
2	120 ± 70
3	160 ± 100
4	175 ± 115
7	180 ± 110
9	115 ± 70
10	175 ± 115

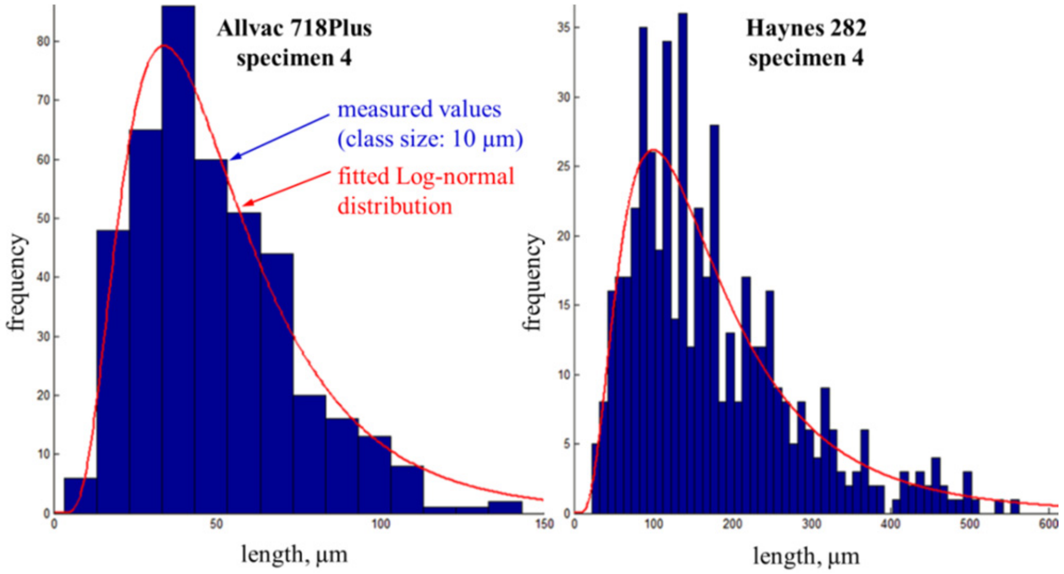

Figure 86. Comparison of typical grain size distributions of Allvac 718Plus (left) and Haynes 282 (right)

Figure 87 shows FEG-SEM images of Haynes 282 base material. Grain boundaries are almost entirely occupied by precipitates of different appearance (presumably MC, M_6C and $M_{23}C_6$ carbides). Coherent twin boundary segments, however, are mostly free of particles.

Small spherical precipitates with a mean diameter of 35 ± 5 nm and dark appearance are found inside grains. They exhibit a phase fraction of 18% and are suggested to be γ' phase.

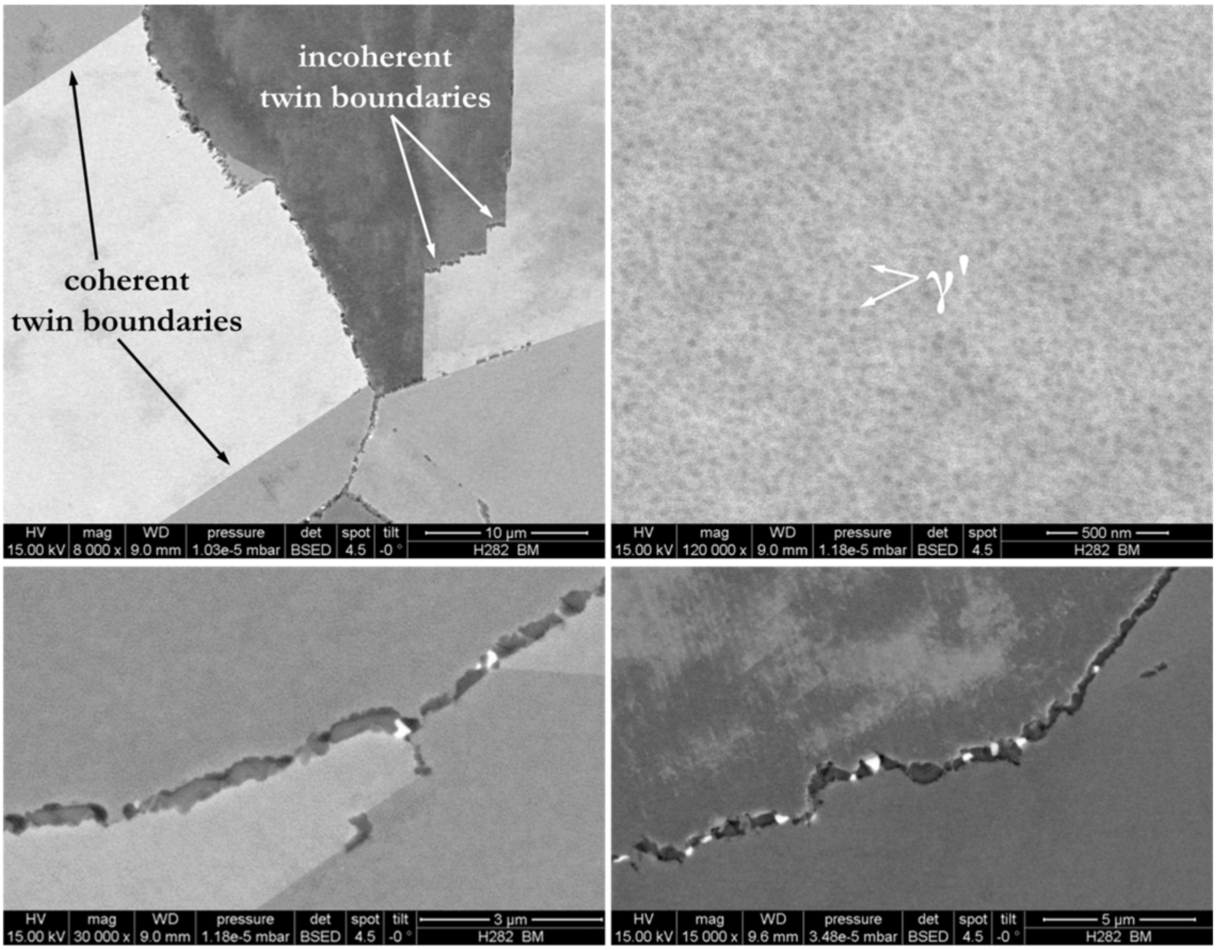

Figure 87. FEG-SEM BSD-images of Haynes 282 base material showing different precipitates at grain boundaries, twin boundaries and inside grains (specimen 2)

5.2.3.2 *Deformed material*

Figure 88 shows LOM micrographs of deformed Haynes 282 specimens in the specimen center. Similar to the other investigated alloys, grains are strongly deformed at high plastic strains. At lower strains, grain deformation is less distinct but deformation bands are still occasionally observed.

Evidently, more deformation bands occur at high plastic strains in strongly deformed areas, especially near the specimen border (see **Figure 89**). Locally, deformation bands propagated through grains to the specimen surface which lead to the formation of small protrusions. Furthermore, as in the other alloys, some (mostly intergranular) surface cracks are observed.

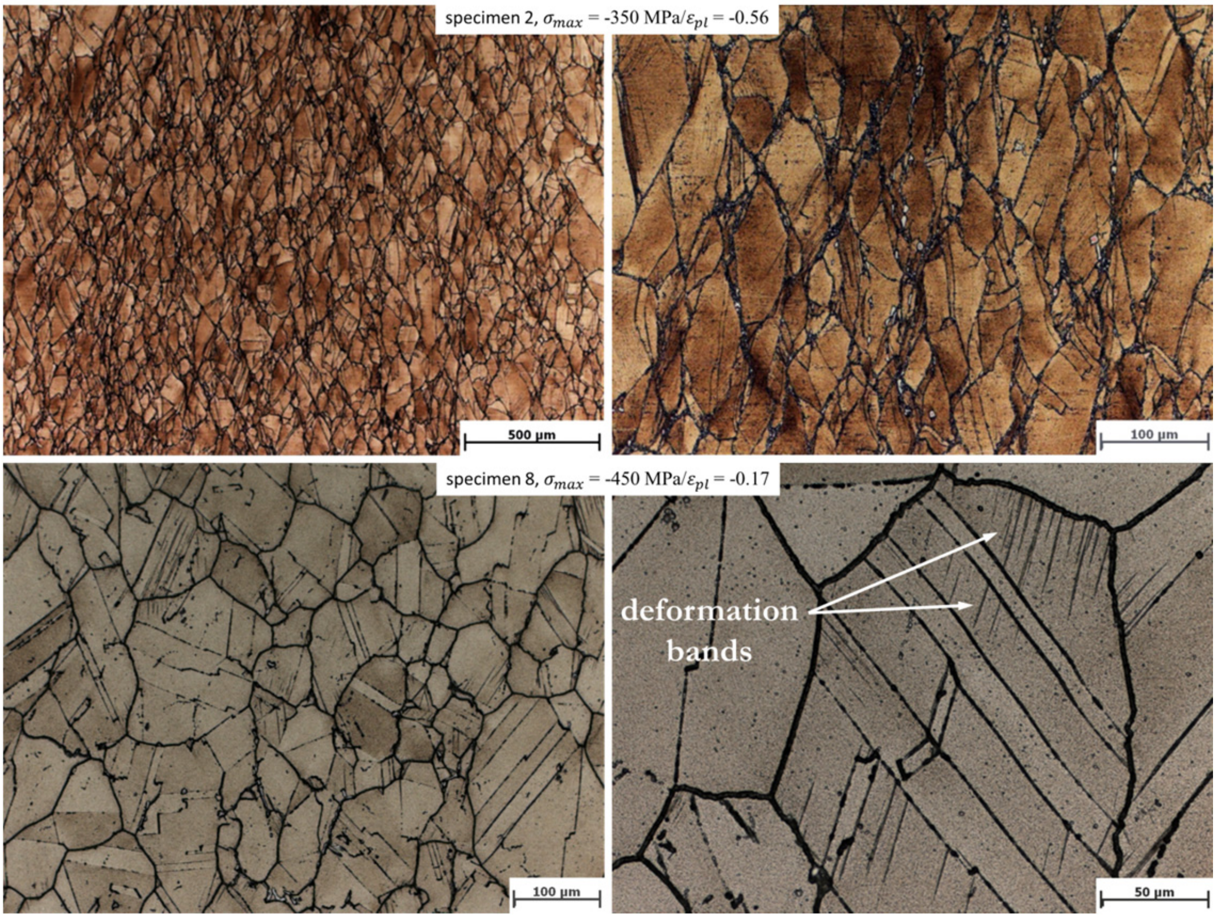

Figure 88. LOM micrographs of deformed Haynes 282 microstructure in the specimen center showing deformed grains and deformation bands

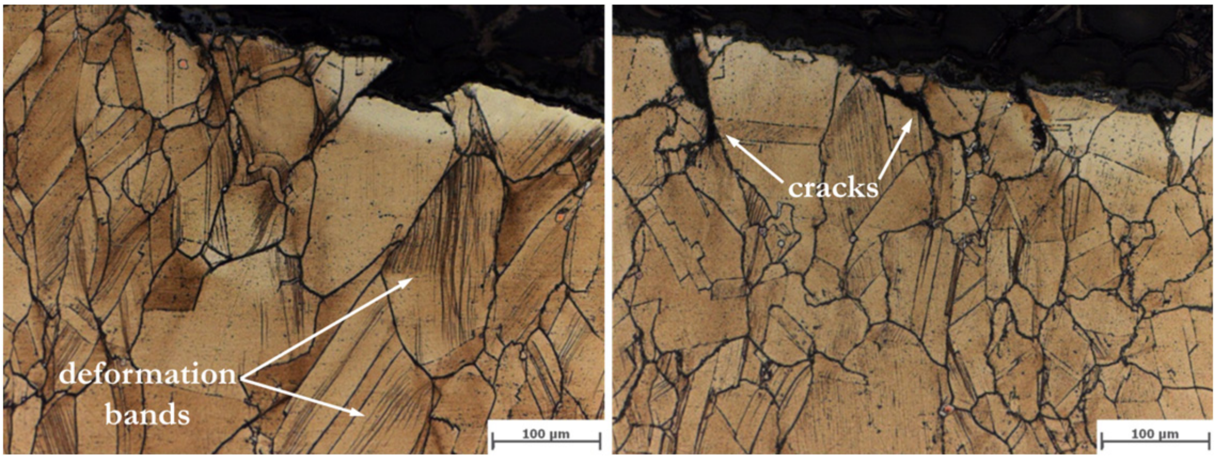

Figure 89. LOM micrographs of deformed Haynes 282 microstructure at the specimen border showing deformation bands and surface cracks (specimen 2)

Figure 90 shows FEG-SEM images of deformed Haynes 282 microstructure at different specimen center positions. As in the other alloys, small, precipitate-free grains were found at grain boundaries as evidence that DRX occurred. Furthermore, γ' particle coarsening to a diameter of 55 ± 10 nm was observed.

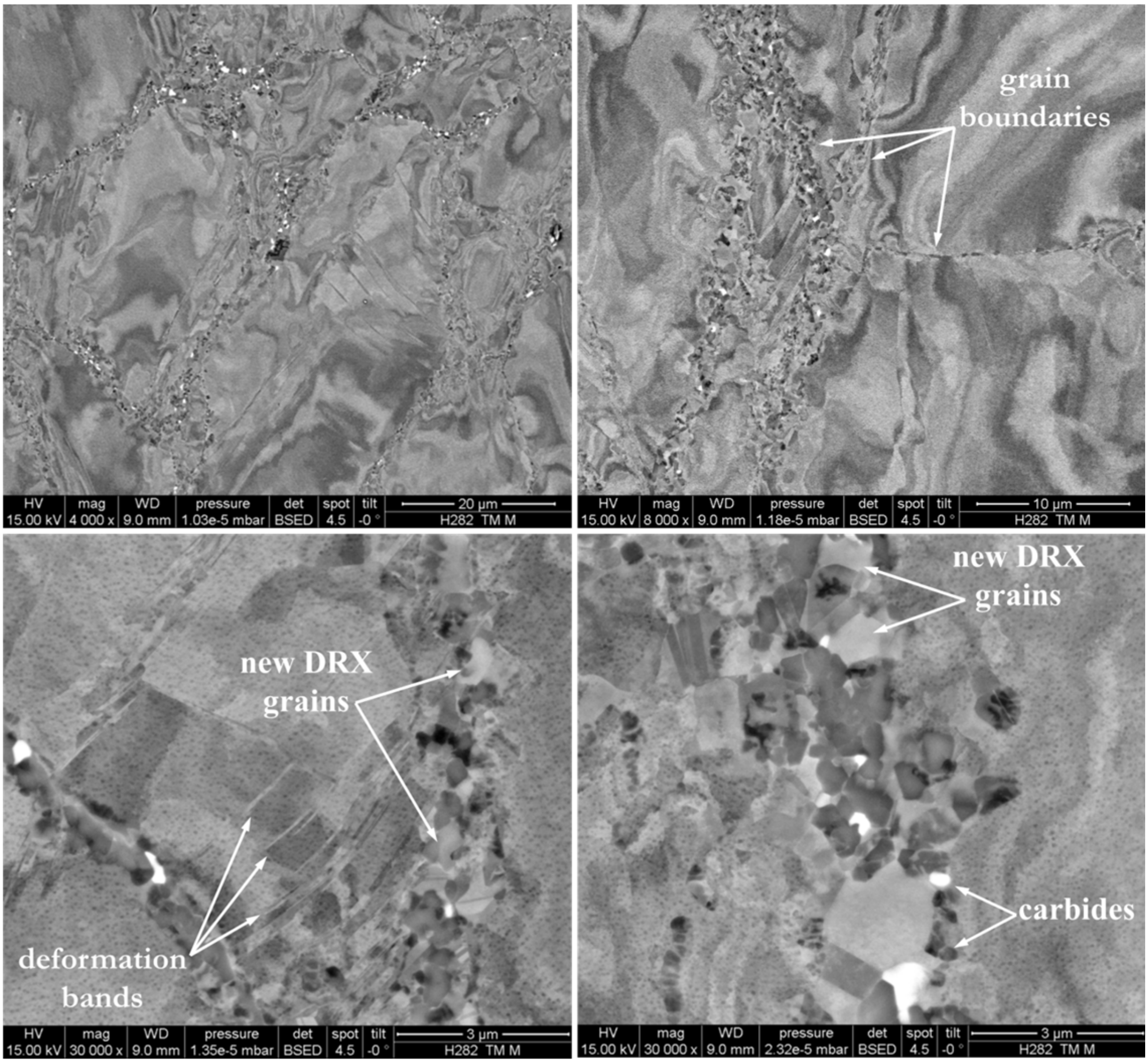

Figure 90. FEG-SEM BSE-images of deformed Haynes 282 microstructure in the specimen center showing recrystallized grains, precipitates and deformation bands (specimen 2)

5.3 Numerical simulation

5.3.1 Thermodynamic equilibrium

5.3.1.1 Inconel 718

Figure 91 shows the calculated equilibrium phases of Inconel 718. The resulting solidus and liquidus temperatures are around 1220 °C and 1345 °C, respectively.

Below around 940 °C, a small amount of η phase is present and below 910 °C, the TCP σ phase occurs. $M_{23}C_6$ replaces MC phase at around 700 °C. The calculated solvus temperatures of γ' and δ phases are around 900 °C and 1055 °C, respectively. As anticipated, γ'' phase does not appear in equilibrium state.

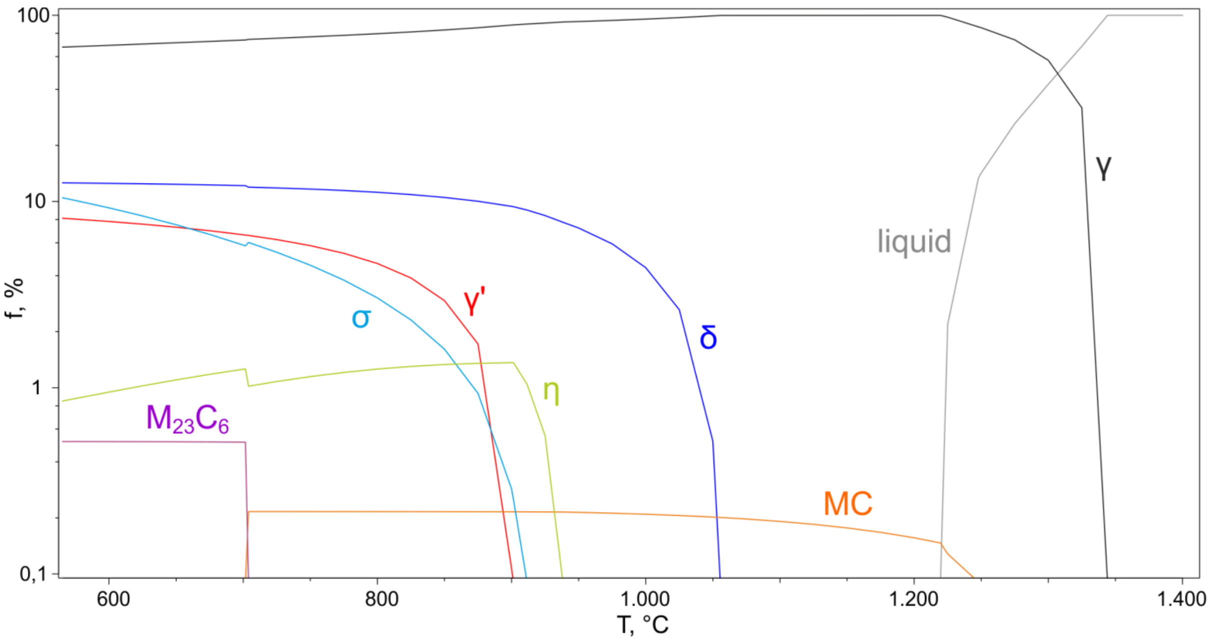

Figure 91. Equilibrium phases of Inconel 718

5.3.1.2 Allvac 718Plus

Figure 92 shows the results of the stepped equilibrium calculation for Allvac 718Plus. They are similar to Inconel 718 as solidus and liquidus temperatures are around 1135 °C and 1355 °C, respectively, and the same phases appear except for η phase.

Below around 780 °C, $M_{23}C_6$ is more stable than MC and σ phase is present below around 750 °C. The calculated solvus temperatures of γ' and δ are around 975 °C and 1050 °C, respectively. In comparison with Inconel 718, the solution temperature and phase fraction of γ' is significantly higher (around 75 °C and 18%, respectively).

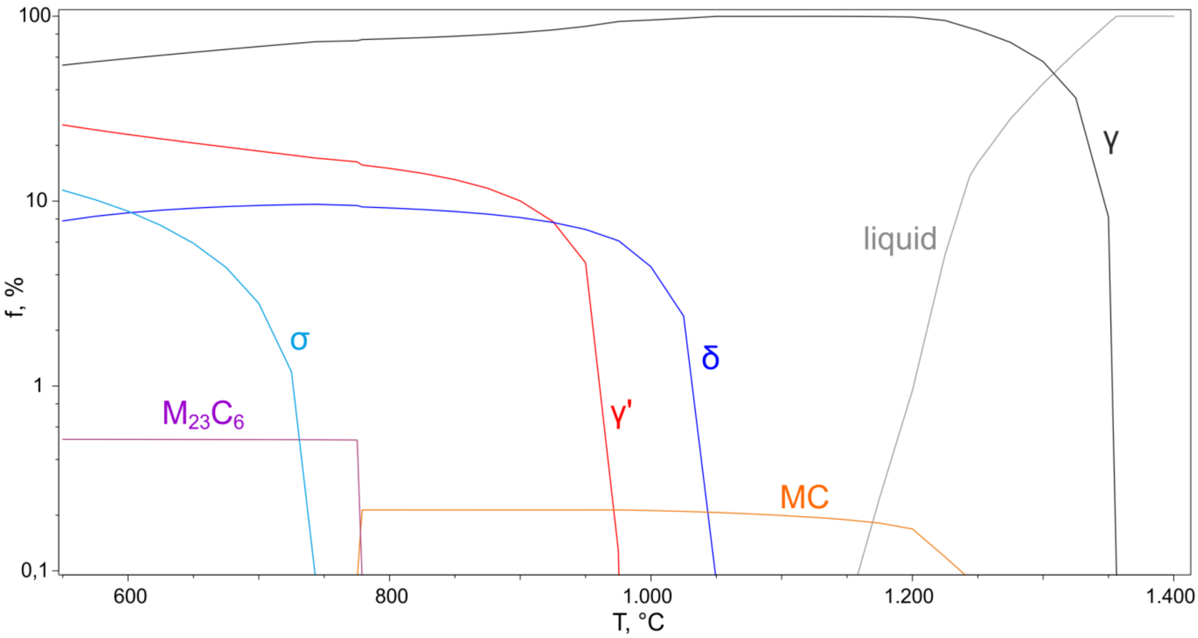

Figure 92. Equilibrium phases of Allvac 718Plus

5.3.1.3 Haynes 282

Figure 93 shows the calculated equilibrium phases of Haynes 282. The alloy's solidus and liquidus temperatures are around 1255 °C and 1340 °C, respectively.

Compared to Inconel 718 and Allvac 718Plus, Haynes 282 exhibits two additional equilibrium phases, the TCP μ phase as well as secondary carbides of M_6C type. These carbides have a solution temperature of 1015 °C and are replaced by $M_{23}C_6$ below around 750 °C. The calculated γ' solvus temperature of around 1040 °C is noticeably higher compared to the two other alloys.

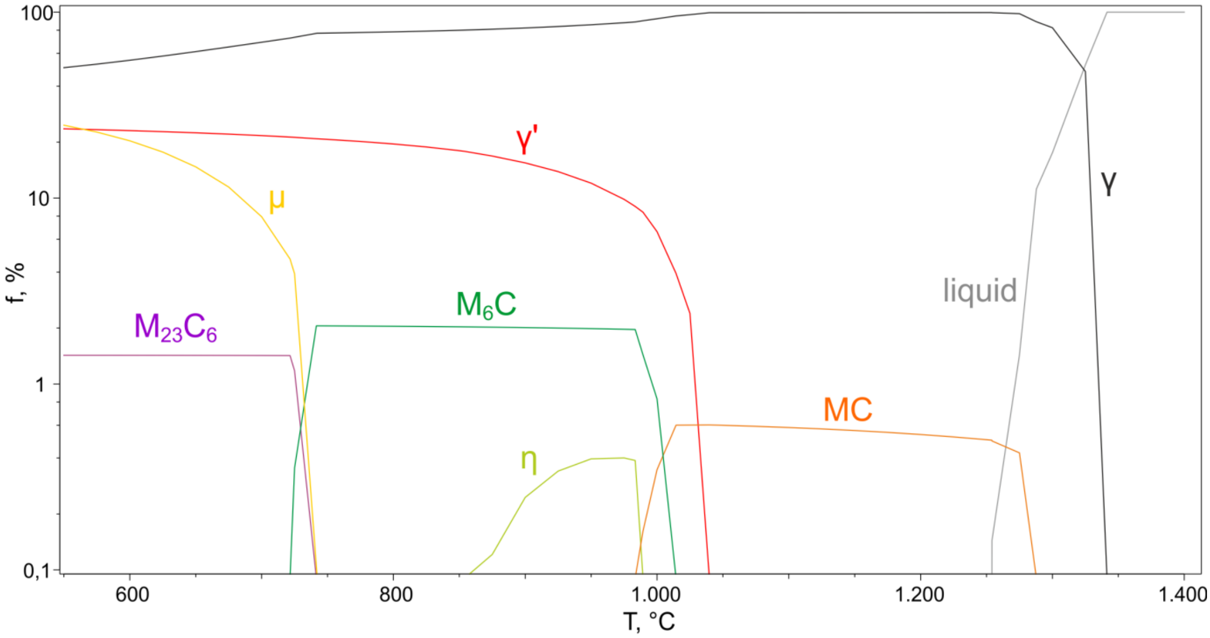

Figure 93. Equilibrium phases of Haynes 282

5.3.2 Precipitation of primary carbides during solidification

The results of the Scheil-Gulliver simulations are summarized in **Table 28**. All alloys show rather low phase fractions of primary carbides. As N was neglected in the calculations, their type is (Nb,Ti)C in Inconel 718 and Allvac 718Plus and (Ti,Cr,Mo)C in Haynes 282, respectively.

Table 28. Phase fractions and chemical composition of primary MC carbides

	phase fraction	**chemical composition**, at.%			
		Nb	**Ti**	**Cr**	**Mo**
Inconel 718	0.4%	28.2	23.1	1.1	0.1
Allvac 718Plus	0.2%	31.5	19.8	1.0	< 0.1
Haynes 282	0.4%	-	44.1	6.7	4.2

5.3.3 Precipitation kinetics during heat treatment and forging

5.3.3.1 Inconel 718

Figure 94 shows the resulting phase fractions (f), mean particle diameters (d) and number densities (N) of the considered precipitate phases during heat treatment of Inconel 718. These precipitate parameters are related to each other via[94]

$$f = \frac{\pi}{6} d^3 N \qquad [13]$$

γ' and γ'' phases nucleate during cooling after solution annealing and grow to final mean diameters of 36 nm and 85 nm, respectively (see **Table 29**). The small size of γ' could be the reason why it was not clearly experimentally detectable via FEG-SEM. After tempering, γ' and γ'' phases obtain phase fractions of 3.8% and 12.2%, respectively. This is in good agreement with typical values stated in literature and, in the case of γ'', with experimental findings (70 nm/14%).

δ phase forms during solution annealing and obtains a final phase fraction of 1.3% and a mean diameter of 392 nm after heat treatment. Secondary MC precipitates with a mean diameter of 89 nm and a rather low phase fraction of 0.2% form during solution annealing and remain at constant phase fraction and size during the rest of the heat treatment.

The phase fractions, average size and chemical composition of all precipitate phases as well as the γ matrix are summarized in **Table 29**.

Table 29. Phase fraction, average size and chemical composition of Inconel 718 precipitate phases and matrix after heat treatment

phase	***f***	***d***, nm	**chemical composition**, at.%							
			Ni	**Co**	**Cr**	**Fe**	**Mo**	**Nb**	**Ti**	**Al**
γ	82.4%	-	48.5	0.2	26.1	21.7	2.2	0.3	0.1	0.9
γ'	3.8%	36	72.5	0.2	1.1	2.1	0.4	7.5	9.2	7.0
γ''	12.2%	85	73.4	< 0.1	0.2	1.6	< 0.1	19.1	5.6	< 0.1
δ	1.3%	392	74.8	< 0.1	0.1	< 0.1	0.1	25.0	< 0.1	< 0.1
MC	0.2%	89	-	-	-	-	-	27.1	22.9	-

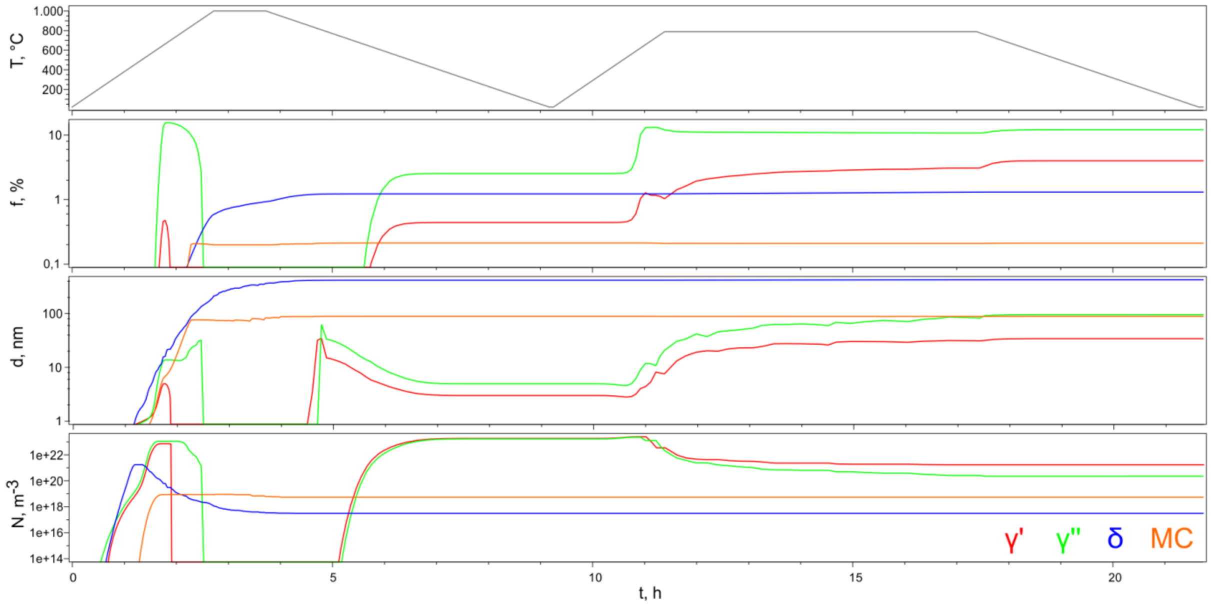

Figure 94. Precipitation kinetics of Inconel 718 during heat treatment

In the subsequent forging simulation, the dislocation density evolved according to the strain rate and peaked at around five times the initial value ($5 \cdot 10^{11}$ m^{-3}) during forging (see **Figure 95**).

The average size of γ' and γ'' phases stayed nearly constant during forging. Their phase fractions, however, decrease to 2.6% (γ') and 8.8% (γ''), respectively. Grain boundary δ phase does not significantly change in size or quantity and only a low number ($1.5 \cdot 10^{13}$ m^{-3}) of very small δ precipitates (≈ 1 nm) nucleate at dislocations.

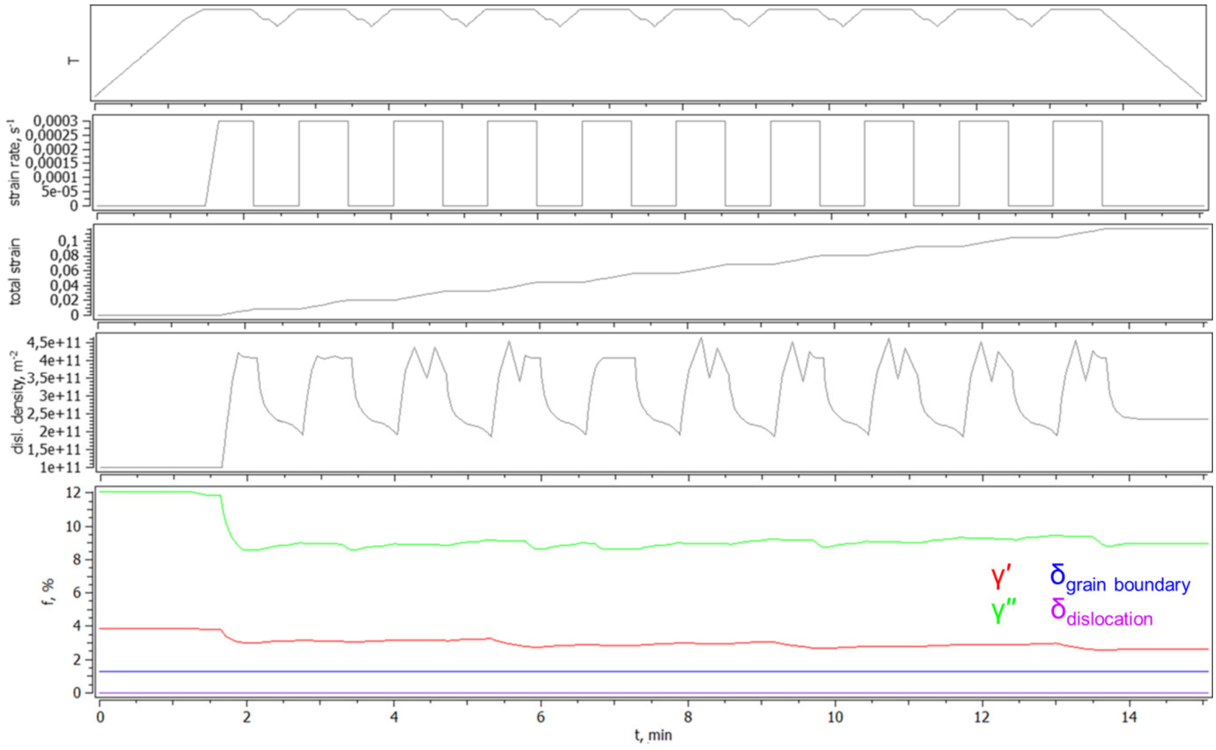

Figure 95. Evolution of dislocation density and precipitate phase fractions in Inconel 718 during forging

5.3.3.2 Allvac 718Plus

Figure 96 shows the heat treatment simulation results of Allvac 718Plus. Similar to Inconel 718, δ phase forms during solution annealing and stays at nearly constant phase fraction and size during heat treatment. Its mean diameter is slightly larger as in Inconel 718 and it obtains higher phase fraction after heat treatment (3.3%) which is consistent with experimental results.

γ' phase, on the other hand, nucleates during cooling after solution annealing as well as the beginning of each tempering stage. The phase exhibits a final volume fraction of 16.4% and a mean diameter of 76 nm after the second tempering stage which is in excellent agreement with experimental results (16%/80 nm). It consists mainly of Ni, Co, Nb, Al and Ti, see **Table 30**.

Table 30. Phase fraction, average size and chemical composition of Allvac 718Plus precipitate phases and matrix after heat treatment

phase	***f***	***d*, nm**	**chemical composition, at.%**								
			Ni	**Co**	**Cr**	**Fe**	**Mo**	**W**	**Nb**	**Ti**	**Al**
γ	80.2%	-	48.0	9.5	24.7	12.0	2.0	0.4	0.4	< 0.1	3.0
γ'	16.4%	76	64.9	8.5	1.3	0.7	0.1	0.1	13.9	5.1	5.4
δ	3.3%	422	74.8	< 0.1	0.1	< 0.1	< 0.1	-	25.0	< 0.1	< 0.1
MC	0.2%	82	-	-	-	-	-	-	29.3	20.7	-

As in Inconel 718, only a rather small amount of MC phase formed during solution annealing and stayed at constant size and phase fraction during the rest of the heat treatment.

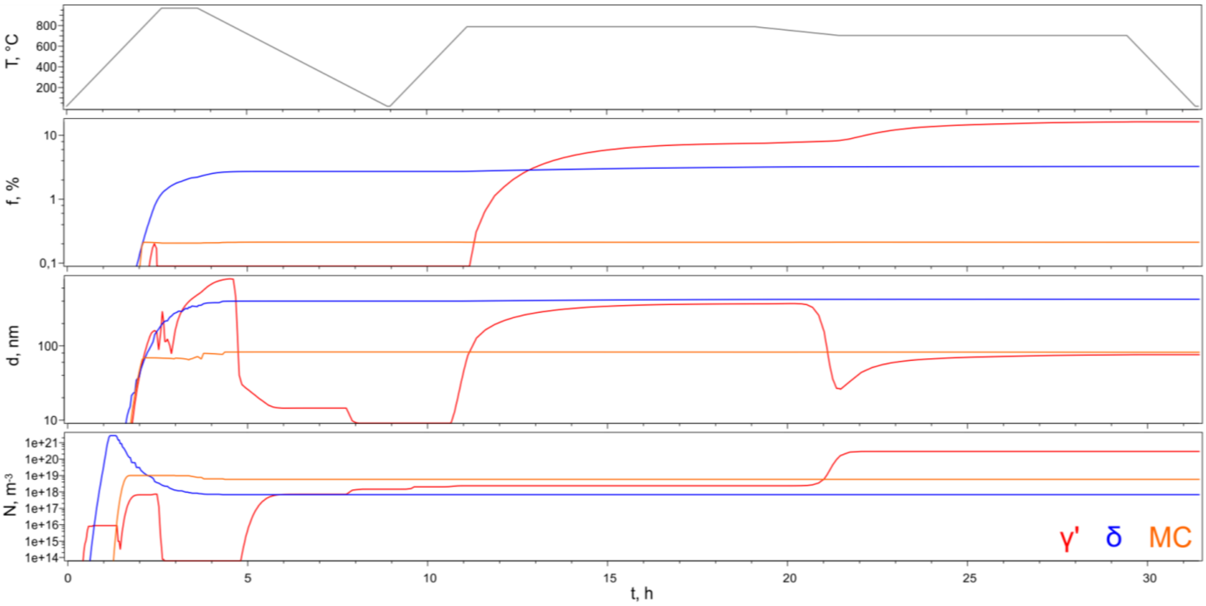

Figure 96. Precipitation kinetics of Allvac 718Plus during heat treatment

In the subsequent forging simulation, the phase fraction of γ' slightly decreased to 14.8% while its mean particle diameter increased to 91 nm (see **Figure 97**). The dislocation density reached peak levels of twice the initial value during forging. As in Inconel 718, no significant change in size and amount of grain boundary δ phase occurs during forging and hardly any δ precipitates nucleate at dislocations.

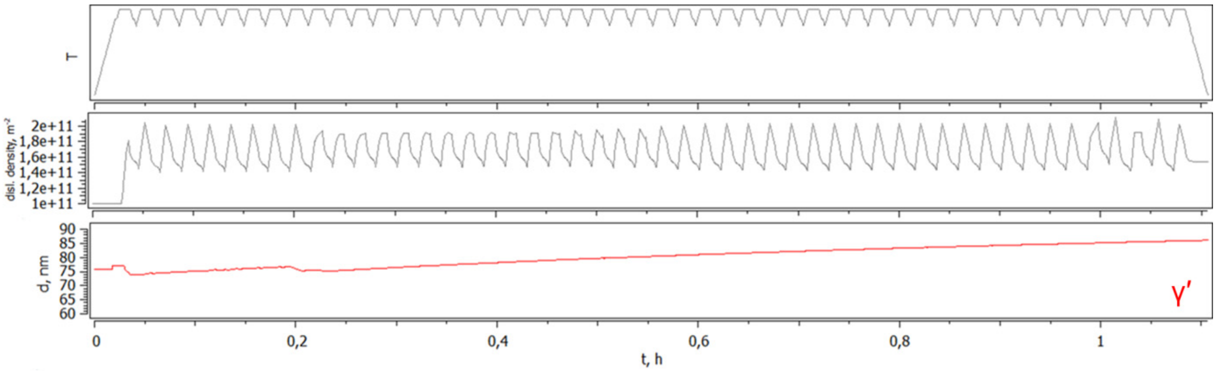

Figure 97. Evolution of dislocation density and γ' size in Allvac 718Plus during forging

5.3.3.3 Haynes 282

Figure 98 shows the simulation results of Haynes 282 heat treatment and **Table 31** shows the phase fractions, mean diameters and chemical composition of γ' phase, secondary carbides as well as the γ matrix after heat treatment.

The major carbide phases are grain boundary M_6C and MC which form during solution annealing and obtain phase fractions of 1.3% and 0.2%, respectively. MC phase at dislocations and grain boundary $M_{23}C_6$ phase dissolve during solution annealing and nucleate again in the second heat treatment stage. However, only a very small amount of small MC and rather large $M_{23}C_6$ is present at dislocations and grain boundaries, respectively, at the end of heat treatment. Generally, the final average diameters of grain boundary MC, M_6C and $M_{23}C_6$ in the range of around 1-3 µm is in good agreement with experimental results.

γ' phase nucleates during cooling after solution annealing and obtains a phase fraction of 18.4% after heat treatment which is in excellent agreement with experimental results (18%).

Its low final mean diameter of 28 nm results from the nucleation of many small precipitates during cooling after precipitation hardening. Without them, the mean diameter of γ' phase would be around 260 nm which is much larger as experimentally determined. The reason for this discrepancy is unclear, especially as similar results were obtained for varying calculation parameters and different combinations of considered phases.

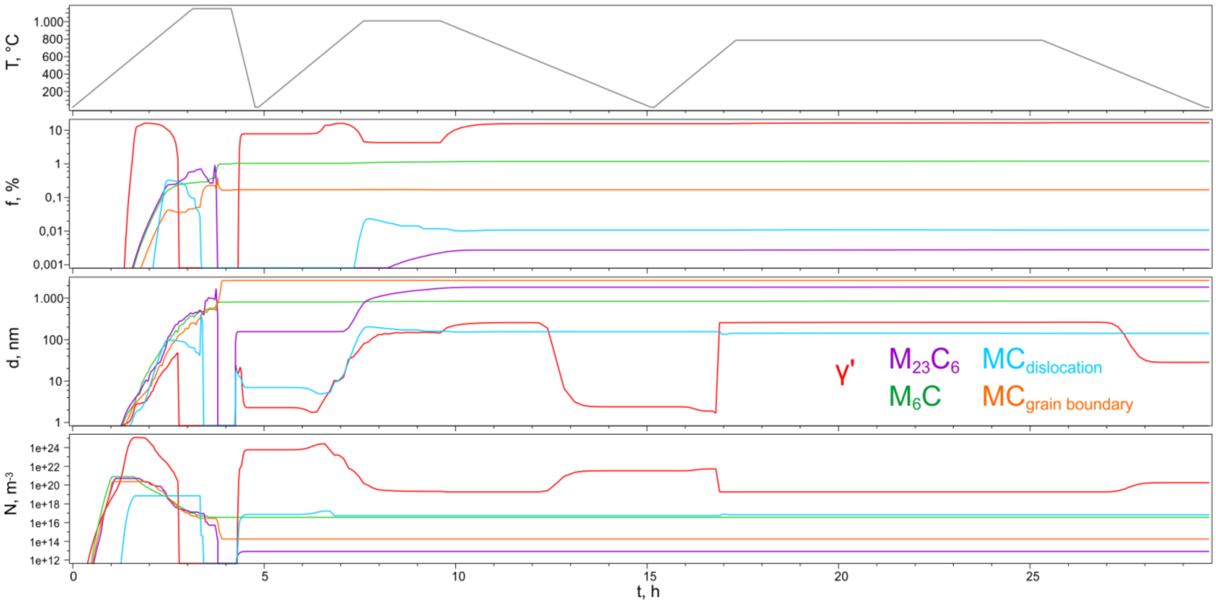

Figure 98. Precipitation kinetics of Haynes 282 during heat treatment

Table 31. Phase fraction, average size and chemical composition of Haynes 282 precipitate phases and matrix after heat treatment

phase	***f***	***d*, nm**	**chemical composition**, at.%						
			Ni	**Co**	**Cr**	**Fe**	**Mo**	**Ti**	**Al**
γ	80.1%	-	53.3	11.9	26.2	1.0	5.8	0.2	1.4
γ'	18.4%	28	71.0	3.2	1.0	< 0.1	0.3	12.5	12.0
MC_{gb}	0.2%	2680	-	-	7.3	-	< 0.1	42.7	-
MC_d	< 0.1%	142	-	-	7.6	-	< 0.1	42.2	-
$M_{23}C_6$	< 0.1%	1856	13.1	0.2	55.8	< 0.1	10.1	-	-
M_6C	1.3%	851	24.4	4.3	27.3	< 0.1	29.7	-	-

Haynes 282 did not exhibit any considerable microstructural changes during forging except for a negligible increase in $M_{23}C_6$ particle size to 1.92 μm and a slight reduction of γ' phase fraction to 16.9% during the early forging phase from when on it remained constant (see **Figure 99**).

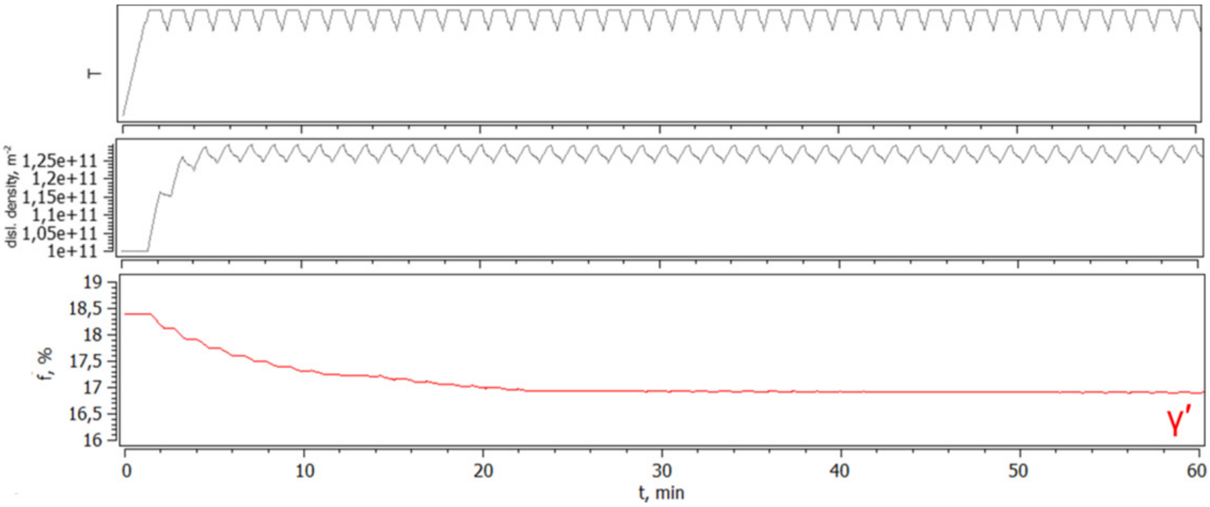

Figure 99. Evolution of dislocation density and γ' size in Haynes 282 during forging

5.4 Summary of results

Thermomechanical tests were carried out to simulate the forging process at three different maximum stress levels. During these tests, plastic deformation of tensile specimens occurred at considerably different rates in each investigated alloy. Typical strain curves showed roughly linear behavior up to low plastic strains (≈ 0.1) followed by a progressive increase in strain. The alloys' minimum strain rates were determined from these strain curves and found to depend on the maximum stress according to power-law relationships with different exponents. The determination of these stress exponents was based on the simplifying assumption that the tests were carried out at constant stress and temperature. Furthermore, it was assumed that no changes in the precipitate state of the alloys occurred during deformation up to low strains which was reviewed via precipitation kinetics simulations in MatCalc.

All three investigated Ni-base alloys are strengthened by small, coherent precipitate phases inside grains and larger grain boundary precipitates. In the case of precipitation hardened Inconel 718, disk-shaped precipitates with average particle size of 70 nm and a phase fraction of 14% were detected via FEG-SEM and are suggested to be γ'' phase. The presence of γ' precipitates could not be clearly proven experimentally. However, MatCalc simulations predict the precipitation of both γ'' and γ' phase of type $Ni_3(Nb,Ti)$ and $Ni_3(Ti,Nb,Al)$, respectively, with a total phase fraction of around 16% after heat treatment.

Furthermore, Inconel 718 was observed to contain grain boundary precipitates, presumably δ phase (Ni_3Nb). The assumption is supported by numerical simulations which predict a δ phase fraction of around 1% in precipitation hardened condition.

MatCalc simulations of the forging process show a slight decrease in γ' and γ'' phase fractions in the early stage of deformation. FEG-SEM investigations on a strongly deformed Inconel 718 specimen showed δ phase coarsening. However, no strong change in size and quantity of γ'' phase was observable even though it is assumed that partial transformation to δ phase occurred.

Contrary to Inconel 718, Allvac 718Plus contains no γ'' phase but only spherical γ' phase with high Nb content. The experimentally determined size (80 nm) and quantity (16%) of the phase in precipitation hardened condition was validated by numerical simulations. In comparison to Inconel 718, more δ phase was experimentally observed at grain boundaries. This is validated by simulations which predicted a phase fraction of around 3%.

MatCalc simulations predict slight coarsening of γ' phase during deformation up to low strains. It was experimentally observed that δ phase coarsened less strongly in Allvac 718Plus than in Inconel 718 during plastic deformation but γ' phase was found to have partially transformed to δ phase inside grains.

In contrast to the other two alloys, Haynes 282 contains no Nb and therefore no γ'' and δ phases. Instead, small spherical precipitates (average diameter 35 nm) were found inside grains and assumed to be γ' phase. Numerical simulations predict a γ' phase fraction of around 18% which is in excellent agreement well with experimental results.

Furthermore, different types of particles were found at grain boundaries in Haynes 282. In MatCalc they were identified as carbides of type $(Mo,Cr,Ni)_6C$, $(Ti,Cr)C$ and $(Cr,Ni,Mo)_{23}C_6$. The calculated phase fraction and size of these carbides after heat treatment seems to be reasonable. However, the predicted size of γ' particles differs strongly from experimental results.

FEG-SEM investigations revealed coarsened γ' particles in Haynes 282 in a strongly deformed specimen. For low strains, however, no γ' coarsening and no change in the precipitate parameters of carbides is predicted in MatCalc simulations.

In summary it can be stated that the precipitation microstructures of all materials do not change strongly during low-strain deformation according to numerical simulations. However, this was not experimentally validated as no comprehensive microstructural investigations of specimens with low strains were performed.

However, major microstructural changes were observed in strongly deformed specimens compared to the initial precipitation hardened state. These changes include severe deformation of the grain structure, deformation banding and softening mechanisms such as precipitate coarsening and/or transformation as well as dynamic recrystallization.

The alloys exhibited different grain sizes and grain size distributions. Haynes 282 obtained the largest average grain size (150 µm) followed by Inconel 718 (90 µm) and Allvac 718Plus (50 µm). Due to their sampling position, larger grain size variations were observed between different Inconel 718 specimens compared to the other alloys. For none of the alloys, however, a correlation between specimen grain size and thermomechanical performance was found.

6 Discussion

6.1 Performance comparison

The main performance criterion of the die material was defined as the service time until a maximum permitted strain is reached. For locally tolerable true plastic strain of 0.1 (≈ 10.5% engineering strain) to stay within production tolerances, the average number of withstood forging cycles of each alloy was determined from their strain curves. **Table 32** summarizes the results of this evaluation for all stresses.

Table 32. Comparison of forging cycles up to $\boldsymbol{\varepsilon_{pl}}$ = 0.1 for each alloy and stress

		Inconel 718	**Allvac 718Plus**	**Haynes 282**
$\boldsymbol{\sigma_{max}}$, MPa	**-450**	1 ± 0.5	10 ± 1	80 ± 30
	-350	10 ± 3	50 ± 10	480 ± 80
	-300	40 ± 10	160 ± 50	1230 ± 110

It is evident that Haynes 282 showed by far the best performance as it exhibited the lowest minimum strain rates (see chapter 5.1.3.4). The difference in the average number of withstood cycles between Haynes 282 and Allvac 718Plus is nearly one order of magnitude at all stress levels. Inconel 718 obtained the worst performance withstanding between 4 to 10 times less forging cycles than Allvac 718Plus on average.

Considering annual production volumes of up to 24 800 turbine blades and a total number of 177 300 forgings to be manufactured until 2023, even the performance of Haynes 282 at the lowest maximum stress level (i.e. -300 MPa) seems unsatisfactory. However, the material performance in the real forging process is assumed to be considerably better because the testing conditions (i.e. T_{max}, T_{min} and σ_{max}) were chosen to simulate an extreme scenario, i.e. the real process parameters are less severe.

Furthermore, the thermomechanical tests were designed to simulate the material behavior at the most heavily loaded region of the forging die. In reality, the highest thermal and mechanical load occurs only in a rather small volume of the die material. This volume is multilaterally supported by less strongly loaded material (see **Figure 40**, chapter 4.2.1) and therefore presumably not as easily deformed as a tensile sample in uniaxial thermomechanical tests.

6.2 Hot deformation mechanism

The dominating hot deformation mechanism in the (idealized linear) low strain region of the strain curves, was determined by evaluating the stress exponent of each alloy (see chapter 5.1.3.4). This simplified approach was based on the neglect of varying temperature and stress during the thermomechanical tests and on the assumption that no microstructural changes occurred during this early stage of deformation (steady-state phase). However, as the results were ambiguous, the approach was refined by taking a threshold stress σ_{th} into account according to equation [2] (see chapter 3.4.1.2). This stress is needed to detach dislocations from precipitates and can be modeled in different ways depending mainly on the predominant deformation mechanism.[57-61]

It is often assumed to be proportional to the Orowan stress which is defined as

$$\tau_0 = \frac{Gb}{\lambda} \tag{14}$$

where G and b are the material's shear modulus and Burger's vector, respectively, and λ the mean distance between strengthening particles which can be calculated from their respective mean diameter d and phase fraction f as follows:[94]

$$\lambda = d\sqrt{\frac{\pi}{6f} - 1} \tag{15}$$

The alloy's shear moduli at T_{max} were calculated from the corresponding elastic moduli E and Poisson's ratios ν via

$$G = \frac{E}{2(1+\nu)} \tag{16}$$

and the Burger's vectors at T_{max} were obtained from Shang et al.[95] Assuming random precipitate distribution as well as constant particle sizes and phase fractions during steady-state phase, the effective threshold stresses were found to be most successfully determined via a modified Ashby-Orowan formulation[67] according to

$$\sigma_{th} = 0.06\, M\, \tau_0\, ln\sqrt{\frac{8}{3}\frac{d}{b}} \tag{17}$$

where M is the Taylor factor, i.e. the average value of Schmid factors in a polycrystalline material. It is used to convert shear stresses in the slip systems of each grain into normal stress. For all three alloys, it was assumed to be 3.06 which is a common value for fcc polycrystals assuming random grain orientation. **Table 33** summarizes the parameters used to determine the threshold stresses and the resulting stress values.

Due to the small particle size and high phase fraction of γ' phase in Haynes 282, the alloy obtains the highest threshold stress.

Table 33. Parameters for threshold stress determination and resulting stresses for each investigated alloy

	$E_{T_{max}}$	$\nu_{T_{max}}$	$G_{T_{max}}$	$b_{T_{max}}$	d	f	λ	σ_{th}
	GPa	-	GPa	nm	nm	%	nm	MPa
Inconel 718	143	0.327	54	0.276	70	14	134	100
Allvac 718Plus	167	0.340	62	0.283	80	16	144	110
Haynes 282	160	0.356	59	0.257	35	18	59	200

Figure 100 shows the stress dependence of the alloys' minimum strain rates corrected via the determined Ashby-Orowan threshold stresses. Again, high R^2 values indicate good linear approximation. Corresponding to their performance during the forging simulations, the stress sensitivity of the alloys decreases from Inconel 718 (n = 7.4) to Allvac 718Plus (n = 4.6) and Haynes 282 (n = 3.5).

While the stress exponents of Allvac 718Plus and Haynes 282 show good agreement with typical values obtained for dislocation creep (n = 5 and n = 3, respectively), the value of Inconel 718 is still too high despite the correction. This could be explained by the fact that γ' phase was not clearly observed experimentally and therefore neglected in the threshold stress determination.

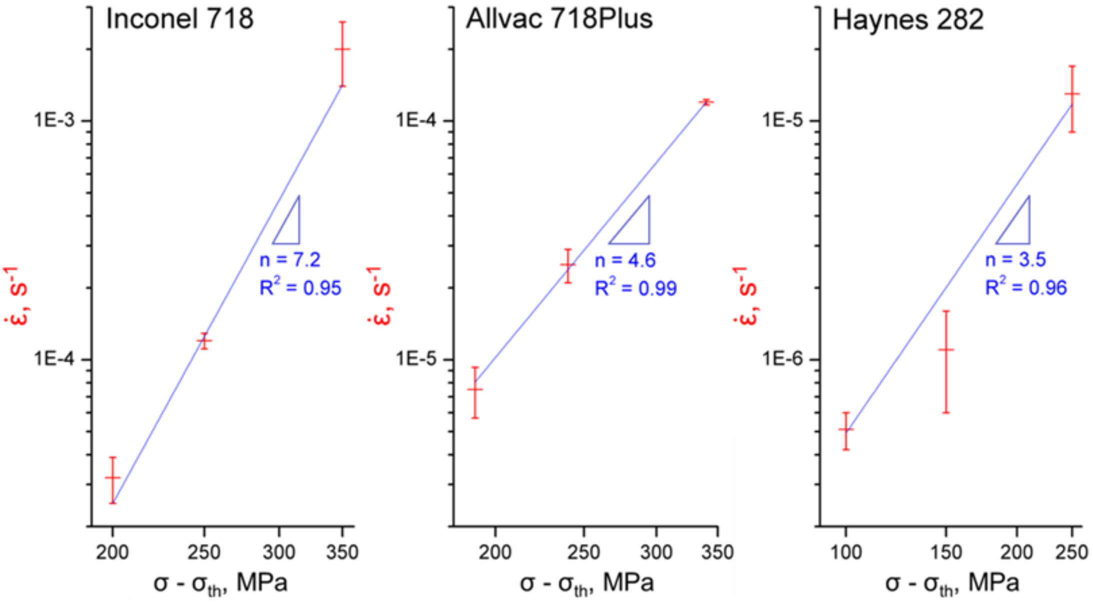

Figure 100. Stress dependence of minimum strain rates corrected via threshold stresses

To improve the results, further experimental work (such as thermomechanical tests at different maximum stress levels or at constant stress and temperature) would be needed. FEG-SEM or TEM investigations on specimens after deformation to different plastic strain could help to gain better insight into the precipitation kinetics during forging. Then, a further enhanced approach to determine the stress exponents could be established by incorporating time-dependent precipitate parameters, i.e. $d(t)$ and $f(t)$. Thus, the importance of changing precipitate microstructure on material softening during the loading conditions could be assessed more accurately.

However, as the performance of all three alloys was grain size independent, dislocation creep is the proposed dominant deformation mechanism at low strains (i.e. the technically relevant field of application).

6.3 Error influences on results

Although the results of the physical forging simulations are generally in good agreement for each set of parameters, some discrepancies occurred. This could be explained either by experimental errors or with regards to the material influences, i.e. microstructural reasons. The suggested error influences include:

- loosening of the locking nuts during long tests due to vibrations and plastic deformation
- unsymmetrical positioning of the thermocouple
- thermocouple measurement errors during long-term tests due to diffusion effects[96]
- wrong position or angle of CGauge sensor
- slip of CGauge sensor due to bulging of the specimens during testing
- tolerances (i.e. variations in specimen diameter and length
- variations in specimen surface condition and burr
- variations in grain size
- variations of precipitate parameters (size, morphology, distribution, quantity)

The results of the stress exponent determination could be falsified to certain extent due to the general assumptions concerning constant stress, temperature and microstructure during deformation up to low plastic strains and some possible systematical and/or statistical errors:

- inaccurate determination of minimum strain rates from strain curves (strain rate curves mathematically derived from strain curves were not properly evaluable)
- inaccurate experimental determination of precipitate type, size and quantity
    - too small amount of investigated micrographs
    - too low magnification of investigated micrographs
    - no certain identification of the phases (only assumptions based on literature review and numerical simulations)
    - inaccurate determination of size and quantity of strengthening precipitates inside grains (the grain structure was neglected in the determination of phase fractions)

6.4 Softening

Each alloy obtained progressive increase in strain after preceding approximately linear behavior at lower strain rate. Even though certain changes in the precipitate microstructure occurred during this stage of deformation (see chapter 5.4), the main softening mechanism responsible for the drop in strength is believed to be the formation of new, very small grains via DRX. After these new grains form (mostly at grain boundaries), they do not yet contain strengthening phases (as the precipitation process requires a certain annealing time) for which reason they are relatively soft in comparison to the initial precipitation-hardened grains. However, the performance comparison of the three materials suggests that DRX happened after significantly different times (i.e. a different number of forging cycles) in each alloy.

Inconel 718 shows the lowest performance which is most likely attributable to the presence of only few grain boundary precipitates (δ phase) after heat treatment. These precipitates coarsened rapidly during thermomechanical testing which facilitated the occurrence of DRX as there were fewer obstacles to formation and growth of new grains. Contrary to initial assumptions, however, no considerable transformation of γ'' to δ phase inside grains and only slight coarsening of γ'' phase was observable which contributes to the assumption that DRX was the main softening mechanism in this alloy.

In comparison to Inconel 718, Allvac 718Plus contained more grain boundary δ phase with slower coarsening rates which is suggested to be one of the reasons for its better performance. Another reason could be the stronger effect of solid solution strengthening counteracting plastic deformation and DRX as it obtains higher content of Co, W and Al compared to Inconel 718. However, γ' phase was found to be less stable as γ'' phase in Inconel 718 as large-scale transformation to δ phase was observed, certainly affecting the alloy’s performance.

The outstanding performance of Haynes 282 in comparison with the other two alloys is believed to result mainly from its grain boundary precipitates. Apparently, these carbides are very stable and exhibited favorable morphology and size to retard DRX. Furthermore, the alloy contained higher amounts of γ' phase. The stability of this phase during the comparably long service time as well as strong solid solution strengthening (high content of Co and Mo) are assumed to be further reasons for the good microstructure stability of Haynes 282.

It was not possible to identify a significant connection between grain size and material performance during physical forging simulations. However, the larger grain size of Haynes 282 compared to the other alloys could also be a reason for its beneficial thermomechanical behavior, especially at higher plastic strains. This assumption is based on the fact that smaller grain size offers more locations for the formation of DRX and generally facilitates diffusion processes leading to particle coarsening or transformation.

6.5 Damage

Several (mostly intercrystalline) surface cracks were observed in all three alloys in the bulged regions of strongly deformed specimens. Furthermore, the investigated deformed microstructures exhibit a low number of grain boundary pores, especially near the specimen borders. These pores are suggested to be the result of creep damage.

Despite their occurrence, none of the specimens fractured even at very high plastic strains. This could be explained by the mostly compressive nature of the load spectrum with only short stages of tensile load. Formation of pores and subsequent fracture due to pore coalescence is typical for tensile conditions during creep (or fatigue) loading while compressive stresses tend to counteract crack formation.

Few pores were also observed near large primary carbides in all alloys. However, such pores were found in the deformed material as well as the undeformed base material for which reason they are not classified as damage as they could result from metallographic specimen preparation.

7 Conclusion

Softening of all three alloys during physical forging simulations was found to result mainly from a combination of precipitate coarsening and dynamic recrystallization at grain boundaries.

Haynes 282 clearly showed the best results during the thermomechanical tests. This can be explained by its alloy system which enables strong solid solution strengthening and precipitation of different strengthening phases.

In comparison to Inconel 718 and Allvac 718Plus, Haynes 282 exhibits a higher phase fraction of nanometer-sized γ' precipitates inside grains. Furthermore, the phase shows higher thermal stability and slower coarsening rates as equivalent strengthening phases (γ'/γ'') in the other alloys.

Haynes 282 contains different types of carbides evenly distributed along grain boundaries. These phases obtain significantly higher thermal stability in comparison to grain boundary δ phase present in Inconel 718 and Allvac 718Plus.

The current market prices of the investigated alloys differ quite strongly (roughly 25 €/kg for Inconel 718, 35 €/kg for Allvac 718Plus and 42 €/kg for Haynes 282). However, considering the cost of forging die manufacture, a clear recommendation of Haynes 282 for the use as forging die material can be made both from technical and economic point of view.

8 List of figures

9 List of tables

10 Bibliography

[1] Böhler Schmiedetechnik GmbH & Co KG, http://www.bohler-forging.com/english/876.php (lastly accessed on May 15, 2013).

[2] Clean Sky Joint Undertaking, http://www.cleansky.eu/content/homepage/about-us (lastly accessed on May 15, 2013).

[3] S. Kremmer, H. F. Chladil, H. Clemens, A. Otto, V. Güther, “Near Conventional Forging of Titanium Aluminides”, Proceeding of the 11th World Conference on Titanium, The Japan Institute of Metals (2007) 989-992.

[4] M. Lang, “Werkstoffwahl für ein Gesenk zur Turbinenschaufelherstellung”, Bachelor Thesis, Graz University of Technology (2012).

[5] DIN 8583-4, “Fertigungsverfahren Druckumformen, Teil 4: Gesenkformen - Einordnung, Unterteilung, Begriffe”, Deutsches Institut für Normung (2003).

[6] E. Doege, B.-A. Behrens, “Handbuch Umformtechnik - Grundlagen, Technologien, Maschinen”, Springer (2007).

[7] S. L. Semiatin, “ASM Handbook Volume 14A - Metalworking: Bulk Forming”, ASM International (2005).

[8] F. Klocke, W. König, “Fertigungsverfahren 4 - Umformen”, Springer (2006).

[9] H. Haller, “Handbuch des Schmiedens”, Hanser Verlag (1971).

[10] K. Lange, “Umformtechnik - Handbuch für Industrie und Wissenschaft, Band 2: Massivumformung”, Springer (1990).

[11] G. Spur, T. Söferle, “Handbuch der Fertigungstechnik, Band 2: Umformen und Zerteilen”, Carl Hanser Verlag (1984).

[12] H. Luig, T. Bobke, “Beanspruchung und Schadensarten an Schmiedegesenken”, Tribologie und Schmierungstechnik, Vol. 37, No. 2 (1990) 76-81.

[13] R. Bürgel, “Handbuch Hochtemperatur-Werkstofftechnik”, Vieweg+Teubner Verlag (2011).

[14] M. Durand-Charre, “The Microstructure of Superalloys”, Gordon and Breach Science Publishers (1997).

[15] R. F. Decker, “The evolution of wrought age-hardenable superalloys”, JOM, Vol. 58, No. 9 (2006) 32-36.

[16] J. R. Davis, “ASM Specialty Handbook: Nickel, Cobalt, and Their Alloys”, ASM International (2000).

[17] M. J. Donachie, S. J. Donachie, “Superalloys: A Technical Guide”, ASM International (2002).

[18] C. T. Sims, N. S. Stoloff, W. C. Hagel, “Superalloys II: High-Temperature Materials for Aerospace and Industrial Power”, Wiley (1987).

[19] J. N. DuPont, J. C. Lippold, S. D. Kiser, “Welding Metallurgy and Weldability of Nickel-Base Alloys”, John Wiley & Sons (2009).

[20] A. K. Jena, M. C. Chaturvedi, “The role of alloying elements in the design of nickel-base superalloys”, Journal of Materials Science, Vol. 19, No. 10 (1984) 3121-3139.

[21] X. Xie, X. Liu, Y. Hu, B. Tang, Z. Xu, J. Dong, K. Ni, “The role of phosphorus and sulfur in Inconel 718”, Superalloys 2004, TMS (1996) 599-606.

[22] M. Stockinger, “Mikrostrukturelle Simulation des Gesenkschmiedens von Nickelbasis-Legierungen”, PhD Thesis, Graz University of Technology (2003).

[23] E. Nembach, G. Neite, “Precipitation hardening of superalloys by ordered γ' particles”, Progress in Materials Science, Vol. 29 (1985) 177-319.

[24] N. Seliga, “Untersuchungen der Strukturstabilität von Ni-(Fe)-Basislegierungen für Rotorwellen in Dampfturbinen mit Arbeitstemperaturen über 700 °C”, PhD Thesis, RWTH Aachen (2005).

[25] C. Stotter, C. Sommitsch, J. Wagner, H. Leitner, I. Letofsky-Papst, G. A. Zickler, W. Prantl, M. Stockinger, “Characterization of δ-phase in superalloy Allvac 718Plus™”, International Journal of Materials Research, Vol. 99, No. 4 (2008) 376-380.

[26] R. L. Kennedy, “Allvac® 718Plus™, Superalloy for the Next Forty Years”, Superalloys 718, 625, 706, and Various Derivatives, TMS (2005) 1-14.

[27] X. Xie, G. Wang, J. Dong, C. Xu, W.-D. Cao, R. Kennedy, “Structure stability study on a newly developed Nickel-base superalloy - Allvac® 718Plus™”, Superalloys 718, 625, 706, and Various Derivatives, TMS (2005) 179-191.

[28] X. Xie, C. Xu, G. Wang, J. Dong, W.-D. Cao, R. L. Kennedy, "TTT diagram of a newly developed Nickel-base superalloy - Allvac® 718Plus™", Superalloys 718, 625, 706, and Various Derivatives, TMS (2005) 193-198.

[29] R. B. Li, M. Yao, W. C. Liu, X. C. He, "Isolation and determination for δ, γ' and γ'' phases in Inconel 718 alloy", Scripta Materialia, Vol. 46, Issue 9 (2002) 635-638.

[30] A. Oradei-Basile, J. F. Radavich, "A Current TTT Diagram for Wrought Alloy 718", Superalloys 718, 625 and Various Derivatives (1991) 325-334.

[31] A. Thomas, M. El-Wahabi, J. M. Cabrera, J. M. Prado, "High temperature deformation of Inconel 718", Journal of Materials Processing Technology, Vol. 177 (2006) 469-472.

[32] Special Metals, INCONEL® Alloy 718 datasheet, http://www.specialmetals.com/documents/Inconel%20alloy%20718.pdf (lastly accessed on May 15, 2013).

[33] R. B. Bhavsar, A. Collins, S. Silverman, "Use of Alloy 718 and 725 in Oil and Gas Industry", Superalloys 718, 625, 706, and Various Derivatives, TMS (2001) 47-55.

[34] R. A. Jeniski Jr., R. L. Kennedy, "Development of ATI Allvac® 718Plus™ Alloy and Applications", Second Symposium on Recent Advantages of Nb-Containing Materials in Europe (2006).

[35] G. A. Zickler, R. Radis, R. Schnitzer, E. Kozeschnik, M. Stockinger, H. Leitner, "The precipitation Behavior of Superalloy ATI Allvac® 718Plus™", Advanced Engineering Materials, Vol. 12, Issue 3 (2010) 176-183.

[36] W.-D. Cao, "Solidification and solid state phase transformation of Allvac® 718 Plus™ alloy", Superalloys 718, 625, 706, and Various Derivatives, TMS (2005) 165-177.

[37] G. A. Zickler, R. Schnitzer, R. Radis, R. Hochfellner, R. Schweins, M. Stockinger, H. Leitner, "Microstructure and mechanical properties of the superalloy ATI Allvac® 718Plus™", Materials Science and Engineering A, Vol. 523 (2009) 295-303.

[38] ATI Allvac, ATI 718Plus® Alloy datasheet, http://www.atimetals.com/Documents/ati_718plus_tds_en-v3.pdf (lastly accessed on May 15, 2013).

[39] L. M. Pike, "Development of a fabricable gamma-prime (γ') strengthened superalloy", Superalloys 2008, TMS (2008) 191-200.

[40] C. J. Boehlert, S. C. Longanbach, "A comparison of the microstructure and creep behavior of cold rolled HAYNES® 230 alloy™ and HAYNES® 282 alloy™", Materials Science and Engineering A, Vol. 525 (2011) 4888-4898.

[41] F. Duschel, "Thermo-Mechanische Analyse der Nickelbasis Superlegierung Haynes 282", Master Thesis, Vienna University of Technology (2013).

[42] R. A. Buckson, O. A. Ojo, "Cyclic deformation characteriztics and fatigue crack growth behaviour of a newly developed aerospace superalloy Haynes 282", Materials Science and Engineering A, Vol. 555 (2012) 63-70.

[43] Haynes International, HAYNES® 282® Alloy datasheet, http://www.haynesintl.com/pdf/h3173.pdf (lastly accessed on May 15, 2013).

[44] Y. Wen, "Computational Modeling of Microstructural Evolution in Alloys for Advanced Fossil Power Systems", 26th Annual Conference on Fossil Energy Materials (2012), http://www.netl.doe.gov/publications/proceedings/12/fossil_energy_materials/pdf/Tue/Wen.FE2012_2.pdf (lastly accessed on May 15, 2013).

[45] G. Winther, "Slip systems, dislocation boundaries and lattice rotations in deformed metals", PhD Thesis, Technical University of Denmark (2009).

[46] B. K. Sokolov, V. V. Gubernatorov, I. V. Gervasyeva, A. K. Sbitney, L. R. Vladimirov, "The deformation and shear bands in the Fe-3%Si alloy", Textures and Microstructures, Vol. 32 (1999) 21-39.

[47] J. Rösler, H. Harders, M. Bäker, "Mechanisches Verhalten der Werkstoffe, 2. Auflage", Teubner (2006).

[48] M. E. Kassner, M.-T. Pérez-Prado, "Five-power-law creep in single phase metals and alloys", Progress in Materials Science, Vol. 45 (2000) 1-102.

[49] M. A. Meyers, K. K. Chawla, "Mechanical Behavior of Materials, Second Edition", Cambridge University Press (2009).

[50] B. Wilshire, C. J. Palmer, "Grain size effects during creep of copper", Scripta Materialia 46 (2002) 483-488.

[51] H. Yafang, M. C. Chaturvedi, "Steady-state Creep Equation of Inconel 718 Superalloy", Journal of Materials Science and Technology, Vol. 5, No. 2 (1989) 79-84.

[52] F. Abe, T.-U. Kern, R. Viswanathan, “Creep-resistant steels”, Woodhead Publishing (2008).

[53] M. F. Ashby, D. Jones, “Engineering Materials 1: An Introduction to their properties & applications, Second Edition”, Butterworth Heinemann (1996).

[54] H. J. Frost, M. F. Ashby, “Deformation-Mechanism Maps: The Plasticity and Creep of Metals and Ceramics”, Pergamon Press (1982).

[55] O. D. Sherby, E. M. Taleff, “Influence of grain size, solute atoms and second-phase particles on creep behaviour of polycrystalline solids”, Materials Science and Engineering A, Vol. 322 (2002) 89-99.

[56] G. Bernasconi, G. Piatti, “Creep of Engineering Materials and Structures”, Applied Science Publishers (1978).

[57] Y. Han, M. C. Chaturvedi, “A study of back stress during creep deformation of a superalloy Inconel 718”, Materials Science and Engineering, Vol. 85 (1987) 59-65.

[58] M. McLean, “On the threshold stress for dislocation creep in particle strengthened alloys”, Acta Metallica, Vol. 33, No. 4 (1985) 545-556.

[59] R. A. Stevens, P. E. J. Flewitt, “The dependence of creep rate on microstructure in a γ' strengthened superalloy”, Acta Metallurgica, Vol. 29 (1981) 867-882.

[60] E. Arzt, D. S. Wilkinson, “ Thresholds stresses for dislocation climb over hard particles - the effect of an attractive interaction”, Acta Metallica, Vol. 34, No. 10 (1986) 1893-1898.

[61] J. Rösler, E. Arzt, “A new model-based creep equation for dispersion strengthened materials”, Acta Metallurgica et Materialia, Vol. 38, No. 4 (1990) 671-683.

[62] M. F. Ashby, H. Shercliff, D. Cebon, “Materials engineering, science, processing and design, Second Edition”, Elsevier (2010).

[63] F. J. Humphreys, M. Hatherly, “Recrystallization and Related Annealing Phenomena, Second Edition”, Pergamon Materials Series (2004).

[64] M. Ueki, S. Horie, T. Nakamura, “Factors affecting dynamic recrystallization of metals and alloys”, Materials Science and Technology, Vol. 3, No. 5 (1987) 329-337.

[65] R. L. Goetz, “Particle stimulated nucleation during dynamic recrystallization using a cellular automata model”, Scripta Materialia, Vol. 52 (2005) 851–856.

[66] National Physical Laboratory, MTDATA - Phase Diagram Software, Calculated phase diagrams, http://resource.npl.co.uk/mtdata/phdiagrams/nbni.htm/http://resource.npl.co.uk/mtdata/phdiagrams/alni.htm/ http://resource.npl.co.uk/mtdata/phdiagrams/niti.htm (lastly accessed on May 15, 2013).

[67] I. Holzer, “Modelling and Simulation of Strengthening in Complex Martensitic 9-12% Cr Steel and a Binary Fe-Cu Alloy”, PhD Thesis, Graz University of Technology (2010).

[68] Institute for Materials Science and Technology, Vienna University of Technology, http://www.matcalc.at (lastly accessed on May 15, 2013).

[69] J. Svoboda, F. D. Fischer, P. Fratzl, E. Kozeschnik, “Modelling of kinetics in multi-component multi-phase systems with spherical precipitates I - Theory”, Materials Science and Engineering A, Vol. 365, No. 1-2 (2004) 166-174.

[70] E. Kozeschnik, J. Svoboda, P. Fratzl, F. D. Fischer, „Modelling of kinetics in multi-component multi-phase systems with spherical precipitates II - Numerical solution and application“, Materials Science and Engineering A, Vol. 365, No. 1-2 (2004) 157-165.

[71] E. Kozeschnik, J. Svoboda, F. D. Fischer, “Modified evolution equations for the precipitation kinetics of complex phases in multi-component systems”, CALPHAD, Vol. 28, No. 4 (2005) 379-382.

[72] J. Svoboda, I. Turek, F. D. Fischer, “Application of the thermodynamic extremal principle to modeling of thermodynamic processes in material sciences”, Philosophical Magazine, Vol. 85, No. 31 (2005) 3699-3707.

[73] K. Janssens, D. Raabe, E. Kozeschnik, M. Miodownik, B. Nestler, “Computational Materials Engineering - An Introduction to Microstructure Evolution”, Elsevier Academic Press (2007).

[74] B. Sonderegger, E. Kozeschnik, “Generalized nearest neighbor - broken bond analysis of randomly oriented coherent interfaces in multi-component fcc and bcc structures”, Metallurgical and Materials Transactions A, Vol. 40 (2009) 499-510.

[75] R. Radis, G. A. Zickler, M. Stockinger, C. Sommitsch, E. Kozeschnik, “Interaction of the Precipitation Kinetics of δ and γ' Phases in Nickel-Base Superalloy ATI Allvac® 718Plus™”, Materials Science Forum, Vol. 638-642 (2010) 2712-2717.

[76] C. Sommitsch, E. Kozeschnik, G. Wasle, B. Buchmayr, “A Precipitation Model for Multi-Phase Systems in Nickel-Base Superalloys”, Proceedings on International Conference on Processing and Manufacturing of Advanced Materials: CDROM, Section D7, Vol. 117/3 (2001).

[77] R. Radis, M. Schaffer, M. Albu, G. Kothleitner, P. Pölt, Kozeschnik E., “Multimodal size distributions of γ' precipitates during continuous cooling of UDIMET 720 Li”, Acta Materialia, Vol. 57 (2009) 5739-5747.

[78] L. Whitmore, H. Leitner, E. Povoden-Karadeniz, R. Radis, M. Stockinger, “Transmission electron microscopy of single and double aged 718Plus superalloy”, Materials Science and Engineering A, Vol. 534 (2012) 413-423.

[79] K. Rockenschaub, W. Marketz, “Verfahren zur Warmformgebung eines Werkstückes und Mittel zur Verminderung der Wärmeabstrahlung”, European patent EP 10450089.7 (2010).

[80] H. Clemes, W. Wallgram, M. Schloffer, “Method for producing a component from a gamma-titanium-aluminium base alloy”, European patent EP 11450055.6 (2011).

[81] S. Kremmer, H. Romen-Kierner, W. Wallgram, “Method for producing a forged article from a gamma-titanium-aluminium base alloy”, European patent EP 10450090.5 (2010).

[82] Dynamic Systems Inc., Gleeble® 3800 System, http://gleeble.com/index.php/products/gleeble-3800.html (lastly accessed on May 15, 2013).

[83] R. Klemm, “Thermoelemente in der industriellen Praxis”, Rössel Messtechnik GmbH, http://www.roessel-messtechnik.de/webro-wAssets/docs/Seminare/Thermoelemente_in_der_industriellen_Praxis.pdf (lastly accessed on May 15, 2013).

[84] C. Moosbrugger, “Atlas of Stress-Strain Curves, Second Edition”, ASM International (2002).

[85] ASTM E112 - 96, “Standard Test Methods for Determining Average Grain Size”, ASTM International (2004).

[86] M. Funk, “Grain and particle analysis with line intersection method”, Karlsruhe Institute of Technology, http://www.mathworks.com/matlabcentral/fileexchange/35203-grain-and-particle-analysis-with-line-intersection-method (lastly accessed on May 15, 2013).

[87] E. Kozeschnik, W. Rindler, B. Buchmayr, “Scheil-Gulliver simulation with partial redistribution of fast diffusers and simultaneous solid-solid phase transformations”, International Journal of Materials Research, Vol. 98 (2007) 826-831.

[88] W. Rindler, E. Kozeschnik, B. Buchmayr, “Computer simulation of the brittle temperature range (BTR) for hot cracking in steels”, Steel Research, Vol. 71, No. 11 (460-465).

[89] P. Sherstnev, P. Lang, E. Kozeschnik, “Treatment of simultaneous deformation and solidstate precipitation in thermo-kinetic calculations”, European Congress on Computational Methods in Applied Sciences and Engineering (2012).

[90] M. Santella, J. Shingledecker, B. Swindeman, “Materials for Advanced Ultra-Supercritical Steam Boilers”, 24th Annual Conference on Fossil Energy Materials, Pittsburgh, USA (2010).

[91] L. Liu, C. Lu, W. Ding, A. Hirose, K. F. Kobayashi, “Effect of Phase on Hydrogen Embrittlement of Inconel 718 by Notch Tensile Tests”, Journal of Materials Science and Technology, Vol. 21, No. 2 (2005), 256-260.

[92] M. Dumont, W. Lefebvre, B. Doisneau-Cottignies, A. Deschamps, “Characterization of the composition and volume fraction of η' and η precipitates in an Al-Zn-Mg alloy by a combination of atom probe, small-angle X-ray scattering and transmission electron microscopy”, Acta Materialia, Vol. 53 (2005) 2881-2892.

[93] A. Devaux, L. Nazé, R. Molins, A. Pineau, A. Organista, J.Y. Guédou, J. F. Uginet, P. Héritier, “Gamma double prime precipitation kinetic in Alloy 718”, Materials Science and Engineering A, Vol. 486 (2008) 117-122.

[94] G. F. Vander Voort, “ASM Handbook Volume 9 - Metallography and Microstructures”, ASM International (2004).

[95] S. L. Shang, “Volume, Burgers Vector and Stacking Fault Energy of Ni-base superalloys”, Phases Research Lab at Penn State University, http://www.phases.psu.edu/Tools/VBSFEscripts/VBSFE.html (lastly accessed on May 15, 2013).

[96] Dynamic Systems Inc., Gleeble® System Application Note, “Diffusion Effects on Type K (Cr-Al) Thermocouple Measurements” (2001).